Inhibition and dynamics of a β-lactamase
Elings, W.

Citation
Elings, W. (2019, November 19). *Inhibition and dynamics of a β-lactamase*. Retrieved from https://hdl.handle.net/1887/80412

Cover Page

Universiteit Leiden

Leiden University
Repository

The following handle holds various files of this Leiden University dissertation:
http://hdl.handle.net/1887/80412

Author: Elings, W.
Title: Dynamics of a β-lactamase
Issue Date: 2019-11-19

Inhibition and dynamics of a β-lactamase

Proefschrift

ter verkrijging van
de graad van Doctor aan de Universiteit Leiden,
op gezag van Rector Magnificus prof.mr. C.J.J.M. Stolker,
volgens besluit van het College voor Promoties
te verdedigen op dinsdag 19 november 2019
klokke 11:15 uur

door
Wouter Elings
geboren te Utrecht, Nederland
in 1989

Promotor: Prof. dr. M. Ubbink

Tweede promotor: Prof. dr. G.P. van Wezel

Promotiecommissie: Prof. dr. H.S. Overkleeft (voorzitter)

                        Prof. dr. A.H. Meijer (secretaris)

                        Dr. P.-L. Hagedoorn

                        Prof. dr. D.F. Hansen

Contents

Abbreviations

AIC	Akaike Information Criterion
ATP	Adenosine triphosphate
Bis-Tris	Bis(2-hydroxyethyl)amino-tris(hydroxymethyl)methane
BMRB	Biological Magnetic Resonance Data Bank
CEST	Chemical Exchange Saturation Transfer
CFU	Colony Forming Unit
CPMG	Carr-Purcell-Meiboom-Gill sequence
CSP	Chemical Shift Perturbation
dATP	Deoxyadenosine triphosphate
dCTP	Deoxycytidine triphosphate
dGTP	Deoxyguanosine triphosphate
DNA	Deoxyribonucleic acid
DTT	Dithiothreitol
dTTP	Deoxythymidine triphosphate
EDTA	Ethylenediaminetetraacetic acid
ESBL	Extended Spectrum β-Lactamase
HSQC	Heteronuclear Single Quantum Coherence
IPTG	Isopropyl β-D-1-thiogalactopyranoside
LB	Lysogeny Broth
MD	Molecular Dynamics
MES	2-Ethanesulfonic acid
MIC	Minimal Inhibitory Concentration
MS	Mass Spectrometry
Mtb	*Mycobacterium tuberculosis*
NMR	Nuclear Magnetic Resonance
NOE	Nuclear Overhauser Effect
OD	Optical Density
PCR	Polymerase Chain Reaction
PDB	Protein Data Bank
Pi	Inorganic phosphate
SDS-PAGE	Sodium Dodecyl Sulfate Polyacrylamide Gel Electrophoresis
Tat	Twin-arginine translocation
TEV	Tobacco Etch Virus protease
Tris	Tris(hydroxymethyl)aminomethane
TROSY	Transverse Relaxation Optimised Spectroscopy
UPLC	Ultra-Performance Liquid Chromatography
UV-Vis	Ultraviolet to visible
WHO	World Health Organisation
Wt	Wild type
XFEL	X-Ray Free-Electron Laser

Chapter 1

Introduction

Background

Tuberculosis

The disease that we know as tuberculosis has been killing humans since ancient times. Nevertheless, infections are believed to have been merely incidental until the increasing population density in relatively recent times allowed the disease to gain epidemic proportions. At its height in Europe in the 16th through 19th centuries, the so-called "Captain among the Men of Death" was responsible for up to a quarter of all deaths. Improvements in public healthcare and understanding of the disease led to a decline in the death toll during the 19th and early 20th century, but it was only by the discovery of streptomycin in 1946 and other highly effective antibiotics soon after that tuberculosis became a curable and controllable disease. In fact, the introduction of antibiotics was so effective that by the 1970's, it was widely believed that the disease had been defeated and would soon be eradicated completely.[1–3] Such hopes were not long-lived. In the 1980's, the appearance of drug resistance heralded a resurgence of tuberculosis that is becoming increasingly difficult to control. Today, the disease kills almost 2 million people per year, making it again the most lethal of all infectious diseases.[4–6]

Tuberculosis is caused by *Mycobacterium tuberculosis*, a bacterium that is notoriously hard to kill. Its thick, slimy cell wall slows diffusion of antibiotics into the cell. Coupled with its relatively slow generation time of about 1 day, this means that to stop an active infection, the concentration of medicine needs to remain high for a relatively long period of time. Moreover, the bacterium has the ability to encapsulate itself inside a host macrophage and subsequently stay inactive but alive for years. Such a macrophage will attract other host immune cells and form a little clump called a granuloma, which hinders the diffusion of antibiotics even more. To completely cure a tuberculosis infection, therefore, an extensive drug program must be followed, which continues for months after the symptoms have subsided. The completion rate of this treatment is poor. Especially in regions where education and finances are limited, not all patients are inclined to continue taking expensive medication after their symptoms are over. Bacteria that survive an incomplete antibiotic treatment are far more likely to be resistant against these antibiotics and so, when these are allowed to multiply again, the problem of drug resistance

1

increases dramatically. The World Health Organisation published an official definition of multidrug-resistant tuberculosis in the early 1990's. Tuberculosis was declared a global health emergency in 1993 and global initiatives were started to combat the disease. Nevertheless, by 2006 the problem had grown to the point that another classification had to be recognised: extensively drug-resistant tuberculosis.[7,8] The final step towards totally drug-resistant tuberculosis, although surprisingly difficult to define officially,[9] was reached soon after.[10,11]

The rise of drug resistance in *M. tuberculosis* poses a serious threat to public healthcare. New medicines to combat the disease are urgently needed. There are currently several new tuberculosis medicines in development,[12,13] but their numbers are limited and it may take many years before they reach the clinic. Another option that is worth looking into is the repurposing of antibiotics that are used to treat other diseases. By far the largest group of antibiotics that we know is that of the β-lactams. Their effectiveness in treating a wide range of bacterial infections as well as their safety for use in humans, have been proven beyond a doubt. Production processes have been scaled up to the extent that over half of the antibiotics that are being used are β-lactams. However, none of these compounds have been used historically to treat tuberculosis. This is because *M. tuberculosis* produces an enzyme that provides it with resistance to virtually all β-lactam antibiotics.[14–17] This enzyme is called BlaC.

BlaC

BlaC is the β-lactamase that is encoded by the *blaC* gene on the chromosome of *M. tuberculosis*. It is an extended spectrum β-lactamase (ESBL), which means that it can hydrolyse β-lactams, not only those of the penicillin group, but also those of the other two main groups: cephalosporins and carbapenems.[18] Like in all serine β-lactamases, its active site serine (Ser70) performs a nucleophilic attack on the carboxyl in the β-lactam ring, to form a covalently bound intermediate that is subsequently hydrolysed through a new nucleophilic attack by a water molecule, sitting in a conserved location in the active site. Some substrate structures and the general reaction mechanism are displayed in Figure 1.1 and Figure 1.2, respectively.
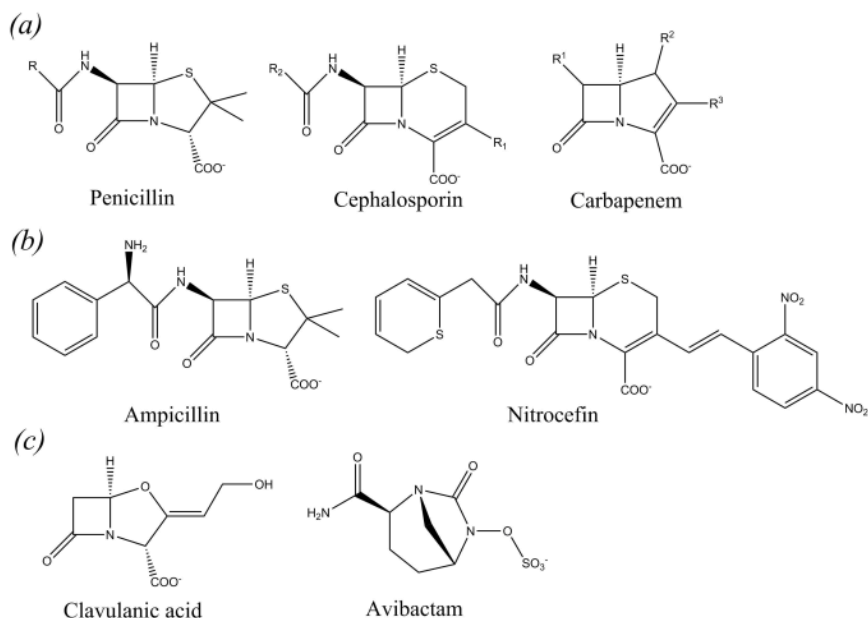
Figure 1.1: *(a)* **Core structures of the three main groups of β-lactams.** The four-membered ring, containing a nitrogen and a carbonyl, is the β-lactam ring. Note that the increasing number of rest groups in the core structures indicates an increasing level of variability within the groups. *(b)* Structures of two substrates that were used in this work. *(c)* Structures of two inhibitors that are used and/or discussed in this work.
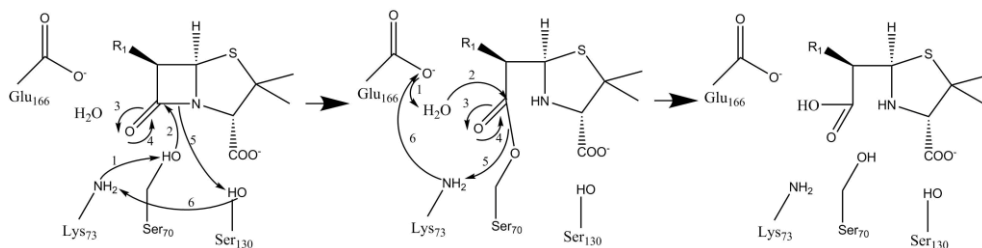

Figure 1.2: Proposed mechanism of penicillin hydrolysis by class A β-lactamases. Activated Ser70 performs a nucleophilic attack on the β-lactam carbonyl group. The β-lactam nitrogen is protonated, resulting in formation of the acyl-enzyme. Subsequent nucleophilic attack of the activated conserved active site water molecule leads to deacylation, yielding the active enzyme and the inactive β-lactam. The key steps of this enzymatic cycle are well characterised, but debate still exists over which residue activates Ser70 prior to acylation and which residues are involved in the proton shuffling (e.g. [19,20]). Shown is the proposed mechanism for BlaC.[21,22] The number labels are included to help the reader appreciate the general order of events, not as absolute and discrete steps.

The BlaC protein is exported through the *M. tuberculosis* cell membrane by the Twin-arginine translocation (Tat) pathway. The protein, with an N-terminal tat-signal peptide, is folded inside the cell and exported afterwards. The signal peptide contains a putative lipoprotein lipid attachment site. This likely tethers the protein to the cell wall after

export, as was derived from the relatively high cell-association of full-length BlaC when expressed in *Mycobacterium smegmatis* and compared to its native β-lactamase, BlaS.[23,24]

β-lactamases have been classified according to their substrate specificities[25–27] and according to their amino acid sequence similarities.[17] In the former, the Bush-Jacoby-Medeiros classification, BlaC is classified in class 2 which contains all serine penicillinases, carbapenemases and broad-spectrum β-lactamases. It has not been classified in a subgroup, however, as the broad substrate spectrum, including β-lactams from all three classes, is unique.[18] BlaC is a member of class A in the latter, the Ambler classification system. This class contains the majority of all β-lactamases that have been identified to date, but it is nevertheless slightly more specific than Bush-Jacoby class 2, as that class contains all Ambler classes A and D β-lactamases. Here, we will therefore use the Ambler classification system to indicate related β-lactamases. An additional advantage is that the Ambler system is arguably less ambiguous and more relevant in evolutionary and structural comparisons.
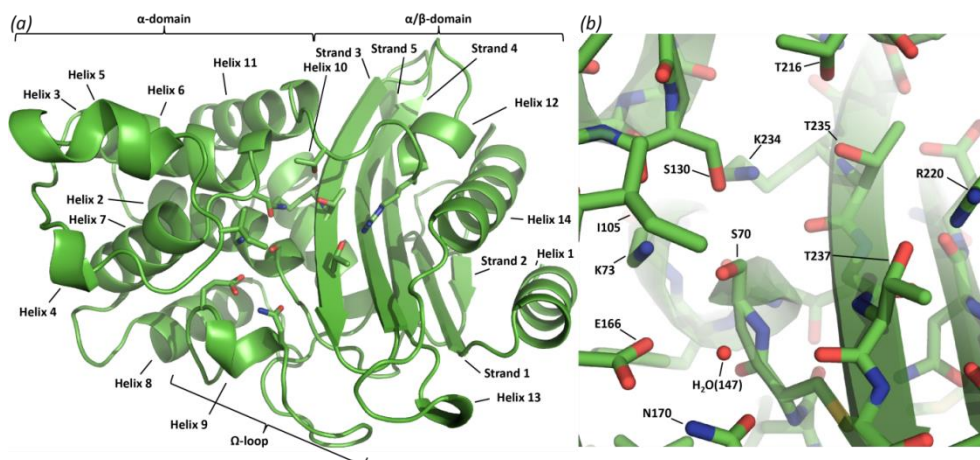

Figure 1.3: Crystal structure of BlaC (subunit A of PDB entry code 5NJ2).[28] *(a)* Cartoon representation with indication of α-helices, β-strands and the Ω-loop. Several active site residues are shown in stick representation. *(b)* Detail of the active site, showing both stick representation and transparent cartoon representation for clarity. Several active site residues and the conserved active site water molecule are indicated.

The structure of BlaC, including the major structural elements and active site residues, is displayed in Figure 1.3. The enzyme is structurally very similar to other class A β-lactamases. Nevertheless, a few structural features can be identified that are specific for BlaC. In the general class A β-lactamase models, the carboxylate group of the substrates interacts through hydrogen bonds with a pocket formed by the conserved Lys234, Thr235, Gly236 (KTG) motif and Arg244. BlaC harbours an alanine at position 244, and the spatial position of the arginine group near the active site is occupied instead by Arg220. This

arginine likely performs a very similar function to Arg244 in other class A β-lactamases. However, BlaC additionally contains a threonine at position 237, which forms an extra hydrogen bonding partner in between the arginine side chain and the substrate. Despite these structural changes in the carboxylate binding pocket compared to other class A β-lactamases, substrates have been shown to bind in the same orientation. It is therefore unclear how these substitutions affect the substrate profile and reaction kinetics.[29] On the other side of the active site, in the usually conserved substrate-binding motif serine-aspartate-asparagine (SDN) at Ambler positions 130 – 132, Asp132 is replaced by glycine. This substitution widens the active site considerably, while decreasing the potential for stabilising enzyme-substrate interactions. This likely contributes to the broad substrate profile and relatively low activity of BlaC, compared to other class A β-lactamases.[16] Another structural feature of the BlaC active site that stands out compared to its relatives is the isoleucine at position 105. This residue hangs like a lid over the active site, restricting the access. For this reason, it has been named 'gatekeeper' residue.[30] Interestingly, most class A β-lactamases harbour an aromatic residue at this position. Site-saturation mutagenesis of this residue in TEM-1 revealed that at least in that enzyme, the aromatic character of the residue plays an essential role in substrate recognition.[31] The isoleucine in BlaC is smaller, which contributes to the active site entrance being ~3 Å wider than in other class A β-lactamases.[16] This may also contribute to the broad substrate profile of BlaC. A structural peculiarity of BlaC outside the active site is that it contains a small, glycine-rich insertion in the loop between helices 7 and 8. Despite these aberrant features, it is important to emphasize that BlaC is structurally in fact very similar to other class A β-lactamases. For example, the root mean square deviation of all C_α positions in a structural alignment of BlaC (PBD 5NJ2, subunit A)[28] with TEM-1 (PDB 1BTL)[32] or SHV-1 (PDB 1SHV)[33] is only 0.9 or 0.85 Å, respectively.

The catalytic efficiency of BlaC with most penicillins (e.g. [16,18,34]) is slightly lower than that of some related β-lactamases (e.g. [35–37]). This may be related to the long generation time of *M. tuberculosis*, which could decrease the importance of sheer conversion rates. The BlaC substrate spectrum, however, is very broad. BlaC is relatively efficient at hydrolysing cephalosporins and even has considerable activity with several carbapenem antibiotics.[16,18,34] Extensive research has gone into identifying compounds that can inhibit β-lactamases.[38–40] Classical β-lactamase inhibitors clavulanic acid, tazobactam and sulbactam, as well as modern variants such as avibactam and some boronic acid-based inhibitors, have all been shown to be able to inhibit BlaC.[18,41,42] Furthermore, some carbapenems such as meropenem, tebipenem and 6-methylidene penem 2 have been found to function as substrates that take so long to degrade that they also effectively inhibit BlaC.[22,34,43,44] Due to the availability of other convenient antibiotics, combinations of these compounds have not been used historically to treat tuberculosis. Considering the rise of resistance to these other drugs, however, β-lactam / β-lactamase inhibitor

combinations have been presented in recent decades as potentially effective treatment (e.g. [29,45,54,46–53]). The most potent and popular clinically approved β-lactamase inhibitor so far is clavulanic acid.[38] In BlaC, clavulanic acid inhibition was initially reported to be irreversible[18] and later found to be slowly reversible.[41] The most used combination is that of clavulanic acid with amoxicillin. For tuberculosis, this combination was shown to be effective at least for early bactericidal activity.[55–57] An even more promising combination is that of clavulanic acid with meropenem, which was suggested to be especially suitable for treatment of difficult-to-treat cases.[47,48,50,52,53,58,59] Other potentially effective β-lactam / β-lactamase inhibitor strategies include the use of clavulanic acid and tebipenem[57] or faropenem.[60] As the use of β-lactamase inhibitors in the treatment of tuberculosis becomes more prevalent, it is high time to consider the possibility that *M. tuberculosis* may in turn develop resistance to these medicines.

Possibility of clavulanate resistance

Drug resistance at the bacterial level can arise through many pathways, amongst which are mutations in the drug target, upregulation of efflux pumps and other diffusion-limiting adjustments.[61–63] For β-lactam antibiotics, the production of β-lactamases is the most common mechanism through which bacteria reach resistance.[38,64] Specific resistance to β-lactamase inhibitors used as drugs in an antibiotics cocktail may in principle occur through as many pathways. However, as most β-lactamase inhibitors are themselves β-lactams, we will focus on mutation of the β-lactamase to resist inhibition. Mutations in β-lactamases that render them resistant to inhibition have been observed in both active site residues and residues that are far away from the active site. Overall, the effect of mutations has been observed to be highly context-dependent (e.g. [38,65–72]). In BlaC, a directed evolution strategy was employed by Feiler *et al.*, who found the I105F substitution to confer slightly decreased ampicillin-clavulanate sensitivity to *E. coli* cells due to an increased enzymatic activity. The magnitude of the inhibition itself, however, remained similar.[30] Kurz *et al.* performed site-directed mutagenesis targeted at creating a clavulanate-resistant BlaC variant, based on sequence variations conferring such resistance in homologues enzymes from other species. This approach yielded variants displaying *in vitro* clavulanate resistance due to having a significantly decreased affinity. *In vivo*, however, the slow generation time of Mtb allowed inhibition anyway.[29] This approach was continued by Egesborg *et al.*, who successfully used combinatorial mutations to increase the *in vitro* clavulanate resistance of BlaC beyond the generation time of Mtb, which is 24 hours.[73] Soroka *et al.*, on the other hand, based their approach on structural information from resistant homologues and found that the G132N substitution, which did not affect hydrolysis of other β-lactams, allowed for efficient hydrolysis of clavulanate by BlaC.[74] Though these substitutions were not tested *in vivo*, these results do suggest that β-lactam-clavulanate combinations are at risk for the development of resistance. However, the

same group later found that the increased clavulanate resistance of G132N is paired with decreased avibactam resistance.[75]

These results suggest that multiple pathways may exist through which BlaC can gain resistance to clavulanic acid. However, the extent to which resistance is reached varies considerably and there appear to be functional trade-offs. Furthermore, little is known about epistasis between these mutations, or the functionality that may be reached through the combination of multiple mutations in general. Moreover, it remains unclear to what extent these pathways, mostly found via human design, represent the most efficient routes towards resistance that are available for BlaC. Lastly, it is currently unknown if the apparent functional trade-offs can potentially be exploited through better inhibitor design.

Research questions

The ultimate goal of the research line in the Ubbink group is to design β-lactamase inhibitors for combination therapy in which BlaC resistance against inhibitors does not occur. This is an ambitious goal, for which a number of other questions need to be answered first. One requirement is to identify which evolutionary pathways by BlaC adaptation are actually available to reach inhibitor resistance. If such pathways are found, we need to understand the molecular causes of the resistance. Consequently, the first objective is to broaden and deepen our understanding of the wild type enzyme. While structures with atomic detail are available and BlaC catalytic activity has been characterized, little is known about the dynamic properties of the enzyme and also a molecular understanding of the interaction with substrates and inhibitors, in particular clavulanic acid, is lacking. Once comprehensive knowledge of the wild type enzyme has been obtained, it will be possible to generate, characterize and understand mutants that confer inhibitor resistance upon BlaC. The research questions that are addressed in this thesis are:

1. Is BlaC inhibition by clavulanic acid reversible? If so, why have there been conflicting results on this topic? (Chapter 2)
2. What is the dynamic behaviour of BlaC in solution in the resting state and in complex with clavulanic acid? (Chapter 3)
3. Is it possible for BlaC to gain resistance to clavulanic acid inhibition through one or a few amino acid mutations? If so, what are the involved mechanisms? Do they involve conformational dynamics? (Chapter 4)

Methodology

Protein dynamics

To date, 49 crystal structures have been published of BlaC, giving a high-resolution look at the structural features of the enzyme, either in free form or bound to various substrate and inhibitor adducts. However, in order to fully understand the function of an enzyme, not only the static structural features are required, but also structural changes as a function of time. Proteins do not exist in a single conformation but rather as a dynamic ensemble of conformations. The sampled conformational landscape may have any number of local energy minima, each with different populations. Exchange between the different conformations occurs on a wide range of time scales. Moreover, a large body of evidence illustrates the importance of this flexibility in various biological processes, including catalysis.[76–83]

The method of choice to measure the dynamics behaviour of proteins is nuclear magnetic resonance (NMR) spectroscopy. In NMR spectroscopy, the magnetic resonances of individual nuclei in a protein are measured. The frequency at which they resonate depends on their chemical environment. Therefore, changes in the chemical environment of individual nuclei can be detected. If the protein is dynamic, some atoms will experience several chemical environments. This phenomenon is called chemical exchange and can be probed using NMR spectroscopy.

If the exchange between states occurs on a time scale that is slower than the difference in resonance frequencies between the states, it is called slow exchange and all states with a population above the detection limit can be measured separately. If the chemical exchange process occurs on a similar time scale as the difference in resonance frequencies, it is referred to as intermediate exchange. In this case, significant line broadening will be observed, leading to a decrease in peak intensity. If the exchange process is much faster than the resonance frequency difference, it is called fast exchange and only an average state is measured. Nevertheless, also in these cases, NMR spectroscopy offers various possibilities to explore some of the characteristics of the process underlying the exchange.

Protein motions cause fluctuations in the local magnetic fields surrounding nuclei through changes in dipole-dipole orientations and due to chemical shift anisotropy. The frequency distribution of these fluctuations is called the spectral density $J(\omega)$. When the frequency of a magnetic field fluctuation matches the energy difference between nuclear spin states, it can cause spin transitions. Spin energy transitions, in turn, can be detected by NMR spectroscopy in the form of relaxation. A variety of NMR experiments has therefore been designed that probe various types of relaxation. In particular, the longitudinal (T_1) relaxation, transverse (T_2) relaxation and steady-state heteronuclear Overhauser effect

(NOE), based on the phenomenon of cross-relaxation, of each backbone amide are often measured. The magnitudes of these types of relaxation are each defined by the spectral density at a combination of frequencies.[84] The spectral density itself, in turn, can be described in terms of motion parameters.[85,86] This allows the use of motion parameters to perform a least-squares fit of the spectral density function to the measured relaxation rates. This approach is called Lipari-Szabo formalism and the theory behind it has been explained extensively in the seminal papers by Lipari and Szabo and by others,[85–90] so we will not go into much detail here. The goal is to extract meaningful parameters of the motion, which can be interpreted in structural terms. Typically, fast internal motion of the measured amide bonds can be described with just two motion parameters per amide bond, S^2 and τ_e, using a least-squared fit of the spectral density function as described in Equation 1.1[85,86,88] to the combined data. S^2 is the order parameter, which represents the spatial restriction of the internal bond motion. It has a value between 0 and 1, 1 meaning no local motion. τ_e is the effective correlation time of the individual amide bond vector, which represents the rate of internal motion. τ_c is the rotational correlation time of the molecule, a measure for the tumbling rate of the protein. Overall tumbling of the protein itself is an important contributor to the magnetic field fluctuation and thus to the relaxation. Unlike S^2 and τ_e, however, τ_c is a global parameter which is not fitted separately per measured amide bond but rather only once for the entire dataset.

Equation 1.1

$$J(\omega) = \frac{2}{5} * \tau_c * \left[\frac{S^2}{(1 + (\tau_c * \omega)^2)} + \frac{(1 - S^2) * (\tau_c + \tau_e) * \tau_e}{(\tau_c + \tau_e)^2 + (\omega * \tau_c * \tau_e)^2} \right]$$

If the tumbling and diffusion of the molecule are not isotropic, they will affect amides that are oriented in different orientations in the molecule differently. In this case, instead of a single value τ_c, a global anisotropic diffusion tensor must be fitted based on the molecular structure of the protein.[91] Furthermore, although Equation 1.1 does not assume any particular type of internal motion, it does assume that the dynamic behaviour can be described with just one frequency of internal motion. In practice, proteins may move at a large range of frequencies. A single amide bond might therefore experience multiple types of movement. In these cases, the measured NOE values tend to be sensitive to the fastest detectable movement, typically in the ps-ns range, while the observed R_2 tends to be affected by all movement. The observed R_2 then cannot be explained by Equation 1.1 alone, so for these amides, an extra contribution to the R_2 is added, R_{ex}. While τ_e and S^2 represent the fast local movement of the amide bond relative to the rest of the protein, R_{ex} then reports on a slower movement, typically indicating movement of a larger protein segment. This slow chemical exchange forms an additional individual parameter in a fitting process that already has many parameters, which often leads to over fitting. It is therefore usually difficult to interpret the R_{ex} beyond the indication that µs-ms motions may be

present. However, for many proteins, this represents the motion with the most relevant biological significance. Fortunately, the contribution of chemical exchange to the apparent transverse relaxation can also be measured directly, using the relaxation dispersion experiment.

Line broadening due to chemical exchange occurs when the exchange rate is around the same frequency as the chemical shift difference, i.e. there is intermediate exchange. In this case, it is possible to refocus the line broadening by application of 180˚ pulses with a higher frequency. The rate of the motion and chemical shift difference can therefore be estimated by measuring the transverse relaxation as a function of 180˚ pulse frequency. This can be done by applying a Carr-Purcell-Meiboom-Gill (CPMG) pulse train with a varied pulse frequency within a fixed relaxation time.[92–94] Exchange parameters are calculated by fitting the Bloch-McConnell equations[95,96], which describe the relation between exchange and peak broadening, to the relaxation data.[97] Modern NMR spectrometers can perform this experiment with pulse frequencies in the range of $10^1 - 10^3$ s^{-1}, making this experiment ideally suited to analyse exchange processes in that frequency range. To access faster motions, a continuous spin-lock field can be used instead of a 180˚ pulse train. In this case, the power of the lock field is varied rather than the pulse frequency. This type of experiment is called $T_{1\rho}$ and is used to investigate motions in the $10^3 - 10^6$ s^{-1} frequency range.[98,99]

Another experiment that can be applied to elucidate slow protein dynamics is Chemical Exchange Saturation Transfer (CEST).[100] As mentioned before, nuclei will likely experience different chemical environments in different protein conformations. In practice, there is often one ground state with a high population and one or more excited states that are too sparsely populated to be observed directly. However, if there is exchange between the states in a frequency range of $10^0 - 10^2$ s^{-1}, saturation transfer methods can be employed to change the spin population of one state by irradiating the other. The CEST experiment uses this principle by applying a saturating B_1 field at a large series of frequencies covering the entire spectrum. The effects on the resonance peak of the main state are measured. If there is no exchange, the intensity of the peak will diminish only if the frequency of the B_1 field is at or very near its own frequency. However, if there is exchange with some other state at another frequency, saturation of that minor state will be transferred through exchange to the main state. As a result, the peak intensity will also diminish upon saturation of the secondary state. This effect not only demonstrates the presence of chemical exchange, but also allows the position(s) of (a) minor state resonance(s) to be determined, which may hold a clue as to what the minor state could structurally look like. Furthermore, when the power of the B_1 field is varied, the exchange rate and population of the minor state can also be determined.[100]

Dynamics of β-lactamases

Nothing is known about the presence or role of dynamics in BlaC. However, considering the conservation of structure and function, it seems prudent to review what is known about dynamic behaviour of related β-lactamases.

A combination of NMR backbone dynamics studies and molecular dynamics (MD) simulations of class A β-lactamase TEM-1 has revealed that it is very rigid on the pico- to nanosecond time scale, showing almost no local, fast motion. Micro- to millisecond time scale motions were observed in the omega-loop and the vicinity of the active site,[101,102] leading to the proposal of a slow, cavity-filling motion of the Ω-loop. Point mutations of TEM-1 residue 105, which acts as a lid on the active site, resulted in an alteration of the motions in the active site, which could be correlated to the alterations in the catalytic efficiency of the mutants, implying that the dynamics might be involved in catalysis.[103]

Backbone dynamics studies on PSE-4, another class A β-lactamase, yielded similar results. PSE-4 is very rigid in the pico-nanosecond time scale, but shows some micro-millisecond dynamics for several residues near the active site. However, significant dynamics differences with TEM-1 were found for several important residues, emphasising the importance of comparing various β-lactamase variants.[104]

The proposal of Ω-loop motion was corroborated by MD simulations comparing free states to substrate-bound states of both TEM-1 and PSE-4. These simulations revealed a marked flexibility increase of the Ω-loop upon substrate binding.[105,106] A synthetic chimera protein consisting of a TEM-1 enzyme with its Ω-loop replaced by that of PSE-4 was found to display increased slow motions relative to either of its parental enzymes.[107] A reconstruction of an ancient β-lactamase, proposed to be the most likely common ancestor of all gram-negative β-lactamases, was shown to combine a broader substrate profile with an active site with potentially more slow dynamics than modern enzymes.[108–110] This likely reflects the idea that specialised enzymes employ conformational pre-organisation to fit their preferred substrate, whereas generalists use flexibility to adapt to various substrates.

Interestingly, all the NMR spectroscopy studies on class A β-lactamases have yielded high-quality spectra in which only a few of the non-proline residues could not be assigned a resonance peak. In all cases, these residues were located in the active site and included serine 70. This implies that those resonances were broadened beyond detection by some intermediate exchange process specific to the active site. The first direct measurement of motion in the ms time scale ($\sim$50-3000 s^{-1}) by CPMG relaxation dispersion measurements reported only very restricted motions for both TEM-1 and PSE-4. Interestingly, the TEM-1 – PSE-4 chimera mentioned before showed strikingly increased dynamics in this time scale, occurring in a broad region around the active site.[111] The authors speculate that

what they observed may have been a shift in time scale, with the underlying dynamics in the wild type enzymes being too fast for the CPMG experiments to probe. A similar hypothesis was put forth recently to explain markedly increased dynamics in a BlaR1 β-lactamase sensing domain upon binding with a ligand.[112] In that case, the β-lactamase inducer 2-(2'-carboxyphenyl)-benzoyl-6-aminopenicillanic acid (CBAP) shifted the time scale of the otherwise hidden active site dynamics to the slow exchange regime, where it could be identified using NMR. Although BlaR1 is not a β-lactamase, similar mechanisms may well apply to class A β-lactamases. Furthermore, a novel approach based on millisecond hydrogen–deuterium exchange mass spectrometry was used recently to measure solvent accessibility of TEM-1 regions upon engaging in reaction with β-lactams that were either efficiently, slowly or not hydrolysed.[113] Although the resolution of this approach is limited in both space and frequency compared to its NMR-based counterparts, the authors identify several regions in which the dynamics modes associated with the various catalytic processes are clearly distinct, making a valuable contribution to the search for dynamics-based inhibitors.

The relevance of the subject, the elusiveness of β-lactamase intermediate/slow dynamics and their correlation with activity and the possibility of time scale shift upon ligand binding, both in β-lactamase simulations and measurements on related proteins, make it all the more striking that no NMR dynamics measurements on class A β-lactamase / inhibitor complexes have been reported to date. The need for such measurements has been recognised for years.[104] The absence of such data may be due to technical difficulties, as a typical NMR dynamics experiment length of several days restricts this option to extremely stable complexes. This experimental limitation, in turn, takes us back to the need to properly understand such enzyme/inhibitor complexes, the involved mechanisms and the (ir)reversibility of inhibition.

Simulated evolution

To identify mutations that confer resistance, one can look at mechanisms in other β-lactamases and try to rationally extrapolate those to BlaC. As discussed before, however, it can be difficult to predict the effects in a different enzyme due to epistatic mutations.[114] Furthermore, such rational inference only provides a very limited number of possible approaches compared to the available sequence space. Importantly, these approaches tend to be blind to all mechanisms except those that are already known. For these and other reasons, several other techniques have been developed to simulate evolution and identify evolutionary pathways.

Ideally, all possible mutations would be tested. For single mutations, methods have been developed and applied that enable this approach.[115–118] Such saturation mutagenesis was performed for the full TEM-1 protein and combined with functional essays such as Minimal Inhibitory Concentration (MIC) measurements of antibiotics.[119–121] This systematic

approach yields a wealth of information about the effects of single mutations in the studied landscapes. However, without combinations of mutations, no information about epistasis is obtained. This was addressed by Steinberg and Ostermeier,[122] who applied the combination of saturation mutagenesis and functional essays to the TEM-17, TEM-19, and TEM-15 β-lactamase alleles to determine how the different epistatic landscapes affect the effect of single mutations. The comparison of the various landscapes is extremely valuable as it has not only yielded vast amounts of information about these enzymes but also helped to improve our understanding of epistasis in general. However, despite the large investment of time and resources that are required, this approach still yields no data on the feasibility of reaching new functions via combined mutations in the same landscape.

The application of a comprehensive scan to combinatorial mutations would complicate the problem exponentially. In the single amino acid replacement saturation mutagenesis of TEM-1 such as performed by Stiffler *et al.*, the fitness effect of an impressive 4997 mutants (263 positions * 19 mutations) were tested.[121] Should we want to increase the number of mutations from 1 to 2 per mutant, each of the 4997 mutations should be combined with 262 * 19 / 2 = 2489 other mutations, bringing the total number of mutants to be created and tested to 12.4 million. Likewise, at three mutations per mutant this number becomes 21 billion and at 4 mutations the number of mutants to test rises to 25 trillion. Clearly, the mapping of all possible combinations of mutations would be beyond challenging. Fortunately, another technique exists that is considerably less daunting.

The synthesis of gene products by polymerases in the polymerase chain reaction (PCR) can be disturbed by the addition of extra magnesium, manganese and/or skewed nucleotide concentrations. This technique is called error-prone PCR and typically produces a large number of gene products with several single nucleotide mutations each. This approach is also sometimes referred to as random mutagenesis, though in truth, the mutations are not quite random. Firstly, the polymerase has a bias under these conditions for A/T to C/G mutations.[123,124] Secondly, mutations that occur early in the PCR reaction are duplicated in successive steps and therefore overpopulated in the final reaction mixture. Thirdly, certain amino acid mutations on the protein level may be reached through a single base pair mutation on the DNA level, whereas other amino acid mutations require two or three base pair mutations and are thus much less frequent. Nevertheless, error-prone PCR allows the comparatively easy synthesis of extremely large numbers of gene products harbouring semi-random combinations of mutations. Also, it is worth noting that the biases in substitution rates that arise from the error-prone PCR approach actually reflect, to some extent, the same biases that occur in natural evolution, which were shown to suppress deleterious mutations and enrich for adaptive mutations.[125] The obtained gene products can be cloned into bacterial cells to produce the encoded protein. Functional β-lactamases will provide their host cells with resistance to β-lactam antibiotics and can thus be selected *in vivo*. This approach has been applied frequently, yielding useful insights into

both enzymatic function and evolution (e.g. [126–129]). It was applied to BlaC by Feiler *et al.* to identify mutations that increase activity with ampicillin.[30] Here, we will use a double selection pressure, applying both ampicillin and the β-lactamase inhibitor clavulanic acid. The ampicillin will kill our host *Escherichia coli* unless it possesses a functional β-lactamase, while the clavulanic acid will make BlaC dysfunctional unless it acquired mutations that enable it to resist inhibition. This way, we can screen large numbers of BlaC mutant proteins and select only those that have mutated to somehow resist inhibition, while maintaining enough functionality and stability to effectively hydrolyse ampicillin. As we are interested in the evolutionary routes that are available for wild type BlaC, more so than in the pinnacle of resistance that could be reached with BlaC as starting point, we will not apply multiple rounds of directed evolution. Rather, we will apply one round of mutagenesis followed by stringent selection. By sequencing individual mutants, we expect to find the mutations that have recently been reported to increase clavulanic acid resistance and hope to find novel mutations and combinations there-of. Subsequently, we will characterise the identified mutants and identify evolutionary pathways that confer resistance. Ultimately, understanding of these pathways will prove vital in the design of inhibitors with improved resistance to evolution.

Thesis outline

Chapter 1 of this thesis gives a general introduction to BlaC, the questions that were probed in this study and the methodologies that were used. **Chapter 2** shows that unlike what was commonly held previously, clavulanic acid does not irreversibly inhibit BlaC. Instead, the enzyme is able to recover from inhibition after a period of time that we found to depend strongly on the conditions. In particular, we found that the presence of phosphate catalyses the recovery more than 20-fold. **Chapter 3** expands upon the understanding of BlaC with the first description of its internal motions. NMR spectroscopy was used to get an impression of what conformational dynamics are present in BlaC and how they change upon binding by clavulanic acid. It shows that BlaC, like related β-lactamases, is very rigid on the pico-nanosecond time scale, while displaying important millisecond dynamics that are localised specifically in the active site. Furthermore, it is revealed that binding of the inhibitor clavulanic acid causes a major increase of the dynamics on all time scales. In **chapter 4**, random mutagenesis coupled with selective functional screening is applied to identify mutations that increase the ability of BlaC to resist inhibition by clavulanic acid. One inhibitor-resistant mutant is found to display increased slow motions in the active site, while the millisecond motions in another have severely decreased, indicating that similar phenotypic function can be reached through various evolutionary routes. **Chapter 5** comprises a general discussion of the work in this thesis in the perspective of the overarching research questions and applications.

Chapter 2

Phosphate promotes the recovery of *Mycobacterium tuberculosis* β-lactamase from clavulanic acid inhibition

Abstract

The rise of multi- and even totally antibiotic resistant forms of *Mycobacterium tuberculosis* underlines the need for new antibiotics. The pathogen is resistant to β-lactam compounds due to its native serine β-lactamase, BlaC. This resistance can be circumvented by administration of a β-lactamase inhibitor. We studied the interaction between BlaC and the inhibitor clavulanic acid. Our data show hydrolysis of clavulanic acid and recovery of BlaC activity upon prolonged incubation. The rate of clavulanic acid hydrolysis is much higher in the presence of phosphate ions. A specific binding site for phosphate is identified in the active site pocket, both in the crystalline state and in solution. NMR spectroscopy experiments show that phosphate binds to this site with a dissociation constant of 30 mM in the free enzyme. We conclude that inhibition of BlaC by clavulanic acid is reversible and that phosphate ions can promote the hydrolysis of the inhibitor.

Introduction

With antibiotic effectiveness decreasing more rapidly than drug development can counter, the broad range, proven safety and ample availability of β-lactam antibiotics may provide new opportunities for treatment of *Mycobacterium tuberculosis* (Mtb) infection. The native resistance that this bacterium has to β-lactams can be circumvented by inhibition of

BlaC by β-lactam-like suicide substrates. The most common of these inhibitors is clavulanic acid and indeed, combinations of clavulanic acid with β-lactam antibiotics were found to be bactericidal against even extensively drug-resistant Mtb.[47,50,55,59]

Clavulanic acid inhibits BlaC in a substrate-like fashion, forming a covalent bond with the catalytic serine (Ser70 by standard Ambler notation[17]). Generally, in class A β-lactamases, it can then form a variety of covalently bound fragmentation products in the active site, leaving the enzyme either transiently or irreversibly inactivated.[38] For BlaC, several of these products have been found.[18,74,130] Formation of these inactive forms was initially reported to be irreversible in BlaC,[18] but slow recovery of activity was reported thereafter.[41]

A crystal structure of a covalent adduct formed between BlaC and clavulanic acid was published by Tremblay *et al.*[130] Interestingly, this structure models a well resolved phosphate ion in the carboxylate binding site, immediately adjacent to the bond between enzyme and adduct. At the same position, a phosphate ion can also be found in several other BlaC crystal structures.[29,44,131–133] In fact, in 26 of the 29 BlaC crystal structures that have been published to date, this position was found to be occupied by either a phosphate ion or a carboxylate group of the ligand that was used for co-crystallization. Additionally, Xu *et al.* notice that in their structure of BlaC with avibactam (PDB: 4DF6), the sulfate group of the inhibitor occupies this position.[41] The authors of these studies either do not mention the active site phosphate they model, or assume that it is an artefact of the high phosphate concentration under crystallization conditions. We investigated the role of the phosphate ion and demonstrate that it affects the rate of recovery from clavulanic acid inhibition. We also show that a phosphate ion binds to the enzyme in solution in the active site.

Results

BlaC is normally produced by *M. tuberculosis* with an N-terminal Tat-type signal peptide that is used to locate BlaC as a lipoprotein on the outside of the cell membrane.[24,134,135] To obtain soluble protein for *in vitro* experiments, a BlaC gene encoding only the soluble beta-lactamase domain supplemented with a C-terminal 6xHistidine purification tag was expressed in *E. coli*. The protein was isolated and purified using immobilized metal affinity chromatography and subsequent size exclusion chromatography to yield *ca.* 30 mg BlaC per liter of culture medium.

The Michaelis-Menten kinetic parameters of nitrocefin hydrolysis by BlaC were determined in buffers with and without phosphate (Table 2.1, Figure S2.1). The measured Michaelis constant K_m is higher in phosphate buffer than in the other tested buffers. This effect appears to be somewhat compensated by a higher catalytic efficiency at pH 6.

Table 2.1. Buffer dependence of nitrocefin hydrolysis by BlaC. [a]

| Buffer	k_{cat} (s^{-1})	K_m (µM)	k_{cat}/K_m ($\cdot 10^5$ M^{-1}s^{-1})
NaPi pH 6.0	107 ± 6	147 ± 14	7.3 ± 0.4
NaPi pH 7.0	64 ± 6	153 ± 23	4.2 ± 0.2
MES pH 6.0	69 ± 1	38 ± 7	18 ± 3
BIS-TRIS pH 6.0	83 ± 3	61 ± 7	14 ± 1

[a] Buffer concentrations were each 100 mM. Errors represent the standard deviation over triplicate measurements.

These results are in agreement with previously published kinetic values for BlaC nitrocefin hydrolysis, which have k_{cat}/K_m in the range of 4–18 $\cdot 10^5$ M^{-1}s^{-1}.[18,22,29,74] Similar to most of these studies, further experiments have been performed at pH 6.4, which is the optimum pH for BlaC. The work in this study was performed on BlaC with a C-terminal His-tag (Figure S2.2). To ensure that the tag has no effect on the activity, we also prepared BlaC with a cleavable N-terminal His-tag (Figure S2.3). The kinetic parameters of nitrocefin hydrolysis by BlaC without His-tag were then compared to those of the His-tagged BlaC used in this study and were found to be the same, at k_{cat}/K_m of 10 $\cdot 10^5$ M^{-1}s^{-1} and 11 $\cdot 10^5$ M^{-1}s^{-1}, respectively, in 100 mM MES pH 6.4 (Table S2.1).

Next, BlaC inhibition by clavulanic acid was studied. For this, Hugonnet and Blanchard proposed a reactivation model, equation (2.1), including fast binding of the inhibitor I to the enzyme E to form the EI complex, followed by slower conversion to the long-lived EI^* complex.[18]

$$E + I \underset{k_{-1}}{\overset{k_1}{\rightleftharpoons}} EI \underset{k_{-2}}{\overset{k_2}{\rightleftharpoons}} EI^* \qquad (2.1)$$

Using this approach, they determined the affinity constant for BlaC clavulanic acid inhibition ($K_i = k_{-1}/k_1$) to be 12.1 µM, the inactivation rate k_2 2.7 s^{-1} and reactivation rate k_{-2} indistinguishable from zero. This led to the conclusion that clavulanic acid inhibition of BlaC is irreversible. To study the variation of inhibition kinetics with buffer conditions, we used the reactivation model with the adjustment proposed by Xu *et al.*[41] (2.2), in which conversion of covalently bound clavulanic acid EI^* into a product P is allowed with a rate constant k_3, rather than reversal of the covalent linkage to the active site serine residue with a rate constant k_{-2}.

$$E + I \underset{k_{-1}}{\overset{k_1}{\rightleftharpoons}} EI \overset{k_2}{\rightarrow} EI^* \overset{k_3}{\rightarrow} E + P \qquad (2.2)$$
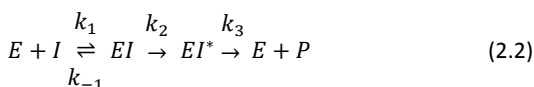
As clavulanic acid acts as a slow-onset inhibitor for BlaC, reaction rates can be estimated from the rate at which enzymatic activity decreases upon administration of the inhibitor.

The resulting inhibition curves are plotted in Figure 2.1 for phosphate buffer and Figure S2.4 for MES buffer. These data were fitted to equation (2.3) to obtain the apparent first-order rate constants (k_{iso}) of inhibition for each clavulanic acid concentration, which were then fitted to equation (2.4) to estimate the rate constants of inhibition (Table 2.2). The mathematical description of k_{iso} given in equation (2.4) is the same for the reactivation model of Hugonnet and Blanchard[18] and the conversion model of Xu *et al.*,[41] except k_{-2} is replaced by k_3. However, the latter model predicts that in time clavulanic acid will be degraded and BlaC will regain activity, whereas the former model predicts that an equilibrium is reached and BlaC will remain inhibited. The latter model applies, as is discussed below.
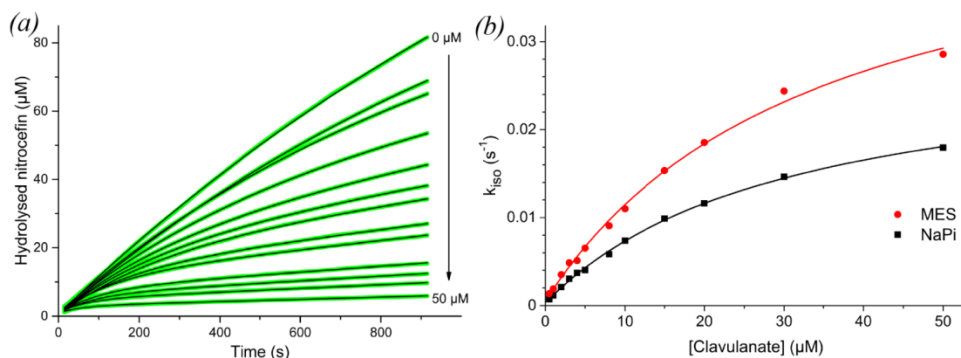

Figure 2.1: *(a)* **Inhibition curves of BlaC nitrocefin hydrolysis with increasing concentrations of clavulanic acid in 100 mM NaPi, pH 6.4.** Green lines represent experimental data, black lines are fits using equation (2.3). *(b)* Plot of k_{iso} values obtained from the fit of each inhibition curve against the respective clavulanic acid concentration, for MES (red circles) as well as NaPi (black squares) buffer. The solid lines represent the fits to equation (2.4).

Table 2.2. Rate constants of BlaC inhibition with clavulanic acid. [a,b]

	Approach	K_i (µM)	k_2 (10^{-2} s^{-1})	k_3 (10^{-4} s^{-1})
NaPi pH 6.4	fit to eq. (2.3) & (2.4)	32 ± 2	2.9 ± 0.1	4 ± 1
	Simulation	20	4.5	18
MES pH 6.4	fit to eq. (2.3) & (2.4)	35 ± 4	4.9 ± 0.3	6 ± 3
	simulation	20	4.5	0.25

[a] Parameters may be correlated, values should therefore be interpreted as indicative.
[b] Errors represent the standard errors of the fit.

The fits of the inhibition curves follow the data remarkably accurately. However, variation of the parameters of the fit shows that they are correlated and other combinations can be obtained that yield equally accurate fits. To evaluate the quality of the data and the values of the parameters, the data were also simulated by solving the differential equations underlying the kinetic model numerically using GNU Octave software. Good simulations

(Figure S2.5) were obtained with the values listed in Table 2.2. All parameters are listed in Table S2.2. These simulations show that curves contain small errors in the offset and in the shape due to measuring artefacts, which are faithfully fitted in the first approach. This suggests that the parameters derived from the k_{iso} curves may not be very accurate, due to overfitting. In short, the method relies on too many parameters to yield quantitative results. It is qualitatively clear, however, that the slopes of the last parts of the curves (i.e. the v_s values in eq. 1, or the k_3 values in the simulations) are close to zero in the presence of high concentrations of clavulanic acid in MES buffer, but not in phosphate buffer. This finding implies that hydrolysis of clavulanic acid by BlaC is much faster in phosphate buffer.

To test the rate of clavulanic acid hydrolysis in a more direct manner, the recovery of activity after inhibition was assayed. BlaC was incubated with a 5-fold excess of clavulanic acid and samples were taken over time and tested for nitrocefin hydrolase activity. Activity was observed to return after a characteristic delay time, reproducible over different batches of enzyme and inhibitor but dependent on reaction conditions (Figure 2.2, Table 2.3). At 20 µM BlaC with 100 µM clavulanic acid in 100 mM MES pH 6.4, Hugonnet and Blanchard[18] observed no return of activity within 12 hours. We find that recovery occurs after *ca.* 14 hours. Moreover, recovery was *ca.* 22 times faster in phosphate buffer than in MES buffer under the same conditions. Addition of sulfate to the MES buffer resulted in *ca.* 7 times faster recovery, whereas addition of acetate slowed the recovery down ca. 2.6 times. Turn-over rates were defined as the number of clavulanic acid molecules inactivated per enzyme molecule per second and were derived from the 50% recovery times. The turn-over rates, listed in Table 2.3, are close to those derived from the simulations of the inhibition data (k_3 values in Table 2.2). Interestingly, at a high concentration of BlaC (300 µM), in 100 mM MES, recovery was found to be about two times faster than that at 100 or 20 µM, with the same clavulanic acid-to-enzyme ratio of 5:1. To investigate whether this was due to an allosteric effect of clavulanic acid at high concentration, the recovery time was measured for solutions with 100 µM BlaC and increasing concentrations of clavulanic acid, from 100 to 1500 µM. The total recovery time increased linearly with the concentration of clavulanic acid (Figure S2.6 and Figure S2.7), indicating that the turn-over rate of BlaC was constant. Thus, it is concluded that the increase in turn-over rate only occurs at very high BlaC concentration (300 µM), perhaps due to a weak protein-protein interaction. However, this effect is unlikely to be relevant under physiological conditions and was not investigated further. No significant concentration dependence of the turn-over rate was seen in phosphate buffer.
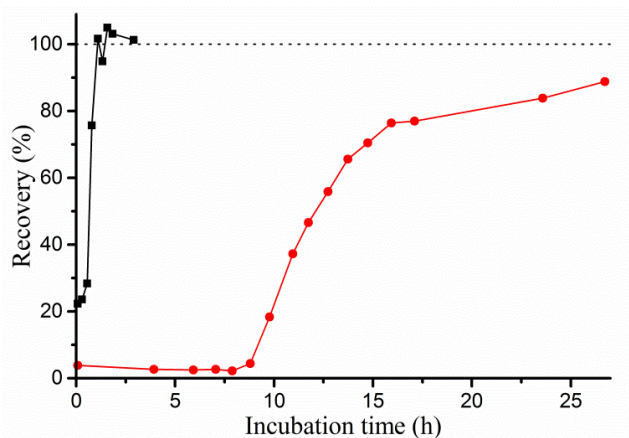
Figure 2.2. Example curves of BlaC recovery from clavulanic acid inhibition. 20 µM BlaC was incubated with 100 µM clavulanic acid in 100 mM NaPi (black squares) or MES (red circles) buffer, pH 6.4. Samples were taken at various time points, diluted to 2.0 nM BlaC and tested for hydrolase activity using 100 µM nitrocefin. BlaC and clavulanic acid separately were each stable throughout the experiments (data not shown). The activity of inhibited enzyme is non-zero due to recovery taking place in the time between initial dilution and activity measurement of the samples (~ 5 min).

Table 2.3. Rates of BlaC activity recovery from clavulanic acid inhibition. [a]

Buffer	[BlaC] (µM)	[Clavulanic acid] (µM)	Ratio	50% recovery time (h)	Turnover rate ($\cdot 10^{-4}$ s^{-1})
MES [b]	20	100	1 : 5	14 ± 1	1.03 ± 0.07
MES [c]	100	100	1 : 1	1.8 ± 0.8	1.5 ± 0.7
MES [c]	100	300	1 : 3	7 ± 0.8	1.2 ± 0.1
MES [c]	100	500	1 : 5	13.8 ± 0.8	1.01 ± 0.06
MES [c]	100	1000	1 : 10	28 ± 0.8	0.99 ± 0.03
MES [c]	100	1500	1 : 15	43.5 ± 1	0.96 ± 0.02
MES [d]	300	1500	1 : 5	6.0 ± 0.6	2.3 ± 0.2
MES + 100 mM acetic acid [c]	100	500	1 : 5	36 ± 3	0.38 ± 0.03
MES + 100 mM Na$_2$SO$_4$ [c]	100	500	1 : 5	2.0 ± 0.5	7 ± 2
NaPi [b]	20	100	1 : 5	0.63 ± 0.06	22 ± 2
NaPi [d]	300	1500	1 : 5	0.82 ± 0.01	16.8 ± 0.3

[a] Buffers were all 100 mM, pH 6.4.
[b] Errors are the standard deviations over 4 replicates.
[c] Errors are the estimated error in half-time determination of single experiments.
[d] Errors are the standard deviations over 2 replicates.

To gain insight in the inhibition intermediates that arise, samples were analyzed using whole-protein mass spectrometry (Figure 2.3). Before inhibition, the enzyme was present in three forms, with the theoretical mass of BlaC as the main species and minor additional

species with relative masses of *ca.* −19 and −35 present. It is unclear how these latter two species differ from the native enzyme or whether this is an artefact of the sample treatment and MS analysis. Upon inhibition with clavulanic acid, these peaks diminish and species of *ca.* +35, +51 and +70 appear instead. The consistent relative intensities and mass differences of +70 relative to the three unbound peaks (−19 + 70 = +51; −35 + 70 = +35) suggest that these peaks represent a single inhibition intermediate. This is likely the propionaldehyde ester that was previously reported upon inhibition of BlaC with clavulanic acid.[18,130] Several other peaks also appear, including *ca.* +86, +136 and +154 species. The *ca.* +86 intermediate has not been observed for inhibition of BlaC with clavulanic acid before, but may correspond to the hydrated propionaldehyde (+88) that was observed upon clavulanic acid inhibition of related β-lactamases.[38] The *ca.* +154 and +136 adducts were previously observed as BlaC clavulanic acid intermediates and these were proposed to represent a decarboxylated *trans*-enamine adduct and its dehydrated variant, respectively.[18,130] Interestingly, although the observed masses are similar to previous results, their relative intensities are not. The BlaC +154 enamine was previously reported as the major dead-end product. However, we observe mainly the +70 aldehyde adduct that was previously reported as minor and decreasing over time. We observed only minor changes in relative intensities upon prolonged incubation, even upon incubating at higher clavulanic acid : BlaC ratios to achieve higher turn-over numbers (Figure 2.3, right). Instead, concurrent with the return of activity, all species were observed to diminish and the original masses returned. Remaining peaks could indicate either irreversible inhibition products or incomplete recovery, but these peaks were relatively low in intensity. Furthermore, although the time required for enzyme recovery was influenced greatly by the presence or absence of phosphate, no effect on the type of intermediates was observed (Figure S2.8).
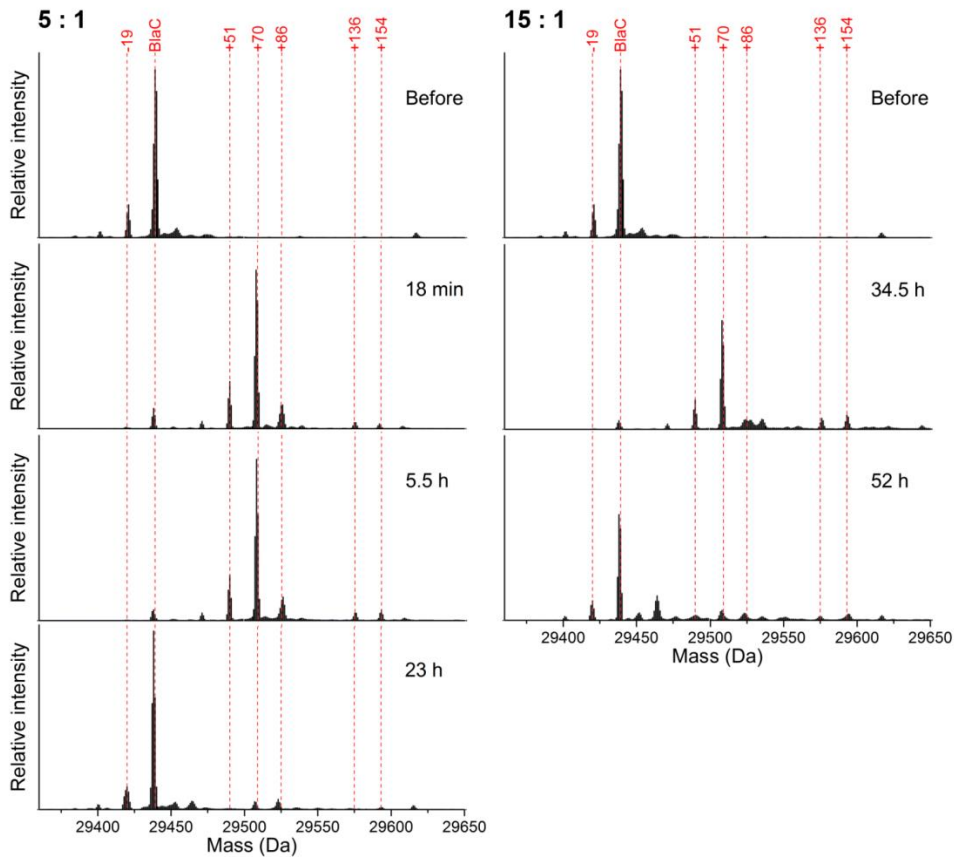
2

Figure 2.3. Charge-deconvoluted mass spectra of BlaC before and during incubation at 100 μM BlaC with 500 (left) or 1500 (right) μM clavulanic acid in 100 mM MES, pH 6.4. Upon inhibition with clavulanic acid, the main species contain covalently bound adducts. After prolonged incubation, the enzyme returns to its free form. The lowest spectra on either side correspond to recovered enzyme activity in the samples. The MS data were obtained using a Waters Synapt mass spectrometer. Each spectrum was normalized to the total signal intensity.

The interaction between phosphate and BlaC was further corroborated by Raffaella Tassoni,[136] who showed specific binding of phosphate in the carboxylate binding site in a 1.19 Å resolution crystal structure (Figure 2.4a). It is available in the Protein Data Bank (PDB) as entry 5NJ2. She furthermore showed that acetate can also bind to this site (Figure 2.4b), this crystal structure is available as PDB entry 5OYO.
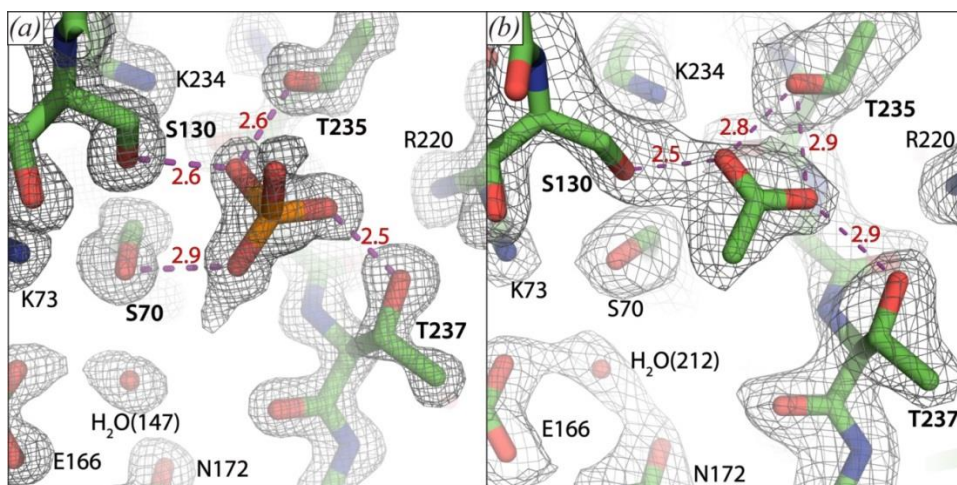
Figure 2.4. Close-up on the carboxylate binding sites of BlaC crystal structures 5NJ2, chain A *(a)* and 5OYO chain B *(b)*. Several catalytically important residues and a conserved active site water molecule are indicated. Distances (in Å) of proposed hydrogen bridges (purple dashed lines) involving the phosphate group and acetate are indicated in red. The mesh shows the $2F_o − F_c$ electron density map contoured at 1.5 σ *(a)* or 1.0 σ *(b)*.

To establish whether BlaC also interacts with phosphate in the solution state, we used nuclear magnetic resonance spectroscopy (NMR). As NMR studies of BlaC have not been reported before, a set of standard 3D NMR spectra was recorded to perform sequential backbone assignment. With these, 98% of the BlaC backbone H-N moieties were assigned to a resonance peak in the corresponding ^{1}H-^{15}N heteronuclear single quantum coherence (HSQC) spectrum (Figure S2.9). Interestingly, the four residues at hydrogen-bonding distance from the active site phosphate (Figure 2.4a) were the only non-proline, non-terminal residues whose backbone resonances could not be identified in the spectra, suggesting that their amide nuclei are in intermediate exchange, causing line broadening of the NMR resonances. The assignment data are available at the Biological Magnetic Resonance Bank under ID 27067.

We then acquired 2D HSQC spectra of BlaC at phosphate concentrations varying from 0 – 250 mM (Figure S2.10). Multiple resonances were found to shift position, indicating that the corresponding residues experience fast exchange between different chemical environments. At low phosphate concentrations only a few peaks were affected, showing large chemical shift perturbations (CSPs, defined as $|Δδ(^1H)| + |0.2*Δδ(^{15}N)|$), whereas CSPs for many resonances were observed at higher phosphate concentrations (>50 mM). When mapped on the protein structure, it becomes apparent that the large CSPs arise for nuclei close to the position in the active site where phosphate is present in the crystal structure (Figure 2.5, left). The smaller CSPs that appear at high phosphate concentration represent much weaker phosphate binding at other sites. The data allowed us to determine the binding affinity in solution. By analyzing the magnitude of active-site CSPs

as a function of the phosphate-BlaC ratio, a binding affinity (K_D) of 27 ± 11 mM was found for phosphate binding to BlaC (Figure 2.5, right). A separate titration with sodium chloride (Figure S2.11) did not result in any CSPs with the magnitude, co-localization or affinity of those found for phosphate, confirming that the observed effects are caused by a specific interaction.
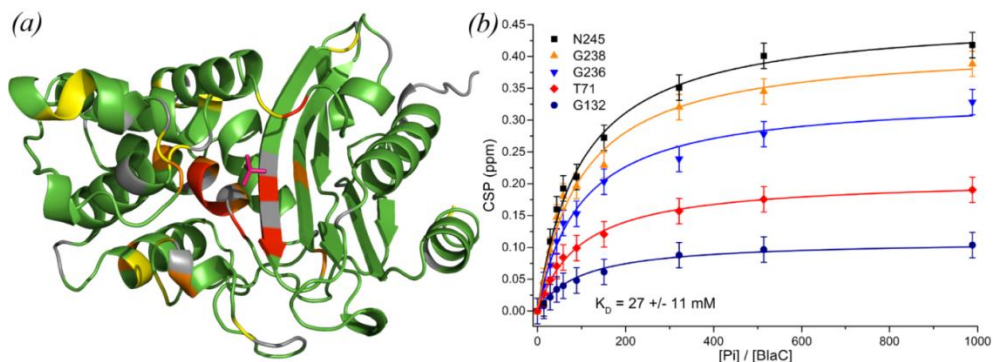

Figure 2.5. BlaC-phosphate interaction. *(a)* Crystal structure 5NJ2 is shown with residues that are affected by phosphate binding in solution highlighted. Residues of which the amide backbone experienced CSPs over 0.075, 0.10 and 0.15 ppm are displayed in yellow, orange and red, respectively, whereas the ones for which no data were available are displayed in grey and those with no or small CSPs are colored green. The phosphate as observed in the crystal structure is indicated in magenta. *(b)* Binding curves. The plot shows the CSPs upon phosphate titration for five selected amide resonances plotted against the ratio of the phosphate and BlaC concentrations. Data points are shown with an estimated peak picking error of ±0.02 ppm, error in K_D is the standard deviation over duplicate titrations.

NMR spectroscopy was also used to study the BlaC clavulanic acid interaction. Upon addition of a fivefold excess of clavulanic acid, several peaks disappeared and new peaks appeared nearby. Unsurprisingly, the corresponding nuclei were located in the active site (Figure 2.6a). Upon prolonged incubation, the peaks of the unbound state reappeared and the peaks of the bound state disappeared. This observation indicates that the free and bound forms are not in exchange on the chemical shift time scale (exchange rate << 100 s^{-1}), in line with the expected formation of a covalent intermediate. The recovery times of free BlaC after incubation with fivefold excess of clavulanic acid based on the NMR peak intensities (Figure 2.6b) were in agreement with the kinetics and MS data (Table 2.3), including data taken directly on the NMR samples.
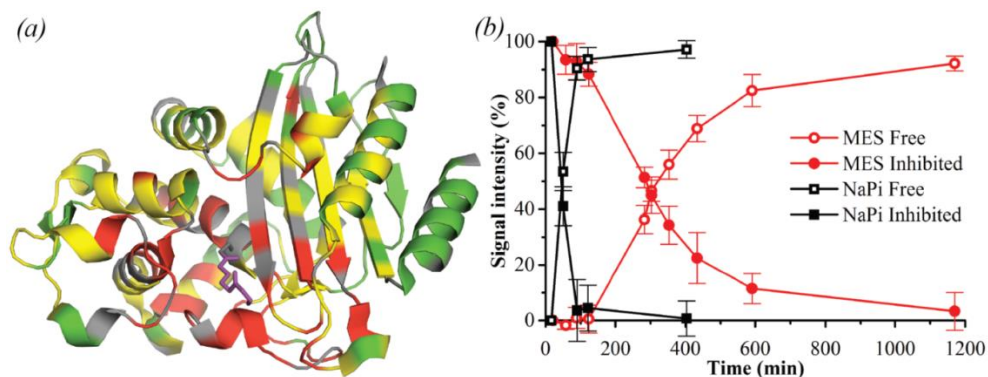
Figure 2.6. Effect of clavulanic acid on BlaC as measured by NMR. *(a)* Crystal structure 3CG5[130], highlighting residues of which NMR resonances are affected by addition of clavulanic acid. Residues of which the amide backbone resonance experienced CSPs over 0.01 ppm and over 0.05 ppm are displayed in yellow and red, respectively, while the ones for which no data were available are displayed in grey and the remaining residues in green. The bound reacted adduct of clavulanic acid as was observed by Tremblay *et. al.*[130] is shown in purple sticks. *(b)* Effect of clavulanic acid on BlaC over time, in 100 mM MES (red circles) and NaPi (black squares) buffer, pH 6.4. Data points show average and standard deviation of relative signal intensities from the native (open symbols) and inhibited (filled symbols) resonances of residues Cys69, Ala74, Asp131, Ala146 and Tyr241.

Discussion

In this work, BlaC and its interaction with clavulanic acid were further characterized *in vitro*. The Michaelis-Menten kinetic values found for nitrocefin hydrolysis are largely consistent with previous observations, although an elevation of the Michaelis constant was observed in the presence of phosphate. This may point toward competition between phosphate and substrate for occupation of the carboxylate binding site. This explanation would lend further credence to the suggestion by Kurz *et al.*[42] that the same competition may explain their observation of an oddly placed carbonyl moiety in co-crystallization of BlaC with a boronic acid transition state inhibitor. To determine the reaction rates with clavulanic acid, the model proposed by Xu *et al.*[41] was used (eq. 7). It should be noted that clavulanic acid chemistry may be more complicated than this model suggests, as various inhibition intermediates have been reported[18,130] and observed in this study. Presumably, different inhibition intermediates will have different rates of formation and decomposition.

The approach of fitting inhibition curves to initial and final velocities (v_i and v_s) and an exponential decay constant (k_{iso}) that describes the time to reach a steady state inhibition level, has been used frequently. Our simulations of the curves suggest that the method may lead to overfitting of the parameters and should be used with caution. In particular the rate constant for hydrolysis of the covalent intermediate (k_3) is poorly defined. This

rate is very low and its value depends heavily on the fits of the lowest inhibitor concentrations. The parameters of clavulanic acid inhibition onset that we found are in reasonable agreement with the K_i = 12.1 μM and k_2 = 2.7 s^{-1} found by Hugonnet and Blanchard,[18] who used the same approach described here except for their assumption that the covalent intermediate is not hydrolyzed (k_3 = 0). We found that BlaC slowly converts clavulanic acid to regain activity, consistent with the observations of Xu *et al.*[41] The return to the native active form of the protein was demonstrated by activity assays, NMR spectroscopy and mass spectrometry.

The main covalent intermediate of inhibition was observed to harbor a *ca.* +70 mass compared to the non-inhibited protein, corresponding to the adducts observed by Hugonnet and Blanchard[18] upon inhibition with each of the inhibitors clavulanic acid, sulbactam and tazobactam and proposed by them and others to be a hydrolysable aldehyde adduct. However, the +136 and +154 clavulanic acid enamine adducts observed as main, dead-end, reaction products by Hugonnet and Blanchard[18] as well as Xu *et al.*[130] were observed in only minor quantities in our analysis. We demonstrate that the rate of recovery is highly dependent on reaction conditions. Phosphate ions enhance the rate, yet the composition of the inhibition intermediates is not affected. This indicates that phosphate promotes the release of covalently bound clavulanic acid adducts from the active site and does not change the direction of the initial chemistry. NMR experiments support phosphate ion binding in the active site and show that the dissociation constant is 3×10^{-2} M. This affinity requires that at crystallization conditions of 2 M phosphate, the site should be fully occupied. This is consistent with the observations published so far. We note that structure 2GDN is the only BlaC structure that was modelled with an empty carboxylate binding site, despite a high phosphate concentration in the crystallization buffer, but the data do show density that suggests the presence of a phosphate ion there. The high resolution structure by Raffaella Tassoni shows that the phosphate is in hydrogen bond distance to several important active site residues and may be protonated at the phosphate oxygen close to Ser70.

To formulate a hypothesis about the role of phosphate in promoting hydrolysis, we examined the structure of BlaC covalently bound to a cleavage product of clavulanic acid (PDB entry 3CG5,[130] Figure 2.7). It should be noted that the intermediate in structure 3CG5 is not the dominant species observed in our work, of +70 Da, but the ester bond to Ser70 is likely to be in a similar place in all intermediates. In this structure, a phosphate (PO$_4$ 309) is present in the same location as in the structure of substrate free BlaC, although it is slightly displaced by the presence of the adduct. Most likely, the carboxylate binding site is also involved in the initial interaction between BlaC and the carboxy group of clavulanic acid, but it becomes available upon decarboxylation of the acyclic adduct. This reaction occurs rapidly and appears to create enough space to allow for diffusion of phosphate into the carboxylate binding site. In the second step of the reaction, a nucleophilic attack on

the carbon (atom CAG in structure 3CG5) of the adduct forming the ester bond with Ser70 occurs, the bond between Ser70 and the adduct is broken, and Ser130 O_γ is reprotonated. The nucleophilic attack can be executed by water 441, located at 3.1 Å underneath the ester bond plane and hydrogen bonded to Glu166. This is the standard mechanism of β-lactamase hydrolysis. However, O_3 of the phosphate is located also at 3.1 Å of the CAG carbon and right above the ester bond plane. So, alternatively, the phosphate could carry out the nucleophilic attack. After release from the enzyme, the phospho-adduct would probably be rapidly hydrolyzed.

Figure 2.7. Schematic representation of catalytically important groups and their hydrogen-bonding network, as present in structure 3CG5[130] **of BlaC with a clavulanic acid cleavage product (indicated in blue) covalently bound to Ser70.** Distances (in Å) between heavy atoms involved in potential H-bonds are shown in red. Residues are numbered according to the Ambler consensus,[17] other numbers represent the internal numbering of the published structure.

An alternative role of the phosphate could be in reprotonation of the Ser70 O_γ. The distance between the phosphate oxygen O_3 and the Ser70 O_γ is larger (3.5 Å) than in the substrate free structure (2.9 Å, Figure 2.4a) but it is close to the O_γ of Ser130 (2.5 Å). If the nucleophilic attack is performed by the water, a proton would be donated to Glu166. This glutamate is hydrogen bonded to the amine of Lys73, which also forms an H-bond with Ser70 O_γ, allowing for proton transfer to Ser. Alternatively, the Ser70 O_γ could be reprotonated by accepting the proton from Ser130 (O-O distance 2.7 Å), which in its turn accepts a proton from O_3 of the phosphate (Figure 2.7). The phosphate is in contact with waters on the protein surface (HOH 492, 500 and 516). In this case, Glu166 could release its proton by a flip of the carboxy group and donation of a proton to the nearby water chain (HOH 586 and HOH 587).

Our data show that sulfate can also accelerate hydrolysis of clavulanic acid, albeit less than phosphate. It can be expected that the sulfate ion is fully deprotonated at pH 6.4, so it could not act as a hydrogen donor to Ser130. However, it could act as a nucleophile to attack carbon CAG. One BlaC structure, PDB 3ZHH,[30] shows sulfate bound in the carboxylate binding site, in a similar location as the phosphate. The limited resolution does not allow for a detailed analysis. Raffaella Tassoni also solved the structure of BlaC with excess acetate. Acetate in MES buffer has a negative effect on the hydrolysis rate as compared to MES buffer only. This observation cannot be readily explained, but the data show acetate binding in the carboxylate binding site. It forms a hydrogen bond with Ser130, so could act as a hydrogen bond donor. In an overlay of 3CG5 and our structure 5OYO, it can be seen that the closest oxygen of the acetate is at 4.2 Å of the CAG carbon, making a nucleophilic attack unlikely. We cannot exclude that MES buffer (2-(N-morpholino)ethanesulfonic acid) can bind to the carboxylate binding site as well, via its sulfonate group, having a weak positive effect on the rate of hydrolysis. Acetate could be competing with MES, leading to a reduction of the rate. These considerations point to a role of phosphate and sulfate as alternative nucleophiles. We emphasize, however, that the proposed mechanisms are speculative. Further research is required to understand the influence of anions on the hydrolysis rate of clavulanic acid. Clearly, the binding site is promiscuous and various ions have quite different effects on hydrolysis.

It is worthwhile to consider whether the effect we observe is specific for BlaC, or if it may signify a more general mechanism in class A β-lactamases. Indeed, related proteins such as TEM-1, SHV-1 and CTX-M-1 have very similar carboxylate binding sites. However, most of these enzymes harbor an Ala at position 237, where BlaC has a Thr, which contributes a hydrogen bond to the binding of phosphate (Figure 2.4a). Indeed, although phosphates and sulfates have been observed to occupy analogous positions in at least TEM-1,[32] CTX-M-9[137] and L2,[138] many x-ray structures of these enzymes with empty carboxylate binding site have also been reported (e.g. structure 3CMZ[139] of TEM-1 and structure 1SHV[33] of SHV-1). These observations suggest that the affinities between these proteins and phosphate-like groups may be lower than in the case of BlaC. We therefore expect any effect of phosphate in related enzymes to be less significant. Whether the role of phosphate and other anions in the breakdown of clavulanic acid by BlaC is relevant under physiological conditions is unclear. *M. tuberculosis* is known to prevent maturation of lysosomes by blocking phagolysosomal fusion and has been shown to live at slightly acidic pH.[140] The experiments reported here have been conducted at pH 6.4, which is the optimal pH of BlaC and can thus be expected to be physiologically relevant. The concentration of phosphate ions in *M. tuberculosis* within macrophages is unknown. Total prokaryotic and eukaryotic intracellular phosphate ion concentrations, however, are in the 1 – 10 mM range.[141] Additionally, sulfate ions were observed to have a similar effect and it cannot be excluded that other compounds, such as ATP, can also interact with BlaC. Thus,

it is reasonable to expect that a substantial fraction of BlaC molecules binds a phosphate-like group specifically in the active site.

Materials And Methods

Materials

NMR analysis indicated that the nitrocefin purchased from BioVision Inc. and Oxoid Limited was significantly purer than that from Cayman Chemicals. The BioVision nitrocefin was used in this study. Several values have been reported for the change in extinction coefficient upon hydrolysis of nitrocefin (e.g. [22,74]). To determine this value independently, a stock solution containing 5.0 mg of nitrocefin was diluted to a range of seven concentrations from 10-75 µM in 100 mM sodium phosphate buffer, pH 6.4. The A_{486} values before and after complete hydrolysis by 20 minutes incubation with 5 nM BlaC were determined. The slope of a linear fit of ΔA_{486} against nitrocefin concentration yielded $\Delta\varepsilon_{486}$. The procedure was performed in duplicate, yielding a $\Delta\varepsilon_{486}$ of 17 ± 1 mM^{-1} cm^{-1}. Clavulanic acid powder is hygroscopic, so its concentration was determined by the absorbance at 256 nm in NaOH. The extinction coefficient was determined by quantitative NMR versus a standard of trimethylsilylpropanoic acid. For ChemCruz and Matrix clavulanic acid, which are sold in a cellulose matrix, we found identical UV-Vis spectra, yielding an absorbance at 256 nm of $20.0 +/- 0.1$ mM^{-1} cm^{-1}. For TRC clavulanic acid, which is a pure powder, the UV-vis spectrum is clearly different and the NMR spectrum shows impurities. The extinction coefficient at 256 nm is 18.7 mM^{-1} cm^{-1}.

Production and purification of BlaC

The *blaC* gene, lacking codons for the N-terminal 42 amino acids that constitute the signal peptide and with the addition of a C-terminal histidine tag (Uniprot P9WKD3 modified as specified in Figure S2.2), was expressed using a host optimized sequence (ThermoFisher Scientific), cloned in the pET28a vector in *Escherichia coli* BL21 (DE3) pLysS cells. The cells were cultured in LB medium at 310 K until the optical density at 600 nm reached 0.6, at which point expression was induced with 1 mM IPTG and incubation continued at 289 K overnight. For the production of isotope labelled proteins for NMR experiments, LB medium was replaced with M9 medium (Table S2.3) containing ^{15}N ammonium chloride (0.3 g/L) as the sole nitrogen source and, where necessary, ^{13}C D-glucose (4.0 g/L) and ^{2}H$_2$O (99.8%) as carbon and hydrogen source, respectively. Cells were harvested by centrifugation and lysed with a French press in a buffer of 50 mM Tris-HCl pH 7.5 containing 500 mM NaCl. After centrifugation, the soluble fraction was loaded on a HisTrap Nickel column (GE Healthcare) and eluted with a gradient of 0 - 250 mM imidazole in the same buffer. A Superose 12 10/300 GL size exclusion chromatography column (GE Healthcare) was used for further purification. Protein concentration and buffer exchange were performed using 10 kDa cut-off Amicon Ultra centrifugal filter units (Merck Millipore

Ltd). Protein purity was determined by SDS-PAGE (Figure S2.12) and concentrations were determined by the absorption at 280 nm, using the theoretical extinction coefficient ε_{280} = 29910 M^{-1} cm^{-1}.[142] BlaC with a TEV-cleavable His-tag (sequence specified in Figure S2.3) was produced in the same way, with additional cleavage of the purified protein by His-tagged TEV protease. Subsequent re-purification using another HisTrap Nickel column (GE Healthcare) yielded pure, His-tag-less BlaC in the flowthrough. Cleavage was confirmed by MS using a Waters Synapt spectrometer yielding a mass of 28637 ±1 Da, corresponding with 100% cleavage and 96% efficiency of the applied ^{15}N-labelling. No other protein forms, such as the non-cleaved construct (expected mass 31770 Da at 96% [15]N labelling), were detected in the final sample.

Kinetics

All kinetic measurements were performed by measuring hydrolysis of the chromogenic reporter substrate nitrocefin at 486 nm, using a Perkin-Elmer Lambda 800 UV-VIS spectrometer thermostated at 298 K. To determine Michaelis-Menten kinetic constants, initial nitrocefin hydrolysis rates by 5.4 nM BlaC were measured in 100 mM of the specified buffers, in triplicate. OriginPro 9.1 was used to fit standard Michaelis-Menten curves to these data. Reported are, for each condition, the average and standard deviation of the three independent fits.

The apparent first-order rate constants of inhibition (k_{iso}) were obtained by fitting the hydrolysis of 125 µM nitrocefin by 2 nM BlaC in the presence of various concentrations of clavulanic acid against equation (2.3).[18]
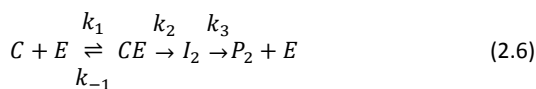
$$[P] = v_s\, t + \frac{v_i - v_s}{k_{iso}} [1 - e^{-k_{iso}\, t}] \qquad (2.3)$$

[P] Is the concentration of product in µM, v_s and v_i are the final and initial reaction velocities in the presence of inhibitor in µM s^{-1}, respectively, t is time in s and k_{iso} is the apparent first-order rate constant for the progression from v_i to v_s in s^{-1}. Subsequently, the rate constants of inhibition were obtained by fitting these data against Equation (2.4),[41] in which k_3 and k_2 are the rate constants for step 3 and 2 in the conversion model (2.2) (see Results section), respectively, while K_i is the ratio k_{-1} / k_1 in that model.

$$k_{iso} = k_3 + \frac{k_2\,[I]}{K_i + [I]} \qquad (2.4)$$

The data were also simulated using GNU Octave 3.2.4 and numerical simulations of the differential equations derived from the following model.

$$N + E \; \underset{k_{-a}}{\overset{k_a}{\rightleftharpoons}} \; NE \xrightarrow{k_b} I_1 \xrightarrow{k_c} P_1 + E \qquad (2.5)$$

$$C + E \underset{k_{-1}}{\overset{k_1}{\rightleftharpoons}} CE \overset{k_2}{\rightarrow} I_2 \overset{k_3}{\rightarrow} P_2 + E \qquad\qquad (2.6)$$
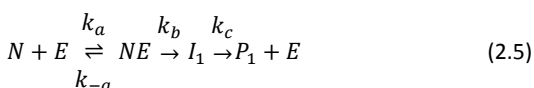
Where (2.5) and (2.6) describe the conversion of nitrocefin (N) and clavulanic acid (C), respectively. E is the enzyme, NE and CE are the non-covalent complexes and I_i and P_i represent the covalent intermediates and the products, respectively. An example script is provided as Supplementary material. Equation (2.6) is equivalent to the conversion model, discussed in the Results section (2.2).

Inhibition recovery

All samples for inhibition recovery experiments were thermostated at 298 K, at the concentrations indicated in Table 2.3. Activity measurements were performed by dilution in buffer without inhibitor to a final concentration of 2 nM BlaC with 100 µM nitrocefin. The time between initial dilution and measurement was kept <5 minutes and the reported time is that of the measurement. Separate incubations were performed to test the stability of BlaC without clavulanic acid, as well as clavulanic acid without BlaC.

Mass spectrometry

Samples for whole-protein mass spectrometry were flash-frozen in liquid nitrogen and stored at 193 K. Upon thawing, they were transferred to 10 mM ammonium acetate buffer pH 6.8 using Micro Bio-Spin® Chromatography Columns (Bio-Rad), loaded on a C4 polymeric reversed phase UPLC column and then analyzed using either an LTQ-Orbitrap mass spectrometer (ThermoScientific) or a Synapt G2-Si mass spectrometer (Waters), 10-25 minutes after thawing. Data were deconvoluted for charge using Thermo Xcalibur.

Nuclear Magnetic Resonance spectroscopy experiments

Samples for backbone assignment contained 0.75 mM [^{15}N,^{13}C,^{2}H] BlaC in 20 mM MES pH 6.0 with 1 mM DTT and 6% D$_2$O (NMR buffer) at 298 K. A set of standard HNCA, HNCACB, HNcoCACB, HNCO and HNcaCO experiments was recorded on a Bruker AVIII HD 850 MHz spectrometer equipped with a TCI cryoprobe for backbone assignment. All other NMR spectra, unless stated otherwise, were recorded on *ca.* 0.35 mM [^{15}N] BlaC samples in the same buffer at 298 K, on the same spectrometer. Data were processed with Topspin 3.2 (Bruker Biospin, Leiderdorp) and analyzed using CCPNmr Analysis.[143]

NMR titrations were performed by addition of an increasing volume of 0.9 M sodium phosphate or sodium chloride stock in NMR buffer to the sample, decreasing protein concentration from 0.35 to 0.25 mM during the titration. Non-linear regression fitting with a shared association constant (K_A) and individual maximal chemical shift perturbations (CSP) values (CSP_{max}) in Origin 9.1 was used to fit the CSP data of selected residues to Equation (2.7), in which R is the ratio of phosphate concentration over enzyme concentration, C_{stock} is the concentration of the phosphate stock solution used for titrating

and E_i is the initial concentration of enzyme in the sample. The phosphate titration was performed in duplicate. As the inter-experimental variation between samples was found to be larger than the intra-experimental variation between reporter peaks, data from the two experiments were fitted separately. Reported are the average and standard deviation of the two fits.

$$CSP = 0.5\, CSP_{max} \left(A - \sqrt{A^2 - 4R} \right)$$
$$A = 1 + R + \frac{C_{stock} + E_i\, R}{C_{stock}\, E_i\, K_A} \qquad (2.7)$$

Samples for NMR visualization of BlaC recovery from clavulanic acid inhibition contained 0.3 mM [^{15}N] BlaC and 1.5 mM clavulanic acid in 100 mM MES or sodium phosphate buffer, pH 6.4, with 1 mM DTT and 6% D$_2$O, at 298 K. Activity measurements as described above were performed at various time points to check the relation between spectra and functional states. Separate incubations were performed as controls on the stability of BlaC without clavulanic acid, as well as clavulanic acid without BlaC.

Supplementary material

Supplementary Tables

Table S2.1. Nitrocefin hydrolysis by BlaC with and without His-tag. [a]

BlaC	k_{cat} (s^{-1})	K_m (µM)	k_{cat}/K_m ($\cdot 10^5$ M^{-1}s^{-1})
His-tagged	81 ± 7	73 ± 3	11.1 ± 0.4
Not tagged	77 ± 1	80 ± 1	9.5 ± 0.1

[a] Buffer was 100 mM MES, pH 6.4. Errors represent the standard deviation over duplicate measurements.

Table S2.2. Simulation parameters of BlaC inhibition by clavulanic acid. [a]

	K_D [b] (µM)	k_a (µM^{-1}s^{-1})	k_b (s^{-1})	k_c (s^{-1})	K_I (µM)	k_1 (µM^{-1}s^{-1})	k_2 (s^{-1})	k_3 (10^{-4} s^{-1})
MES 100 mM, pH 6.4	170	1.05	3000	148	20	1	0.045	0.25
NaP$_i$, 100 mM, pH 6.4	220	1.05	2500	103	20	1	0.045	18

[a] The parameters used for the simulations shown in Figure S2.5 are listed. The model is described in equations (2.5) and (2.6). Note that some parameters are correlated and the values should be considered as indicative. The large difference in k_3 under different buffer conditions is, however, very significant. The concentrations of BlaC and nitrocefin were 2 nM and 125 µM, respectively.
[b] $K_D = k_{-a}/k_a$

Table S2.3. M9 medium constituents per liter, in MilliQ water.

KH_2PO_4	13.0 g
K_2HPO_4	10.0 g
Na_2HPO_4	9.0 g
Na_2SO_4	2.4 g
$^{15}NH_4Cl$	0.3 g
Glucose	4.0 g
thiamine	30 mg
$MgCl_2$	2 g
Biotin	1 mg
Choline chloride	1 mg
Folic acid	1 mg
Niacinamide	1 mg
D-pantothenate	1 mg
Pyridoxal	1 mg
Riboflavin	0.1 mg
$FeSO_4$ (7 H_2O)	10 mg
$CaCl_2$ (2 H_2O)	60 mg
$MnCl_2$ (4 H_2O)	12 mg
$CoCl_2$ (6 H_2O)	8 mg
$ZnSO_4$ (7 H_2O)	7 mg
$CuCl_2$ (2 H_2O)	3 mg
H_3BO_3	0.2 mg
EDTA	50 mg

2

Supplementary figures
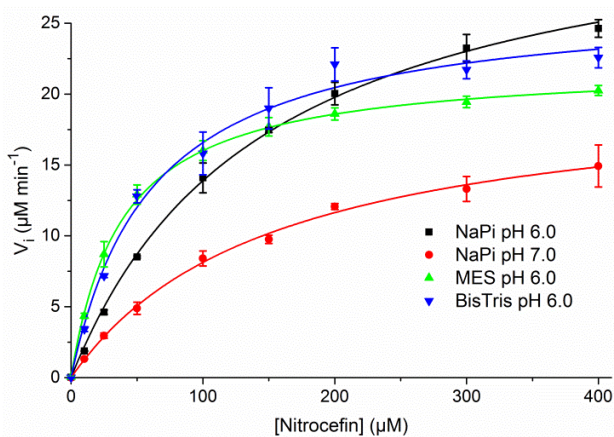
Figure S2.1. Michaelis-Menten curves for the hydrolysis of nitrocefin by 5.4 nM BlaC in various buffers. Error bars represent standard deviation of triplicate measurements.

Figure S2.2. Amino acid sequence of the BlaC protein used in this chapter. The upper numbering corresponds to the actual sequence, the lower to the Ambler notation.[S1] Residues 2-266 (upper numbering) are residues 43-307 of BlaC Uniprot sequence P9WKD3-1. The His-tag residues are highlighted in grey.

```
-26            -16          -6       0
 MGSSHHHHHH SSGLVPRGSH MENLYFQ


1              11           21           31           41           51
GDLADRFAEL ERRYDARLGV YVPATGTTAA IEYRADERFA FCSTFKAPLV AAVLHQNPLT
   30             40           50           60           70           80      88

61             71           81           91           101          111
HLDKLITYTS DDIRSISPVA QQHVQTGMTI GQLCDAAIRY SDGTAANLLL ADLGGPGGGT
90             100          110          120          130          140   145 145

121            131          141          151          161          171
AAFTGYLRSL GDTVSRLDAE EPELNRDPPG DERDTTTPHA IALVLQQLVL GNALPPDKRA
   150            160          170          180          190          200

181            191          201          211          221          231
LLTDWMARNT TGAKRIRAGF PADWKVIDKT GTGDYGRAND IAVVWSPTGV PYVVAVMSDR
   210            220          230          240          250          260     267

241            251          261
AGGGYDAEPR EALLAEAATC VAGVLA
   270            280          290
```

Figure S2.3. Amino acid sequence of the BlaC protein with cleavable His-tag. The upper numbering corresponds to the sequence of the protein after cleavage, the lower to the Ambler notation.[S1] Residues 2-266 (upper numbering) are residues 43-307 of BlaC Uniprot sequence P9WKD3-1. The residues of the TEV-cleavable His-tag are highlighted in grey. The sequence after cleavage with TEV protease (residues 1-266, no highlight) is the same as that shown in Figure S2.2, except that the N-terminal Met in that sequence is replaced by Gly and the eight residues constituting the C-terminal His-tag are lacking.
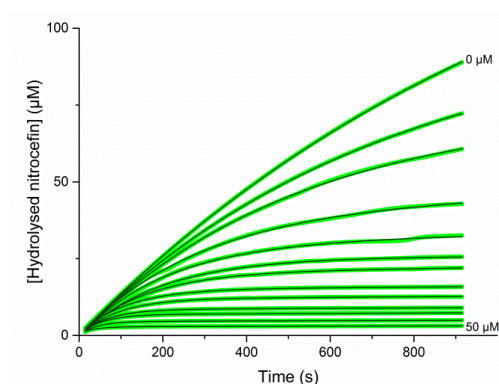
Figure S2.4. Inhibition curves of BlaC nitrocefin hydrolysis with increasing concentrations of clavulanic acid in 100 mM MES buffer pH6.4. Green lines represent experimental data, black lines are fits using equation 1.
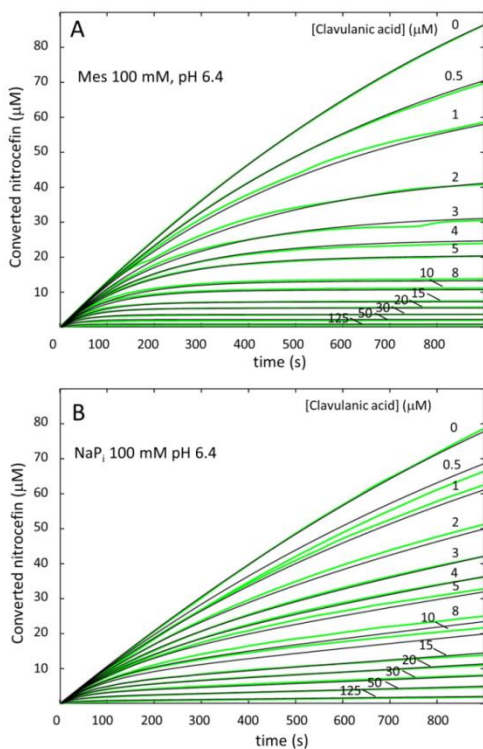
2

Figure S2.5. Inhibition of BlaC nitrocefin hydrolysis by clavulanic acid, in MES buffer (A) and phosphate buffer (B). The experimental curves (green) were simulated using GNU Octave software (black) and the models described in equations (2.5) and (2.6). [Nitrocefin], 125 µM; [BlaC], 2 nM; temperature, 298 K. The concentrations of clavulanic acid and the buffer conditions are indicated. Note the difference in the slopes of the curves at the end of the experiments. The larger slopes in NaP$_i$ buffer reflect the larger hydrolysis of BlaC-clavulanic acid intermediate (rate constant k_3).
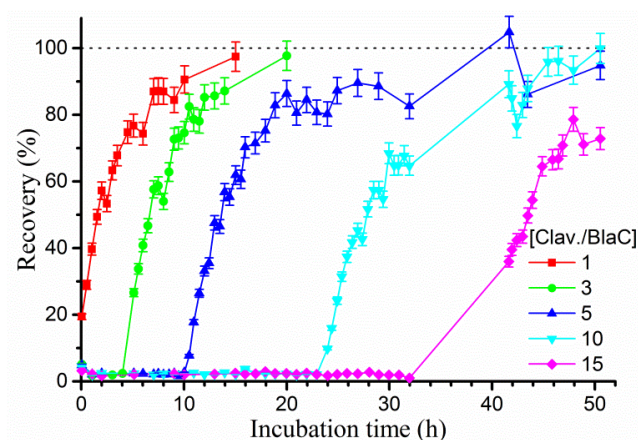
Figure S2.6. BlaC recovery from clavulanic acid inhibition with varying inhibitor / enzyme ratios. BlaC (100 μM) was incubated with 0.1, 0.3, 0.5, 1 and 1.5 mM clavulanic acid, respectively. Samples were taken at various time points, diluted to 2.0 nM BlaC and tested for hydrolase activity using 100 μM nitrocefin. Between 32 and 41.5 h, no measurements were performed due to a technical failure. The error bars are relative to the activity and represent the standard deviation in the 100% activity control measurements.
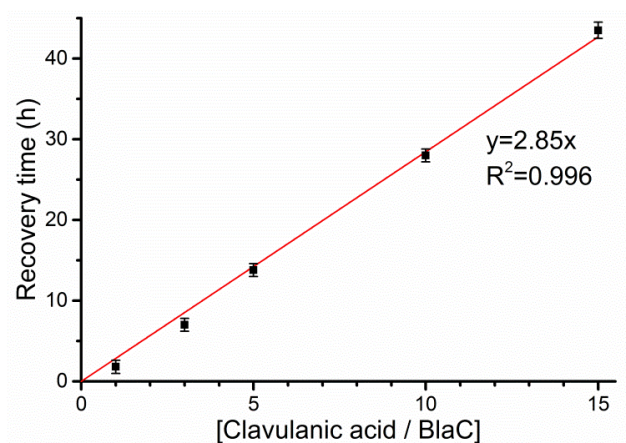
Figure S2.7. Relation between recovery time and molar ratio of enzyme and inhibitor. Recovery times (black squares) are the incubation times required to reach 50% activity, as estimated from Figure S2.6. Error bars represent the estimated error in reading recovery times from single curves. The text inset describes the linear fit through the origin, consistent with a first order reaction (red line). The slope represents the turn-over rate in h^{-1}.

2
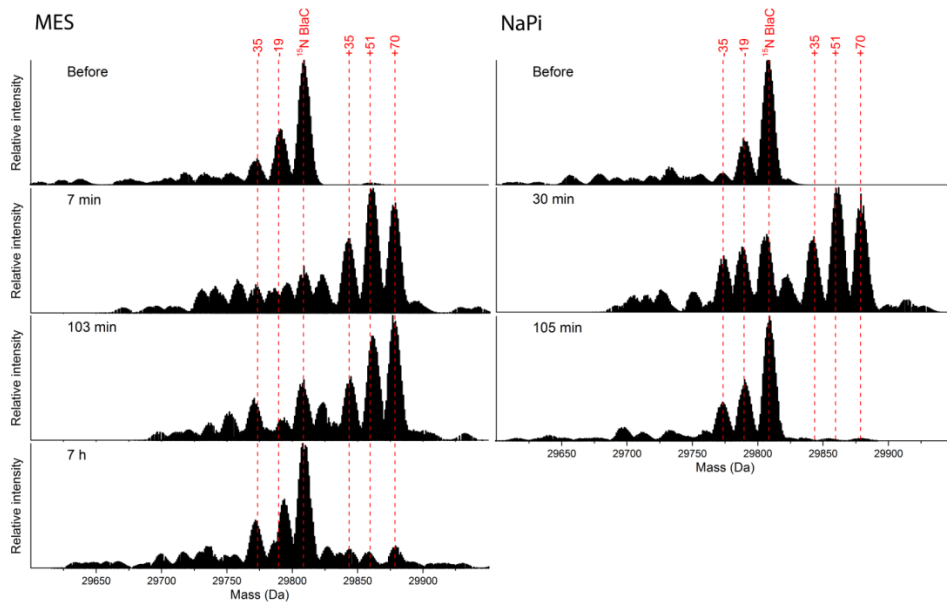
Figure S2.8. Charge-deconvoluted ThermoScientific Orbitrap mass spectra of BlaC before and during incubation with 1.5 mM clavulanic acid (protein: clavulanic acid ratio 1:5) in 100 mM MES (left) or NaPi (right) buffer, pH 6.4. Upon inhibition with clavulanic acid, the main species contain covalently bound adducts. After prolonged incubation, the enzyme returns to its free form in either buffer, but with different rates. For this experiment, ^{15}N labelled BlaC was used. This sample was also used in the NMR experiment. Each spectrum was normalised to the highest signal intensity.

Figure S2.9. TROSY-HSQC spectrum of BlaC with residue assignments. 'NE' labels indicate arginine amide ε signals, 'NE1' labels indicate tryptophan amide ε1 signals. Numbering refers to the protein as it was measured, conversion to the Ambler numbering scheme can be found in Figure S2.2. The assignment can be accessed under Biological Magnetic Resonance Bank ID 27067.

2

Figure S2.10. Overlay of ^{1}H-^{15}N HSQC spectra of BlaC upon titration with phosphate. The sample contained 350 μM BlaC, 20 mM MES buffer, pH 6.2, 1 mM DTT, 6% D_2O, without (blue peaks) and with 5 mM (magenta), 10 mM (purple), 15 mM (pink), 20 mM (red), 30 mM (orange), 50 mM (lime), 100 mM (green), 150 mM (teal) or 250 mM (black) of sodium phosphate, respectively. Selected residue numbers are shown.
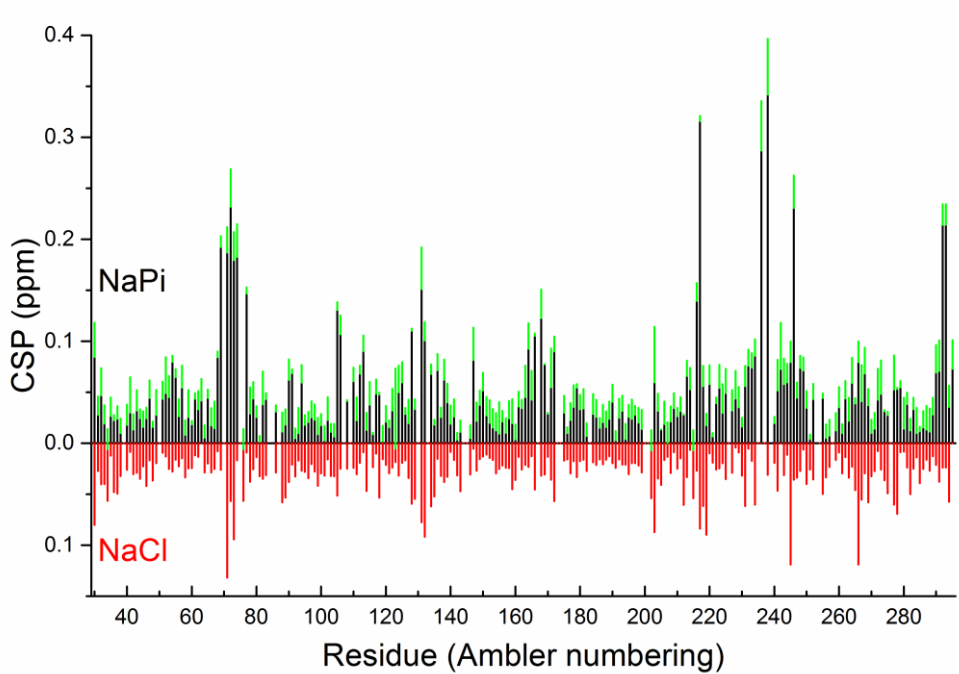
Figure S2.11. Absolute amide CSP upon titration from 0 – 250 mM with sodium phosphate (NaPi) or chloride (NaCl). Green error bars represent standard deviation over duplicate measurements.
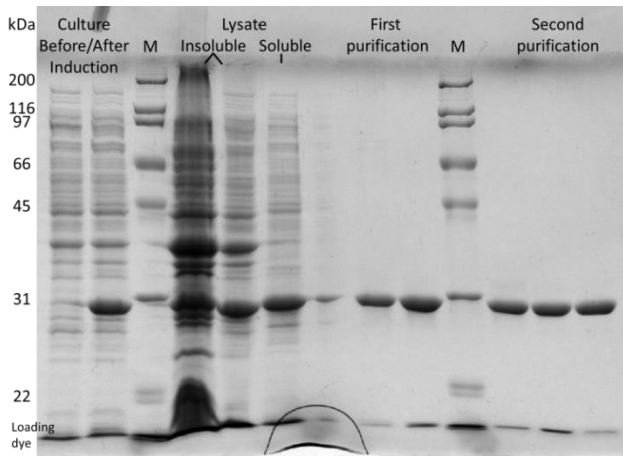
Figure S2.12. SDS-PAGE illustrating the production and purification process of BlaC (29 kDa). Minor impurities present after the first (Nickel column) purification are no longer visible after the second (gel filtration column) purification. This gel shows a representative protein batch. 'M' indicates a protein ladder, with band sizes shown on the left.

Octave script for simulation of inhibition curves

```
#! /usr/bin/octave -qf
# S(1) + E(2) k2<Ki>k1 SE(3) >k3 PSE(4) >k4 PS(5) + E(2)
# I(6) + E(2) k6<K2i>k5 IE(7) >k7 PIE(8) >k8 PI(9) + E(2)

# Load data and adjust
delay = 15;#deadtime
ext = 0.0173;          #extinction coeff of product in uM-1cm-1
data = load ("WE_BlaC_CLA_Phosphate_inhibition_data.txt");
time = data(:,1)-delay;
#abs = data(:,2:end)/ext; #convert abs to conc in uM
abs = data(:,2:end); #data already in uM
conc = load ("WE_BlaC_CLA_Phos_CLAconcen.txt"); #conc of clavulanate in each exp
m1 = rows(abs);
m2 = abs(1,:);

for i = 1:m1
 abs(i,:) = abs(i,:)-m2;
endfor

num1 = numel(conc);
num2 = numel(time);
res = zeros(num2,num1);
sq = zeros(num1,2);
sq(:,1)=conc';

for i = 1:num1
#for i = 1:1

con = conc(i);

# Define rates and differential equations
function xdot = f (x,t)
  Ki = 220;
  k1 = 1.05;
  k2 = Ki*k1;
  k3 = 2500;
  k4 = 103;
  K2i = 20;
  k5 = 1;
  k6 = K2i*k5;
  k7 = 0.045;
  k8 = 0.0018;
  xdot = zeros (9,1);
  xdot(1) = -k1*x(1)*x(2)+k2*x(3);
  xdot(2) = -k1*x(1)*x(2)+k2*x(3)+k4*x(4)-k5*x(6)*x(2)+k6*x(7)+ k8*x(8);
  xdot(3) = k1*x(1)*x(2)-(k2+k3)*x(3);
  xdot(4) = k3*x(3)-k4*x(4);
  xdot(5) = k4*x(4);
  xdot(6) = -k5*x(6)*x(2)+k6*x(7);
  xdot(7) = k5*x(6)*x(2)-(k6+k7)*x(7);
  xdot(8) = k7*x(7)-k8*x(8);
  xdot(9) = k8*x(8);

endfunction;
x0 = [125; 0.002; 0; 0; 0; con; 0; 0; 0];
#t = logspace(-3,8,10000);        #adjust to see entire range
```

```
y = lsode ("f", x0, time);
res(:,i) = y(:,5);
sq(i,2) = sum((abs(:,i)-res(:,i)).^2);

endfor

sqsum = sum(sq(:,2));
sqsum

# Plot the results

## Log plot of all concentrations
#plot (log10(t),log10(y));
#limits = axis([-3,8,-4,2]);
#xlabel ("log(10) time (s)");
#ylabel ("log(10) concentration (uM)");
#legend ("S", "E", "SE", "PSE", "PS", "I", "IE", "PIE", "PI", "location", "west");

#pause();

# Normal plot of data and predicted product curve
figure('Position',[100,350,1000,850]);
plot (time, abs, "-k", time, res,"-r");
limits = axis([1, 900, 0.1, 90]);
xlabel ("time (s)");
ylabel ("concentration (uM)");

print -djpg WE_BlaC_CLA_Phosphate_inhibition_data.jpg;
#save simul02.txt sqsum sq
pause();
```

Chapter 3

β-lactamase of *Mycobacterium tuberculosis* shows dynamics in the active site that increase upon inhibitor binding

Abstract

Mycobacterium tuberculosis β-lactamase BlaC is a broad-spectrum β-lactamase that is able to convert various β-lactam antibiotics. Enzymes with low specificity are expected to exhibit active site flexibility, which could result in protein dynamics. We studied the dynamic behaviour of BlaC in solution using NMR spectroscopy. ^{15}N relaxation experiments show that BlaC in the resting state is mostly rigid on the pico- to nanosecond time scale. Saturation transfer experiments indicate that also on the high millisecond time scale BlaC is not dynamic. Using relaxation dispersion experiments at two magnetic fields, clear evidence was obtained for dynamics in low millisecond range, with an exchange rate of about 860 s^{-1}. The dynamic amide groups are localized in the active site. Upon formation of an adduct with the inhibitor clavulanic acid, extensive line broadening and duplication of NMR signals occurs, indicative of at least one additional, slower exchange process ($k_{ex} < 100$ s^{-1}), while also loss of pico- to nanosecond time scale rigidity is observed for some amides in the α-domain. Possible sources of the observed dynamics, such as motions in the omega loop and rearrangements of active site residues and hydrogen bonds, are discussed.

Introduction

A central question in chemical biology is how enzymes can have broad specificity. Enzymatic catalysis depends on efficient binding of the substrate to the enzyme and on the precise positioning of active site residues to lower the energy of a transition state. Substrates that are structurally diverse, however, have different transition states and may thus require different active site conformations to stabilize their transition states.[76–78,81,83,144–147] This implies a trade-off between active site rigidity for minimal entropic loss upon substrate binding and flexibility for adaptation to various substrates. However, substrate binding typically occurs on the millisecond time scale, whereas bond cleavage and formation events occur many orders of magnitude faster.[148] Protein motions can

likewise occur on a broad range of time scales. It can be hypothesized that enzymes that combine high catalytic efficiency with broad specificity do so by combining high rigidity on short time scales with flexibility on longer time scales. Dynamics studies on Ambler class A β-lactamases TEM-1 and PSE-4 suggest that this is true for this protein class, as is reviewed in Chapter 1.

Studies regarding the dynamics of β-lactamase / ligand complexes, however, have been scarce. Recently, the cleavage of ceftriaxone by the extended spectrum class A β-lactamase BlaC was followed from 30 ms to 2 s in near atomic detail through the acquisition of four crystallographic snapshots by a novel method called Mix and Inject Serial Crystallography.[149] The snapshots give precise structural information about the processes involved in catalysis, but the dynamic information they provide is limited to the time scale of acquisition. NMR dynamics experiments could potentially provide much more insight into the dynamic behaviour of such complexes, but as such experiments tend to take up to several days, monitoring the normal catalysis of substrates this way is not feasible. However, β-lactamases can be inhibited. Inhibition of β-lactamases has been an important clinical approach for decades and is, moreover, gaining in relevance with the increased prevalence of antibiotic resistance. In Chapter 2, the time scale of interaction between BlaC (Figure 1.3) and the inhibitor clavulanic acid was characterised in different buffers.[28] The high stability that was identified for the complex in MES buffer opens up a window for NMR dynamics measurements.

Here, we present the first NMR measurements of dynamics in BlaC and the first characterization of β-lactamase / inhibitor complex dynamics in general. We show that the dynamic behaviour of free BlaC in solution is very similar to that of other class A β-lactamases and that the rate of the active site exchange process is *ca.* 860 s^{-1} at 298 K. We also show that the high rigidity, which is a hallmark of β-lactamases, is locally lost upon inhibitor binding. Furthermore, upon binding, the effects of chemical exchange in the active site become more extensive, clearly showing that inhibitor binding changes the energy landscape of the enzyme significantly.

Results

Resting state BlaC

The backbone amide assignment of resting state BlaC without tag was derived from the previously published assignment of the tagged protein[28] via comparison with an HNCa spectrum. In this way, 98% of the BlaC backbone H–N moieties were assigned to a resonance peak in the corresponding ^{1}H, ^{15}N transverse relaxation optimized heteronuclear single quantum coherence (TROSY-HSQC)[150] spectrum. The spectra are included in Figure S3.1, assignments can be accessed under Biological Magnetic

Resonance Bank (BMRB) ID 27888. As with the tagged protein, the four residues at hydrogen-bonding distance from the active site phosphate were the only nonproline, nonterminal residues for which backbone resonances could not be identified in the spectra. The four missing resonances, as well as the lower peak intensities of the surrounding amides (Figure 3.1), suggest that an intermediate-to-fast exchange process may be present in the active site.
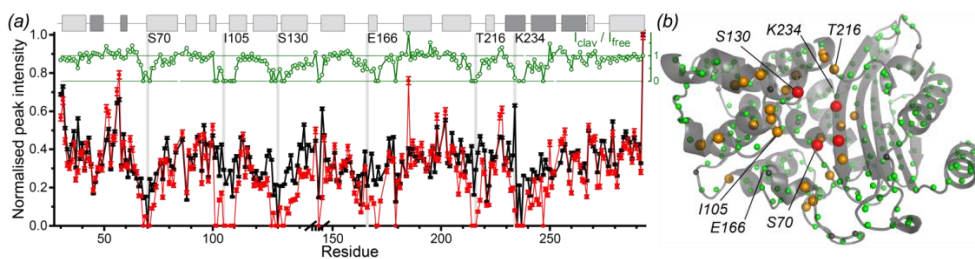

Figure 3.1. *(a) Relative peak intensities of assigned backbone amides in a ^{1}H,^{15}N TROSY spectrum, for resting state BlaC (black), BlaC bound to clavulanic acid (red) and the ratio between the two (green inset).* The resonance of the C-terminal amide was used for normalization. The break on the horizontal axis represents the insertion of a G-G-G-T-loop, relative to Ambler numbering. Several active site residues are indicated with grey bars. Secondary structure is indicated above the graph, light and dark grey boxes represent α-helices and β-strands, respectively. Error bars represent the spectral noise. *(b)* Visualisation of amide locations on BlaC crystal structure with PDB entry code 5NJ2. Non-proline backbone amides for which no resonance was found are indicated with red spheres. Amides for which the resonance was lost upon clavulanic acid binding are indicated with orange spheres. Amides for which a resonance could be assigned for resting state as well as bound BlaC are indicated with green spheres. Proline nitrogen atoms are indicated with grey spheres. Sphere sizes were varied between groups for emphasis.

To characterise the dynamics processes, the ^{15}N longitudinal relaxation time (T_1), ^{15}N transverse relaxation time (T_2) and the ^{15}N-{^{1}H} Nuclear Overhauser Effect (*NOE*) of the BlaC backbone amides were measured at two magnetic fields, 14 T and 20 T (Figure 3.2 and Figure 3.3, BMRB ID 27888). The obtained *NOE* ratios are high, close to and in some cases higher than the theoretical maximum, assuming an HN bond length of 1.02 Å and a chemical shift anisotropy of -160 ppm. This may be due to the 4 s relaxation time in those experiments, which was chosen based on the work of Renner *et al.*[151] and trial experiments with the model protein azurin, but may be insufficient for BlaC, as it is significantly larger.[152–154] Later experiments with ^{1}H saturation times of 6 and 10 seconds indicate that the *NOE* ratios may have been overestimated by as much as 0.025 on average. Nevertheless, the obtained *NOE* ratios show lower values for loop and surface regions of the protein and were used in further analysis. The influence of overestimated *NOE* on the resulting order parameters S^2 should be marginal, but the internal correlation times τ_e will be affected heavily and are not reported here.[155] Lipari-Szabo model-free analysis of the two-field T_1, T_2 and *NOE* data was performed using an anisotropic diffusion

tensor, yielding an average rotational correlation time of 13.9 ± 0.7 ns. This is in agreement with an estimate using HydroNMR[156] and crystal structure 5NJ2[28] (14.5 ns). Fitting of the spectral densities resulted in an average order parameter over 0.9 and yielded very few dynamic regions, confirming that BlaC is rigid on the short time scales (Figure 3.4). Most amides were best fitted with anisotropic models 1-4. Only for Val80, model 5, including an extra local order parameter S_f^2 for very fast motion, was used to fit the data (BMRB ID 27888). The resulting order parameters are S_f^2 = 0.79 ± 0.03 and S^2 = 0.57 ± 0.02, the latter of which is the lowest order parameter in the protein. The other regions that exhibit some flexibility correspond with elements that are expected to be flexible based on the crystal structure, such as the loop between β-strands 1 and 2 and that between α-helices 7 and 8.
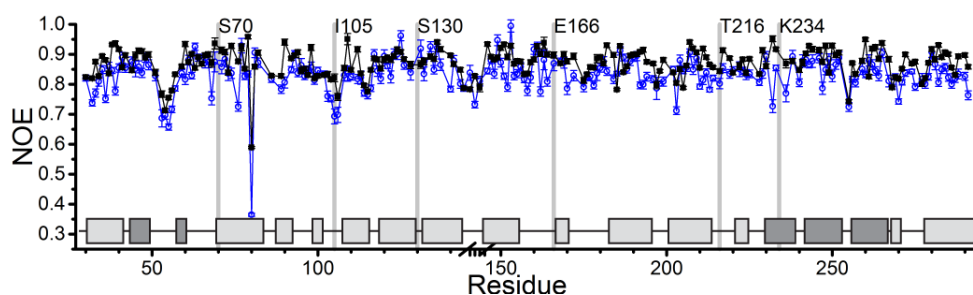

Figure 3.2. ^{15}N-{^{1}H} *NOE* **of BlaC backbone amides, as measured at 20 T (black) and 14 T (blue).** The break on the horizontal axis represents the insertion of a G-G-G-T-loop, relative to Ambler numbering. Error bars represent two times the standard deviations based on error propagation from the spectral noise. Several active site residues are indicated with grey bars. Secondary structure is indicated above the x-axis, light and dark grey boxes represent α-helices and β-strands, respectively. Values can also be accessed under BMRB ID 27888.

3
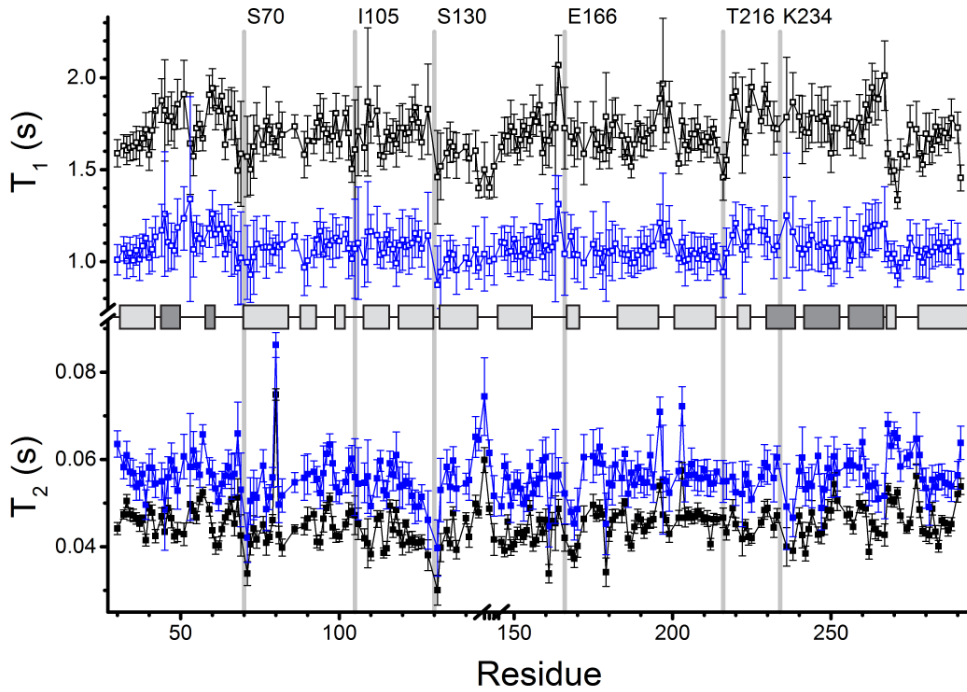

Figure 3.3. T_1 **(open symbols) and** T_2 **(closed symbols) relaxation times of resting state BlaC backbone amides, at 20 T (black) and 14 T (blue).** The break on the horizontal axis represents the insertion of a G-G-G-T-loop, relative to Ambler numbering. Several active site residues are indicated with grey bars. Secondary structure is indicated over the y-axis break, light and dark grey boxes represent α-helices and β-strands, respectively. Error bars represent the 95% confidence interval of the fit. Values can also be accessed under BMRB ID 27888.
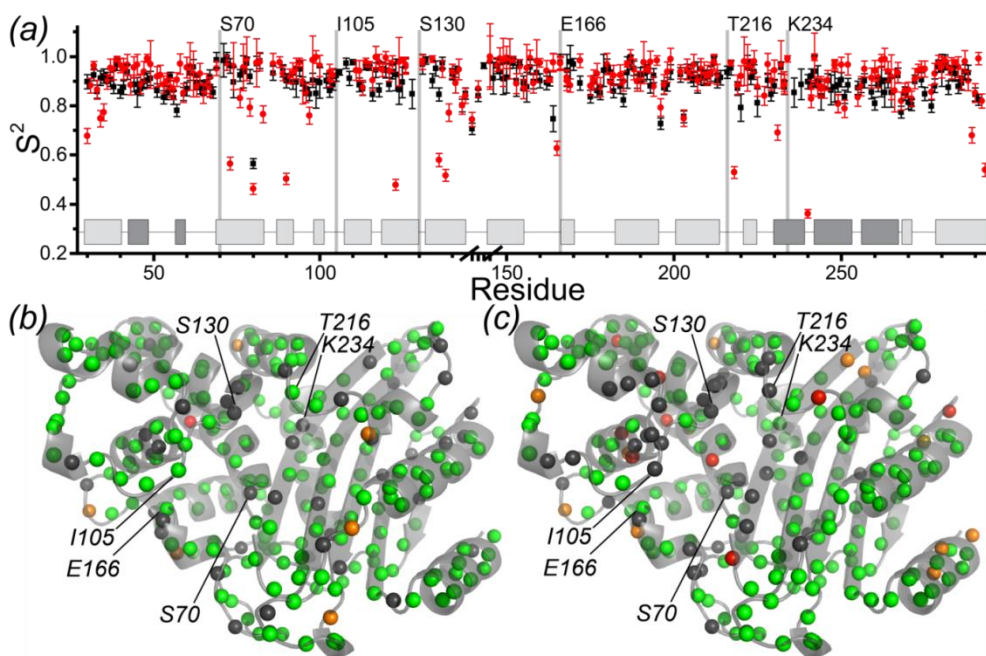
Figure 3.4. Backbone amide order parameter S^2. (a) S^2 values of BlaC resting state (black) and bound to clavulanic acid (red). Order parameters for resting state BlaC were obtained from per-residue fit with the best fitting anisotropic Lipari-Szabo model-free model to T_1, T_2 and NOE data from two magnetic fields. Order parameters for inhibitor-bound BlaC were obtained from similar fits to data from only one magnetic field and should therefore be interpreted as indicative. Error bars indicate the standard error of the fit. Several active site residues are indicated with grey bars. Secondary structure is indicated above the x-axis, light and dark grey boxes represent α-helices and β-strands, respectively. Values can also be accessed under BMRB IDs 27888 (free state) and 27890 (bound state). Low order parameters are indicated on the structure for BlaC in resting state *(b)* and bound to clavulanic acid *(c)*. Backbone amides with an order parameter $S^2 > 0.8$ are indicated as green spheres, those with $0.6 < S^2 < 0.8$ as orange spheres, those with $S^2 < 0.6$ as red spheres and those for which no S^2 could be determined with grey spheres.

Several residues could not be modelled without the inclusion of a chemical exchange parameter (BMRB ID 27888, residues for which Models 3 or 4 were used in the fit), so the possibility of exchange on the millisecond time scale was examined using CPMG relaxation dispersion measurements at 14 T and 20 T. Dispersion of relaxation over the pulse frequency, indicating millisecond chemical exchange, was observed to centre clearly around the active site (Figure 3.5, spheres in red and orange).
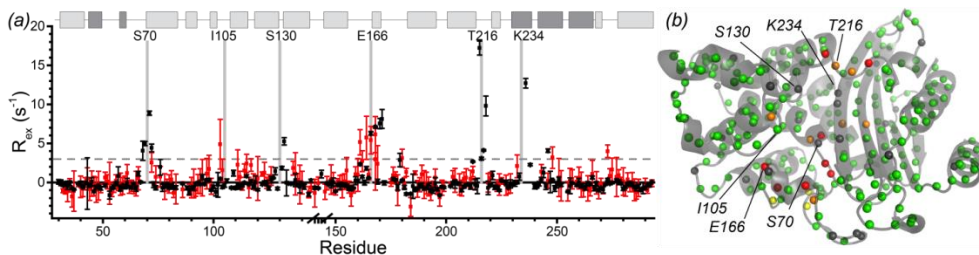
Figure 3.5. *(a)* **Contribution of chemical exchange to the R_2 relaxation of backbone ^{15}N resonances in BlaC resting state (black) and bound to clavulanic acid (red), as measured by CPMG relaxation dispersion analysis.** R_{ex} is defined as the $R_{2,eff}$ at v_{CPMG} = 25 s^{-1} minus that at 1000 s^{-1}. Error bars represent the 95% confidence interval based on three duplicate delays per experiment. The break on the horizontal axis represents the insertion of a G-G-G-T-loop, relative to Ambler numbering. Several active site residues are indicated with grey bars. Secondary structure is indicated above the graph; light and dark grey boxes represent α-helices and β-strands, respectively. Values can also be accessed under BMRB IDs 27888 (free state) and 27890 (bound state). *(b)* Visualization of resting state BlaC R_{ex} on structure 5NJ2.[28] Backbone amides whose relaxation dispersion profiles were used in the group fit are displayed as red spheres and others for which $R_{ex} \geq 3$ s^{-1} as orange spheres. Residues for which the relaxation dispersion profiles suggest possible exchange in the $10^3 - 10^4$ s^{-1} time scale are displayed as yellow spheres, others with $R_{ex} < 3$ s^{-1} as green spheres and those for which R_{ex} could not be determined as grey spheres.

Various types of relaxation dispersion curves were obtained. Examples are provided in Figure 3.6. Eight active site residues that showed similar dispersion profiles at both magnetic field strengths were used in a group fit (Figure 3.6 panels *(a) – (h)*, shown in Figure 3.5 as red spheres) yielding a chemical exchange rate of (8.6 ± 0.6) × 10^2 s^{-1}. The excited state population could not be determined with any accuracy (50 ± 50 %). A second profile shape was observed for residues Arg161, Ala164 and Asp179 (Figure 3.6, panel *(i)* and Figure S3.2, panels *(a) – (c)*). The contribution of this process to the affected relaxation rates was insufficient to determine the exchange rate adequately, but fits to the individual profiles suggest an exchange rate of *ca.* 10^3 – 10^4 s^{-1} (not shown). The similarity of the dispersion profiles and their co-localisation in the base of the Ω-loop (Figure 3.5, spheres in yellow) suggest that a second process may exist.
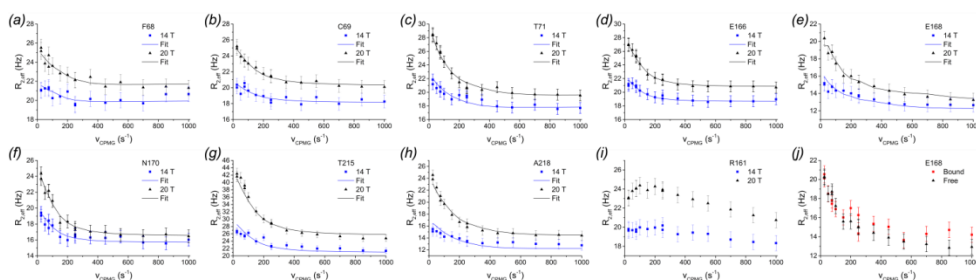
Figure 3.6. *(a)* – *(h)* Relaxation dispersion profiles that were used in a global, two-field fit yielding k_{ex} = (8.6 ± 0.6) × 10^2 s^{-1}. *(i)* Relaxation dispersion profile of Arg161, suggesting exchange on the 10^3 – 10^4 s^{-1} time scale. *(j)* Overlay of relaxation dispersion profiles of Glu168 in free form (black, same as panel *(e)*) and in clavulanic acid-bound form (red), as measured at 20 T. Error bars in all panels show the standard deviation of ±0.8 s^{-1} that was used to avoid over-fitting of ^{15}N offset-induced artefacts.

To investigate the possibility of even slower dynamic processes, chemical exchange saturation transfer (CEST) in resting state BlaC was also measured. Experiments with saturation fields of 25 Hz and 8 Hz and at temperatures of 298 K and 288 K all failed to reveal chemical exchange for any of the residues, suggesting that no significant dynamics in the CEST time scale of 20 - 200 s^{-1} are present. An example profile is provided in Figure S3.3.

Inhibitor-bound BlaC

The effect of BlaC inhibition on its dynamic behaviour was studied by performing NMR experiments on 0.38 mM BlaC with 100 mM clavulanic acid. Considering the ~1.2 h turnover time under these conditions,[28] this large excess of clavulanic acid allowed recording multidimensional NMR experiments on the BlaC/inhibitor complex. The ^{1}H-^{15}N TROSY-HSQC spectrum of backbone amides of BlaC bound to clavulanic acid was assigned by comparison to the spectra of resting state BlaC with additional help of an HNCa spectrum of a ^{15}N, ^{13}C labelled BlaC-clavulanate sample to confirm the assignments. The assignments are available at BMRB ID 27890.

Several peaks that are visible in the spectrum of resting state BlaC broaden beyond detection upon binding with clavulanic acid (Figure 3.1). These peaks all correspond to amides surrounding the binding site, indicating that the reaction with clavulanate induces enhanced chemical exchange broadening in the active site. Furthermore, at least 21 resonances were found to split into two or more distinct peaks. These peaks belong to amides around the active site and in the α-domain (Figure 3.7).
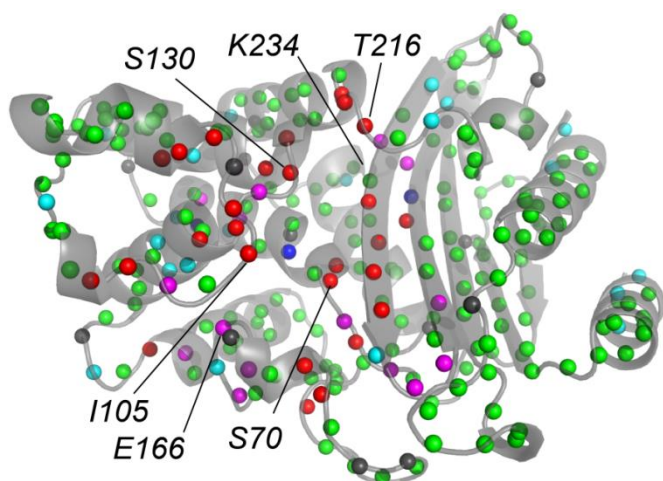
Figure 3.7. Dynamics of BlaC upon reaction with the inhibitor clavulanic acid. Backbone amides for which the resonance has broadened beyond detection are displayed in red, those for which multiple resonances could be assigned in magenta, those for which an order parameter $S^2 < 0.8$ was found in cyan, those for which the cyan and magenta conditions are both true in blue and those for which no severe dynamics were detected in green. Prolines amides are displayed in black.

The T_1, T_2 and *NOE* of clavulanate-bound BlaC were measured at 20 T (Figure S3.4 and Figure S3.5). A rotational correlation time τ_c of 16 ± 1 ns was obtained. This is significantly higher than the value for resting state BlaC, which may be caused by a change in viscosity upon the addition of 100 mM clavulanic acid to the buffer. This affects the absolute relaxation times of rigid amides, shifting the averages from 1.7 to 1.8 s (T_1) and from 45 to 40 ms (T_2). Interestingly, transverse relaxation rates were found to be significantly decreased for several residues in and near loops and terminal regions, as well as for six residues involved in the hydrophobic packing interface between helices 2 and 7 in the α subunit. Moreover, for these residues, the *NOE* is also lower than in the resting state BlaC (Figure S3.4). Lipari-Szabo model-free analysis indicates a severe decrease in rigidity in the afore-mentioned regions (Figure 3.4 and Figure 3.7). As these analyses were based on data at only one field strength and the BlaC diffusion tensor was found to be anisotropic, we would caution against over-interpreting the more detailed modelling results. Nevertheless, the data clearly indicate local loss of internal rigidity, particularly in loop regions and on the interface between helices 2 and 7.

CPMG relaxation dispersion measurements at 20 T were also performed on clavulanate-bound BlaC. However, most of the resonances that show exchange broadening in the resting state protein were broadened beyond detection in the clavulanate-bound spectra. Moreover, due to the splitting of peaks and the gradual appearance of molten globule-like background signal over time, accurate lineshape fitting of the resonances proved impossible in many cases. Residues Glu168 and Asp273 were found to have dispersion profiles with shapes similar to the active site exchange of the resting state protein (e.g.

Figure 3.6, panel *(j)*). Likewise, Arg161 showed dispersion similar to the putative faster exchange profiles (Figure S3.2, panel *(d)*). Slight elevations in the R_{ex} are observed around the loop containing Ile105, near the base of the Ω-loop and for residue Asp273, but overall the profile of exchange relaxation over all residues, keeping in mind the larger error and the missing data, looks rather similar to that of resting state BlaC (Figure 3.5). Thus, it seems that the resting state BlaC dynamics are still present upon formation of the clavulanic acid adduct and at the same time additional states are being populated, causing line broadening and peak splitting.

Discussion

We show that resting state BlaC is mostly rigid on the pico- to nanosecond time scale, similar to the behaviour of the other class A β-lactamases for which NMR dynamics studies have been performed, TEM-1[101–103] and PSE-4.[104] Only Val80 was found to exhibit significant fast motion, as modelled from the low *NOE* ratios and elevated T_2 relaxation times for its backbone amide. This is surprising, as this amide is located in the long α-helix 2 and the Val80 side chain does not face the outside of the protein but rather the interface between helices 2 and 7. The BlaC active site exhibits flexibility on the millisecond time scale, as observed by both CPMG relaxation dispersion studies and the broadening beyond detection of several important active site residues (Ser70, Ser130, Thr235 and Thr237). This behaviour is also similar to that of other class A β-lactamases,[101–110] and the localization of this chemical exchange in the active site suggests that the dynamics may play a role in catalysis. This can only be the case if the dynamics are as fast as or faster than the maximum catalytic turnover rate of the enzyme. This is the first time that the exchange rate of any serine β-lactamase active site was determined based on two-field CPMG relaxation dispersion experiments. The observed exchange rate of $(8.6 \pm 0.6) \times 10^2$ s^{-1} -obtained under the assumption of a two-state exchange model- is faster than the fastest k_{cat} that was reported for BlaC, 111 ± 4 s^{-1} for nitrocefin hydrolysis,[18] which implies that enzyme dynamics may be relevant for catalysis. On the basis of the Bloch-McConnell equations for chemical exchange, it can be shown that at an exchange rate of 860 s^{-1}, the population of the minor state must be sizeable (15 – 50 %) for the resonances of Ser70, Ser130, Thr235 and Thr237 to broaden beyond detection. The chemical shift difference between the major and minor state must be larger than 0.1 ppm for ^{1}H and/or 1 ppm for ^{15}N at 20 T. The link between these four residues is that in every BlaC crystal structure published to date, their respective sidechains each contribute to the hydrogen bonding with either the carboxyl group of a ligand or a phosphate or acetate ion from the solvent. However, upon titration with phosphate, the resonances do not appear (Chapter 2, [28]), meaning that the binding and dissociation of phosphate cannot explain the chemical exchange broadening of these peaks. The structural change causing this effect thus remains unclear.

 We also report the first dynamics study of a class A β-lactamase dynamics upon ligand binding. On the pico-nanosecond time scale the reaction with clavulanic acid leads to fast motions for various residues, notably including several that are involved in the hydrophobic packing interface between helices 2 and 7, similar to what was observed for Val80 for resting state BlaC. This result resembles the observation by Stivers *et al.* that several residues of 4-oxalocrotonate tautomerase show a decrease in the order parameter upon inhibitor binding.[157] The authors suggest that the increased flexibility of these residues serves as an entropic contribution to the overall free energy change upon binding, which may well be the same for BlaC. Structurally, an increase in fast dynamics of backbone amides generally indicates increased flexibility of the peptide bond. Many of the amides for which we observe this phenomenon are on the interface of helices 2 and 7. An increase of backbone flexibility implies reduced stability of the hydrophobic core in that region of the α-domain.

Inhibition of BlaC with clavulanic acid was accompanied by a broadening of some resonances and a doubling of others. All affected amides surround the active site. The doubling of amide resonances can indicate either slow chemical exchange occurring in a single species or the formation of various adducts, which has previously been observed with mass spectrometry (e.g. [18,28,38,158]). However, the relative intensities of assigned peak pairs are 42/58 ± 3 %, while in our hands only one major mass was observed, of +70 Da (Chapter 2, [28]). The minimum chemical shift differences between peak pairs of 0.3 and 0.027 ppm in the ^{15}N and ^{1}H dimensions, respectively, indicate that if there is exchange between the states, the exchange rate must be lower than 100 s^{-1}.

Such a low exchange rate cannot explain the broadening beyond detection of the neighbouring peaks in a two-state model. However, three peaks were assigned to Ala248 and multiple other peaks are observed in the 2D TROSY that were too weak in the 3D HNCa to be assigned confidently to a spin system. These observations indicate that the two-state model does not apply. It is possible that slow exchange between more than two states could explain the broadening beyond detection of many resonances around the active site. Alternatively, multiple motions could take place on different time scales in the same region of the protein. The relaxation dispersion profile of Glu168, which is similar in free and bound form (Figure 3.6, panel *(j)*), suggests the latter. This implies that the chemical exchange processes that we observe for BlaC in the bound state are introduced in addition to the existing active site exchange process in resting state. It is clear that the binding of clavulanic acid leads to a major increase in millisecond dynamics in and around the active site of BlaC. The motion affects the chemical environment of all the catalytic residues as well as residues in all the nearby regions.

The question arises how a clavulanic acid adduct of a mere 70 Da (5 heavy atoms) can have such a major impact on such a broad region of the protein. For related β-lactamases,

it has been suggested (e.g. [102,104,106]) that the process underlying the chemical exchange effects is movement of the tip of the omega-loop into and out of the active site. Such movement could facilitate the flow of solvent and substrate, and aid in positioning of the substrate in the active orientation. This is a plausible model and it may well be true for BlaC. If so, it seems likely that the introduction of an adduct in the active site could slow down the transition from open to closed state due to steric repulsion. Amides in all regions that are in contact with the tip of the Ω-loop, such as helix 7 and the loops containing Ser130 and Ile105, would be affected by such motion. This model thus fits well with our data. A loss of hydrogen bonds between the Ω-loop and the α-domain could even explain the increased fast motions that we observe for some of the residues there. However, the implied shift from the closed towards the open state upon inhibitor binding runs counter to recent observations by Sagar *et al.*.[159] They reported an unexpectedly large solvation radius for free BlaC in solution, while BlaC bound to clavulanic acid was found to have a solvation radius closer to that which is expected based on the crystal structure. The authors proposed that free BlaC in solution adopts an 'open' conformation, whereas inhibitor binding locks BlaC in the 'closed' conformation that is observed in all crystal structures so far. If resting state BlaC were indeed to adapt an open conformation in solution, it would likely exhibit a larger rotational correlation time than in the canonical closed conformation. We observed the opposite, an increase of the correlation time upon formation of the adduct. However, the experimental rotational correlation time may have been affected by a change in buffer viscosity upon addition of 100 mM clavulanic acid to form the adduct. Thus, the data presented here provide no evidence for an open state of free BlaC, but can also not falsify such a model.

To gain more insight into what the various states may structurally look like, we compared two crystal structures of BlaC in free form (PDB entry codes 5NJ2 and 5OYO[28]) with those of BlaC bound to clavulanic acid adduct (3CG5,[130] 6H2C and 6H2G[160]). Small differences between the individual structures, such as sub-Ångström rearrangements of the active site residues or the Ω-loop backbone, can be identified. Surprisingly, however, none of these differences are consistent within the two ensembles of free and clavulanate-bound BlaC. This lack of clustering is also reflected by the root mean square deviation of the alignment of the two free structures to each other (0.5 Å), which is not smaller than those for the three clavulanate-bound structures to free structure 5NJ2 (0.4, 0.2 and 0.8 Å, respectively). Recently, Olmos *et al.*[149] reported an XFEL study with snapshots at 30, 100, 500 and 2000 ms of the catalytic reaction of ceftriaxone hydrolysis by BlaC. The structures obtained during the reaction show almost no structural variation compared to that of BlaC in the resting state. The only active site residues of which the orientation varies between the structures are Lys73 and Ser130. Vandavasi *et al.* used neutron and X-ray crystallography to study the role of Lys73 in class A β-lactamase PenP and observed it to adopt two conformations upon ligand binding,[20] similar in orientation to the two

conformations observed for BlaC by Olmos *et al*. One of these conformations allows an extra water molecule to penetrate deep into the active site, between helix 2 (Lys73) and helix 7 (Met135, which is an alanine in BlaC). The occupancies of these states, 41 and 59 %, respectively, match the relative occupancies of the doubled peaks of 42 ± 3 % that we observe in our spectra. As mentioned before, if there is chemical exchange between the states in our spectra, the rate must be lower than 100 s^{-1}. Although this seems very slow for any movement as small as a sidechain reorientation, the fact that the two Ly73 states were distinguishable in crystal structures at 293 K as well as at 15 K does point towards the two states being highly stabilized relative to the transition states, implying that exchange should indeed be very slow. It therefore seems possible that the chemical exchange we observe upon clavulanic acid binding is related to the interconversion of Lys73 between different conformations and protonation states and is thus, as Olmos *et al.* argued, involved in proton transfer between Lys73 and Ser130.

In conclusion, we show that BlaC is highly rigid on the pico-nanosecond time scale, but exhibits flexibility on the millisecond time scale in and around the active site, with an exchange rate of *ca.* 860 s^{-1}. The dynamic behaviour of free BlaC is very similar the other class A β-lactamases for which dynamics studies were performed and therefore appears to be conserved amongst class A β-lactamases. The high rigidity minimises the entropic cost of binding, while flexibility allows adaptation to various substrates on the time scale of diffusion. We also show that upon binding to the inhibitor clavulanic acid, the prevalence of dynamics around the active site increases dramatically on both the millisecond and pico- / nanosecond time scales.

Materials And Methods

Materials
Pure BlaC without signal peptide and without purification tag (sequence detailed in Figure S2.3) was obtained as described previously.[28] The Ambler standard β-lactamase numbering scheme (Figure S2.3) is used throughout this thesis.[17] Clavulanic acid from manufacturer Matrix Scientific was used, concentrations were determined using the previously determined extinction coefficient at 256 nm of 20.0 (0.1) mM^{-1} cm^{-1}.[28]

Methods
Unless mentioned otherwise, all experiments were performed on samples containing 0.38 mM ^{15}N enriched BlaC in 94 mM MES/NaOH pH 6.4 and 6% D$_2$O, at 298 K. Measurements of BlaC bound to clavulanic acid were performed on samples obtained by mixing BlaC with clavulanic acid in the same buffer, ~1 h before the start of the acquisition to concentrations after mixing of 0.38 mM BlaC and 100 mM clavulanic acid, unless mentioned otherwise. NMR spectra were recorded on Bruker AVIII HD 850 MHz (20 T) or

Bruker AVIII 600 MHz (14 T) spectrometers equipped with a TCI cryoprobe or a TXI probe, respectively. HNCa spectra were measured on samples containing 0.7 mM $^{15}N^{13}C$ enriched BlaC (free) or 0.4 mM $^{15}N^{13}C$ enriched BlaC and 186 mM clavulanic acid, in the same buffer. These spectra were recorded using standard Bruker pulse program 'trhncaetgp3d', processed with Topspin 3.2 (Bruker Biospin, Leiderdorp) and analysed using CCPNmr Analysis.[143] NOE measurements were performed using standard Bruker pulse program 'hsqcnoef3gpsi' or to the sequence as detailed by Cavanagh et al.[89], with a ^1H saturation delay of 3 or 4 s. T_1 measurements were performed using standard Bruker pulse program 'hsqct1etf3gpsitc3d', with a recycle delay between experiments of 6 s and variable delays of 0.12, 0.17, 0.24 (2x), 0.33, 0.46, 0.65, 0.91, 1.28 (2x), 1.78 and 2.50 s. T_2 measurements were performed using standard Bruker pulse program 'hsqct2etf3gpsitc3d', with a recycle delay between experiments of 4 s and variable T_2-delays of ca. 0, 17, 34 (2x), 51, 68, 85, 102, 119 (2x), 136 and 153 ms. T_1 and T_2 data were processed with Topspin 3.2 and resulting peak heights were fitted to exponential decay curves using Dynamics Center 2.5 (Bruker BioSpin, Rheinstetten). NOE data were processed and analysed with the same software.

Lipari-Szabo analysis was performed with Dynamics Center 2.5. The rotational correlation time τ_c was calculated with Equation 3.1[161] and averaged over all residues for which the NOE > 0.75 and T_1 and T_2 were each within one standard deviation of their respective means. The experimental correlation time was compared with an estimate based on the crystal structure using HydroNMR[156] and subunit A of crystal structure 5NJ2, after deletion of the histidine tag and linker from the pdb file.

Equation 3.1.

$$\tau_c = \frac{1}{2 \times \omega_N} \times \sqrt{\frac{6 \times T_1}{T_2} - 7}$$

Least-squares fitting of the reduced spectral density function $J(\omega)$ to the relaxation parameters was performed with 1000 iterations with random starting parameters, using an NH bond length of 1.02 Å and an average chemical shift anisotropy of -160 ppm. To avoid overfitting of relaxation parameters with small errors, Lipari-Szabo analyses were performed with user-defined errors of 10 % (T_1) and 5 % (T_2 and NOE) of the respective values. Relaxation data from each residue were fitted with the five standard anisotropic model-free models.[161,162] In Model 1, the order parameter S^2 is fitted for each residue, while the correlation times τ_j are calculated from components and orientation of the diffusion tensor, which is a global parameter. In Model 2, a local correlation time τ_e for fast motion is additionally fitted individually for each residue. Model 3 is the same as Model 1, except that an R_{ex} term is added to the R_2 in the calculation of the reduced spectral densities. Likewise, Model 4 is the same as Model 2 with the addition of an R_{ex} term. In Model 5, an extra modelling parameter S_f^2 is included for very fast local motion. The best

model was selected based on the lowest *AIC* value, which is the sum of the χ^2 of the fit and the number of fitted parameters $\times$ 2. The selected model for each residue is reported under BMRB IDs 27888 (free state) and 27890 (bound state).

CPMG relaxation dispersion measurements were performed on 0.38 – 1.0 mM ^{15}N BlaC using the TROSY CPMG pulse program as detailed by Vallurupalli *et al.*,[163] with 0, 1 (2x), 2, 3 (2x), 4, 6, 8, 10 (2x), 14, 18, 22, 28, 34 and 40 ^{15}N 180° pulses in 40 ms relaxation time, respectively. Data were processed with NMRPipe[164] and resulting resonances were fitted to a glore lineshape using FuDa.[165] Effective transverse relaxation rates $R_{2,eff}$ were calculated from the fitted peak heights using $R_{2,eff}(v_{CPMG}) = -ln(\ I(v_{CPMG})\ /\ I_0\ )\ /\ T_{ex}$. In the relaxation dispersion data of BlaC bound to clavulanic acid, a few profiles showed ^{15}N-offset dependent variations that were much bigger than the experimental noise (examples in Figure S3.2, panels *(e)* and *(f)*). This variation is likely due to technical imperfections, so these data points were excluded from Figure 3.5 and BMRB ID 27890. An exclusion cut-off of 10 s^{-1} total increase in $R_{2,eff}$ between subsequent pulse frequencies was used. Figure S3.6 shows the complete dataset, including the points that were excluded from Figure 3.5, BMRB ID 27890 and further analysis. The chemical exchange rate and excited state population of the resting state were determined with a two-field grouped fit with the software CATIA,[97] using a minimum $R_{2,eff}$ standard deviation of 0.8 s^{-1} to avoid over-fitting of small ^{15}N offset-induced artefacts.

Chemical Exchange Saturation Transfer (CEST) measurements were performed on 0.38 – 1.0 mM ^{15}N BlaC using the standard Bruker 'hsqc_cest_etf3gpsitc3d' pulse program, with 2.5 s recycle delay and 0.8 s B$_1$ irradiation at frequencies in the ^{15}N range 100.5:0.5:130 ppm.

Figures containing the protein structure were created using the PyMOL Molecular Graphics System, Version 2.2 Schrödinger, LLC.
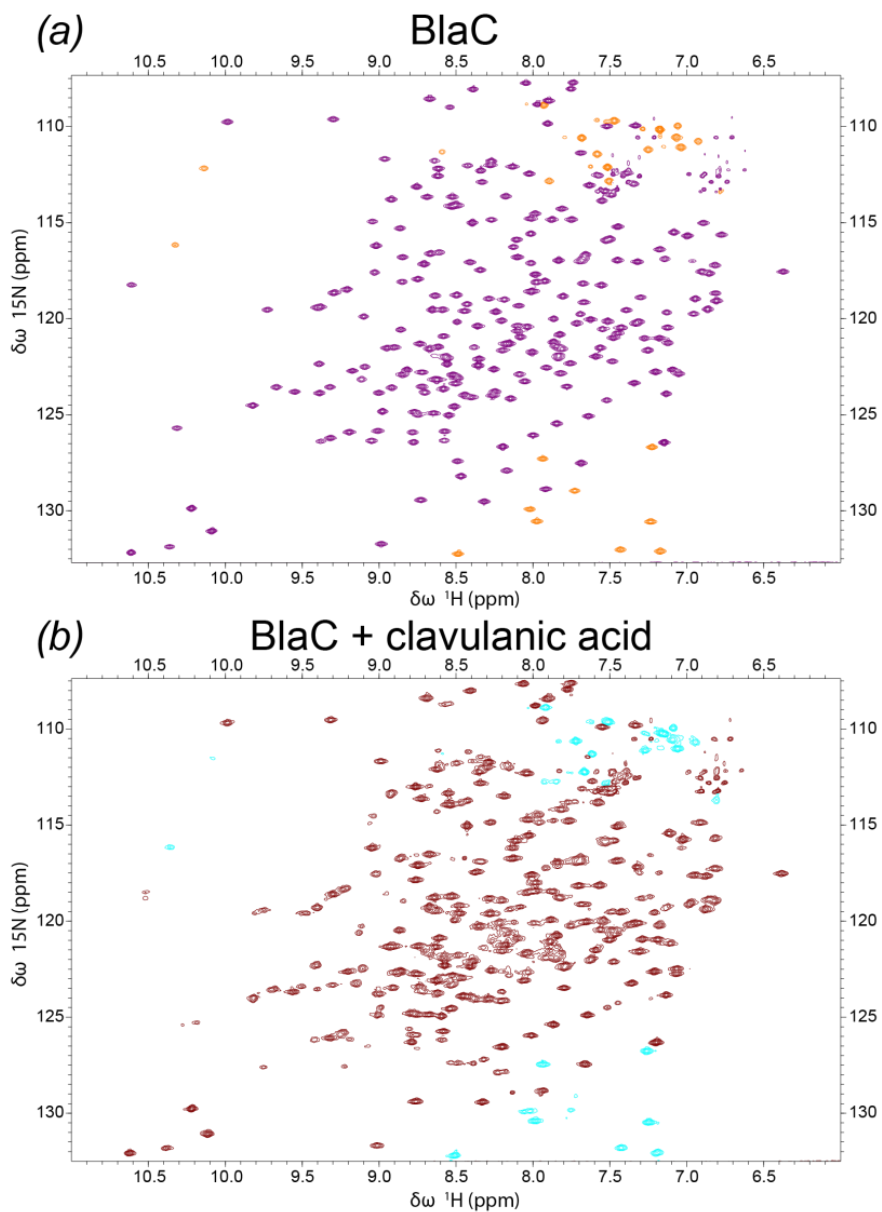
Supplementary Figures

Figure S3.1. TROSY-HSQC spectra of BlaC in free and bound state. In each spectrum, contour levels in the minority colour indicate folded peaks. Assignments can be accessed under Biological Magnetic Resonance Bank IDs 27888 (free state) and 27890 (bound state).
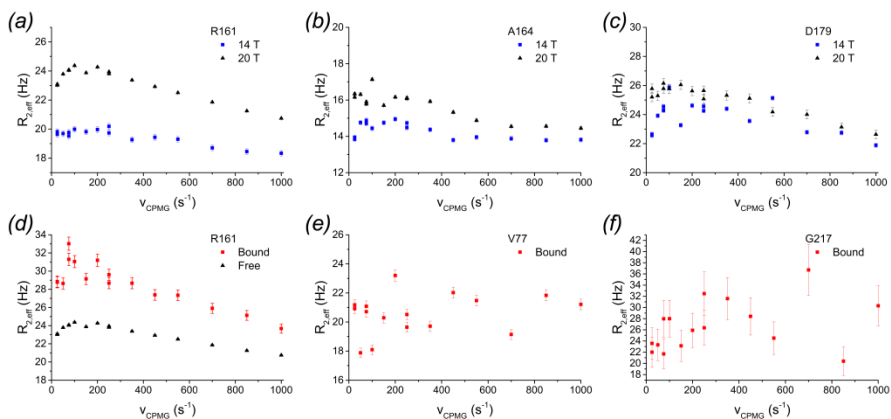
Figure S3.2. Example CPMG relaxation dispersion profiles. *(a) – (c)* Profiles suggesting exchange on the $10^3 - 10^4$ s^{-1} time scale. *(d)* Profile suggesting that exchange on the $10^3 - 10^4$ s^{-1} time scale may still be present after the binding of clavulanic acid. *(e), (f)* Examples of profiles that were excluded from Figure 3.5 and BMRB ID 27890 due to technical artefacts. Data in panels *(d) – (f)* were acquired at 20 T. Error bars in all panels represent the standard deviation based on three replicate pulse frequencies.
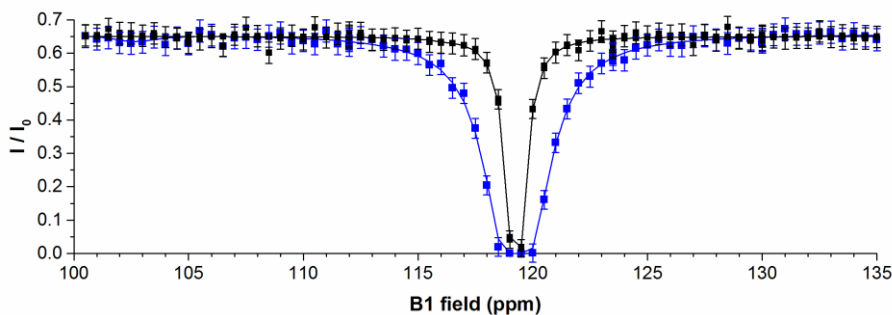

Figure S3.3. Example CEST curves for Glu166, as measured at 298 K with B_1 field strengths of 8 Hz (black) and 25 Hz (blue), respectively. Error bars represent the 95% confidence interval as derived from the spectral noise; lines are drawn to guide the eye. No secondary dips were observed.
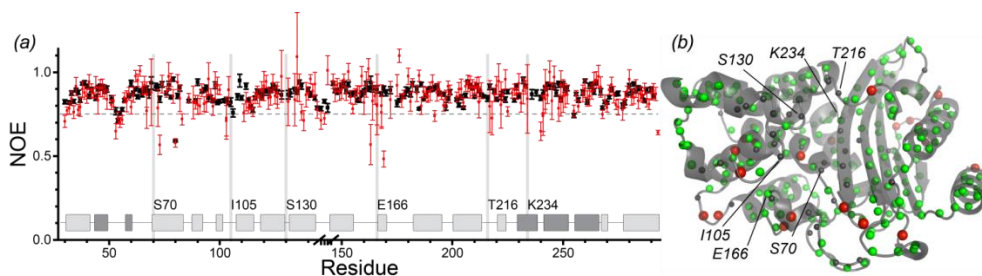
Figure S3.4. (a) ^{15}N-{^{1}H} NOE of backbone amides, as measured at 20 T for BlaC in resting state (black) and bound to clavulanic acid adduct (red). Several active site residues are indicated with grey bars. The break on the horizontal axis represents the insertion of a G-G-G-T-loop, relative to Ambler numbering. Secondary structure is indicated above the x axis, light and dark grey boxes represent α-helices and β-strands, respectively. Error bars represent the 95% confidence interval based on error propagation from the spectral noise. Values can also be accessed under BMRB IDs 27888 (free state) and 27890 (bound state). (b) Colour map of NOE upon binding of clavulanic acid. Backbone amides for which NOE < 0.75 are represented as red spheres, those with NOE ≥ 0.75 as green spheres and those for which NOE could not be determined as grey spheres. Sphere sizes were varied between groups for emphasis.
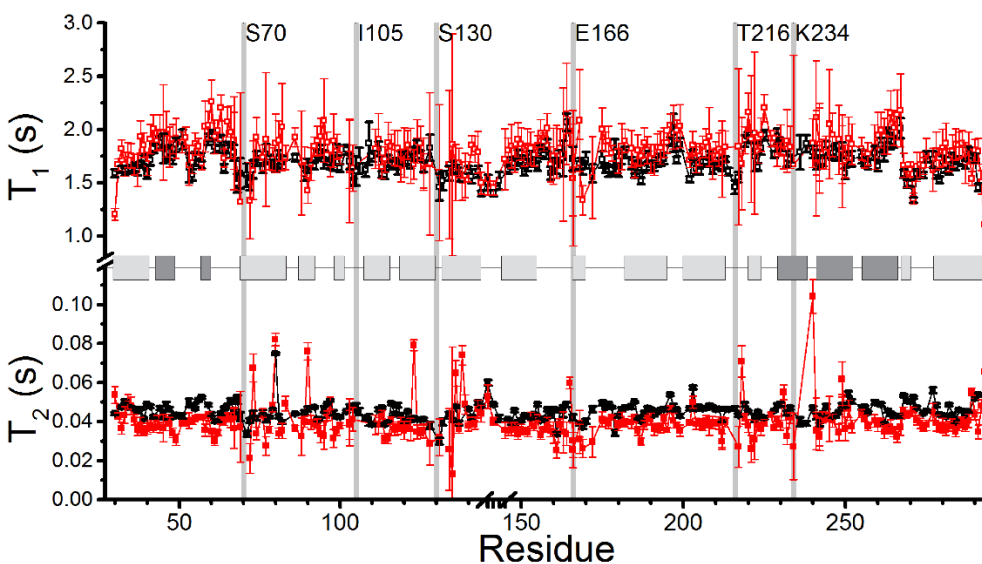

Figure S3.5. T_1 (open symbols) and T_2 (closed symbols) relaxation times of backbone amides of BlaC in resting state form (black) and bound to clavulanic acid adduct (red), measured at 20 T. Error bars show the standard error of the fit. Values can also be accessed under BMRB IDs 27888 (free state) and 27890 (bound state). Several active site residues are indicated with grey bars. The break on the horizontal axis represents the insertion of a G-G-G-T-loop, relative to Ambler numbering. Secondary structure is indicated over the y axis break, light and dark grey boxes represent α-helices and β-strands, respectively.
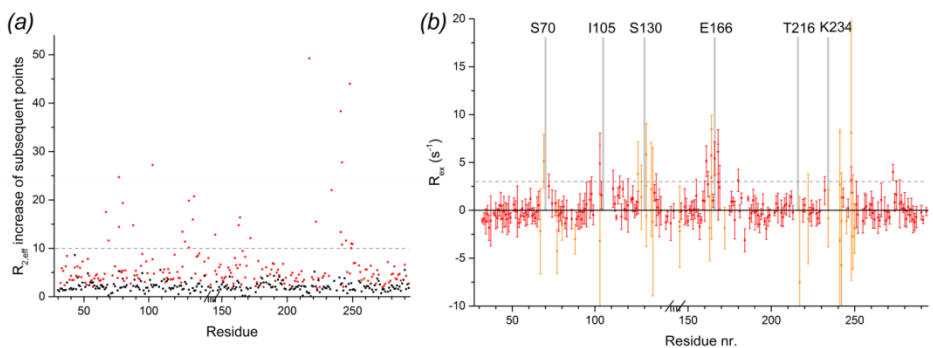
Figure S3.6. Exclusion of relaxation dispersion profiles with extremely large systematic deviations. *(a)* Plot of exclusion parameter on the protein sequence. No profiles from the resting state protein dataset (black) were excluded, 28 profiles from the clavulanic acid-bound protein dataset (red) were excluded. *(b)* Plot of resulting clavulanic acid-bound R_{ex} on the protein sequence, with data that were included in Figure 3.5 and BMRB ID 27890 in red and data that were excluded in orange. Several active site residues are indicated with grey bars for reference. Error bars represent the 95% confidence interval based on three duplicate delays per experiment.

Chapter 4

Role of protein dynamics in BlaC evolution towards clavulanic acid resistance

Abstract

The β-lactamase of *Mycobacterium tuberculosis*, BlaC, is susceptible to inhibition by clavulanic acid. The ability of this enzyme to escape inhibition through mutation was probed using error-prone PCR combined with functional screening in *Escherichia coli*. The mutation that was found to confer most inhibitor resistance, K234R, together with the mutation G132N that was found previously, were then characterised *in vitro* using NMR dynamics experiments. The G132N mutant exists in two, almost equally populated, conformations that exchange with a rate of *ca.* 70 s^{-1}. The conformational change is much more prominent than in the wild type protein and affects a broader region of the enzyme, around the active site. In the K234R mutant, on the other hand, the active site dynamics were significantly diminished with respect to the wild type. These results show that multiple evolutionary routes are available to reach the inhibitor resistant phenotype in BlaC and that active site dynamics on the millisecond time scale are not required for function.

Introduction

Chemical reactions are catalysed by enzymes through stabilization of the transition state, by arranging functional groups in the active site in precise orientations with respect to the substrate. Some enzymes can have broad substrate profiles, catalysing reactions with a variety of substrates. As different substrates will have different transition states, such enzymes must have some degree of flexibility in the active site. Furthermore, in some cases a single amino acid mutation can have a profound effect on the function, switching the specificity of an enzyme from one substrate to another. Conformational dynamics are required for protein evolution, as flexibility allows promiscuity and adaptation by single amino acid substitution.[83] In this chapter, such behaviour is studied in BlaC.

Evolutionary constraints of BlaC include factors such as efficient folding and export, stability at 37 °C and the ability to break down any β-lactams that its host *Mycobacterium*

tuberculosis encounters. Such environmental constraints may change over time, requiring the protein to adapt. With increasing clinical use of β-lactam / β-lactamase inhibitor combinations for the treatment of tuberculosis, the extent to which BlaC is able to adapt to evade inhibition becomes especially interesting. Questions that are addressed here include if, how and why BlaC can evolve, through mutation of one or few amino acids, to gain resistance to the clinically most used β-lactamase inhibitor, clavulanic acid. A method was developed and executed to quickly screen around a million mutants, each carrying a combination of a few semi-random mutations in the BlaC amino acid sequence, for increased clavulanic acid resistance. Mutants that confer such resistance were identified and confirmed through further testing. On the basis of these results and those published by others in the meantime, two mutants with a single amino acid mutation each were selected and isolated. NMR dynamics studies were performed to shed light on the relation between the acquired new functions and the dynamic behaviour of the enzyme.

G132N

One of the most conserved motifs in class A β-lactamase active sites is the serine-aspartate-asparagine (SDN) motif at Ambler positions 130 – 132. In BlaC, however, the asparagine at position 132 is replaced by a glycine. This substitution effectively removes a large side chain with two functional groups from the active site pocket and thus contributes to the phenomenon that BlaC has a wider active site than most of its relatives. This wide active site, in turn, has been suggested to be important for the broad substrate profile of BlaC. Specifically, substituents at the R^6 position of carbapenem could be accommodated by this substitution.[16]

Soroka *et al.* investigated the effect of G132N mutation in BlaC.[74,75] The impact of the substitution on the hydrolysis rate differs per substrate. In BlaC, G132N increases the rates of nitrocefin, imipenem and aztreonam hydrolysis, while decreasing rates of cefoxitin and ceftazidime hydrolysis. Interestingly, however, this single mutation was found to enable BlaC to hydrolyse clavulanic acid, while simultaneously increasing the efficiency of inhibition by another inhibitor, avibactam. The same adduct masses upon reaction with clavulanate were observed for BlaC G132N as for wild type (wt), so the increased turnover must represent either impaired tautomerisation or increased hydrolysis of the tautomers. Furthermore, in at least the class A β-lactamases KPC-2, CTX-M-1 and BlaMab, like in BlaC, the Gly in this position leads to a reduced affinity for avibactam, but also to reduced stability of acyl-enzyme complex with clavulanate.[37,74,75] On the other hand, inhibition by clavulanate has been reported for many SDN-containing enzymes,[15,166,167] so the effect of this substitution appears to be very context-specific. Multiple mycobacterial β-lactamases occur in both groups.

K234R

Another conserved motif in class A β-lactamase active sites is the KTG-motif at Ambler positions 234 – 236 in the hydroxyl-binding pocket. This motif occurs in almost all class A β-lactamases, including BlaC, but not in the carbenicillin-hydrolyzing enzymes, where it is replaced by an RTG-motif. The amine of Lys234 is nested in the wall of carboxylate binding pocket, where its charge plays an important role in the electrostatic binding of the substrate. Furthermore, mutational studies have shown that it is also involved in transition state stabilization.[168] The mutation K234R was found to increase resistance to clavulanic acid in class A β-lactamases such as SHV-1[169], SHV-72[68] and SHV-84,[73] in most cases without significantly decreasing catalytic activities against penicillins. Interestingly, in another class A β-lactamase, KPC-2, the K234R mutation did not show enhanced resistance against inhibition by clavulanic acid, but it did show enhanced resistance against inhibition by avibactam.[69] MD simulations[68] and X-ray crystallography[169] have shown that the K234R mutation in SHV β-lactamases causes a displacement of the Ser130 sidechain, moving it further away from the reactive Ser70. This may prevent the cross-linking between Ser70 and Ser130, which could explain the increased resistance of the enzyme to clavulanic acid. Egesborg *et al.* have found that this mutation also confers resistance to clavulanic acid in BlaC.[73] The resistance to inhibition by clavulanic acid was shown to increase further in BlaC by combining K234R with the S130G or R220S mutations, although these mutations significantly decrease the enzymatic activity.

Results

A library of BlaC mutants was generated, harbouring on average 5 single nucleotide replacements and ~0.08 deletions per mutant (Figure S4.1a). The mutations were found to be heavily biased towards A>G/T>C and A>T/T>A mutations and against G>C/C>G, G>T/C>A and A>C/T>G mutations, with only G>A/C>T mutations having an average frequency (Figure S4.1b). This is in line with expectations, based on observations by others (e.g. [123,124]). The efficiency of the transformation was identified to be the bottleneck in library generation. Using *E. coli* strain KA797 and the transformation protocol described by Inoue *et al.*,[170] efficiencies up to 0.5 million CFU per 200 μL cell volume were obtained. More details are provided in the Supplementary text. Several million mutants, mostly harbouring multiple mutations, were screened for their ability to provide *Escherichia coli* with increased resistance to ampicillin and clavulanic acid, relatively to wt BlaC. The most promising amino acid mutations based on their frequency of occurrence and the levels of resistance they conveyed upon *E. coli* were I105V, H184R, R213S, K234R and A262V. The corresponding single amino acid mutant proteins, with the addition of the G132N mutant which had been found to hydrolyse clavulanic acid by Soroka *et al.*,[74] were produced and purified. Their respective abilities to resist inhibition by clavulanic acid were characterised by measuring the onset of inhibition by 10 μM clavulanic acid (Figure 4.1). Part of this

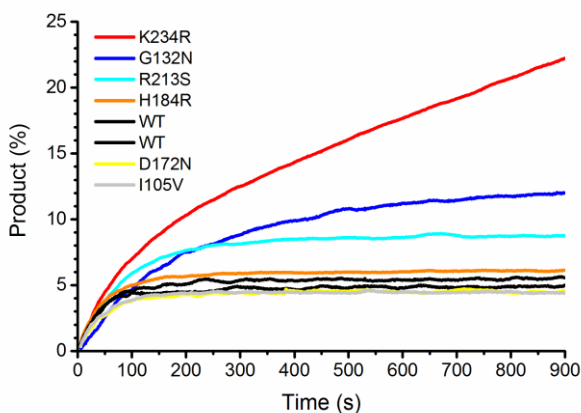work for the I105V and G132N mutants was performed in cooperation with Danny van Zanten.

Figure 4.1. Inhibition curves of nitrocefin hydrolysis by wt BlaC and single amino acid mutants of BlaC with 10 µM clavulanic acid. The protein concentration that was used varied between the different mutants, therefore the product concentration is displayed relative to the total product that is converted by the same concentration of the same BlaC variant in 900 seconds, when it is not inhibited. Mutations D172S, R213S and K234R were found together in one mutant, as were H184R and K234R. I105V was found in combination with D42G and R277C, which were not further tested as single mutants.

The effects of the I105V, H184R and A262V mutations on inhibition were not found to be significant. As these mutations were all found in combination with others, their effects may be epistatic or stability-related, but the more obvious explanation would be that the mutations are random, without any functional effect. This was not further investigated. The R213S mutant was found to require about four-fold more time than wt BlaC to reach full inhibition. This mutation may decrease the affinity of BlaC for clavulanate somewhat. The G132N and K234R mutations were found to convey more inhibition resistance, maintaining some level of activity even after prolonged exposure. As discussed before, both of these mutants had already been identified by others and have been well-characterised kinetically. However, nothing is known about the dynamic behaviour of these enzymes. To study this, the ^{1}H^{15}N spectra of BlaC mutants G132N and K234R were recorded and assigned through comparison of their HNCa spectra to that of wt BlaC. In the wt spectrum, peaks have been assigned to all non-proline backbone amides except Asp2 and four phosphate-binding residues in the active site.[28] The mutant proteins each exhibited well-dispersed spectra that show significant overlap with the wt spectrum, indicating that both share the same overall fold with wt BlaC (Figure S4.2).

In the spectrum of K234R BlaC, peaks were assigned to all the backbone amide groups that were assigned in wt BlaC, including Arg234. Also the resonance belonging to the backbone

amide of Thr235 could be assigned. This resonance is not detectable in the spectrum of wt BlaC (Figure S4.2, marked with *).

In the spectrum of G132N BlaC, many resonances could not be detected. The region for which peaks of backbone amides have broadened beyond detection was found to have extended from the four phosphate-binding residues in wt BlaC to include Glu166, the active site-covering loop ranging from Ser104 to Val108 and the loop between helices 6 and 7, containing Ser130 and the variant residue Asn132 (Figure 4.2). Surprisingly, this last stretch of undetectable amides extends all the way until Leu137, spanning half of helix 7 (Figure 1.3). Furthermore, the resonances of several surrounding residues were observed to have split between two positions. These observations indicate the presence of a chemical exchange process. The split peaks have a minimum distance of ~21 and ~24 Hz in the ^{1}H and ^{15}N dimensions, respectively, which means that the rate of exchange between the two states must be lower than *ca.* 100 s^{-1}. The relative peak intensities of the split peaks suggest populations of *ca.* 60 and 40 %. In the protein structure, the amides for which the resonances were broadened or split are centred around the G132N mutation and the rest of the active site (Figure 4.2).
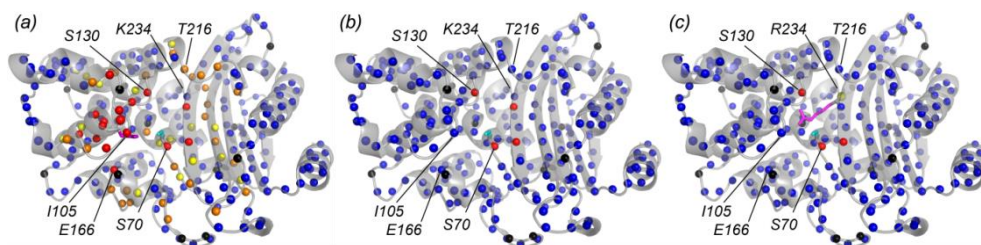

Figure 4.2. Residues for which the backbone amide resonances were lost, split or diminished in the spectra of *(a)* G132N, *(b)* wt and *(c)* K234R. Backbone amides are indicated as spheres. Red: no resonance could be assigned. Orange: two resonances assigned. Yellow: one resonance assigned, but peak intensity diminished below half of the wt relative peak intensity. Blue: one resonance assigned, normal peak intensity. Black: proline. The Ser70 side chain is indicated as a cyan stick, mutant side chains are indicated as magenta sticks, modelled into subunit A of the structure with PBD entry 5NJ2.[28]

The positions of the backbone amide resonances in the spectra of both mutants were compared with those of wt BlaC (Figure 4.3). Large and extensive chemical shift perturbations (CSP) were observed for both mutants, which we attribute to significant disturbances of the active site water network close to the mutation site, as well as in the extended hydrogen bonding network. No large perturbations were observed for any residues that are very far from the mutation site in the wt structure, further corroborating that the proteins are correctly folded.
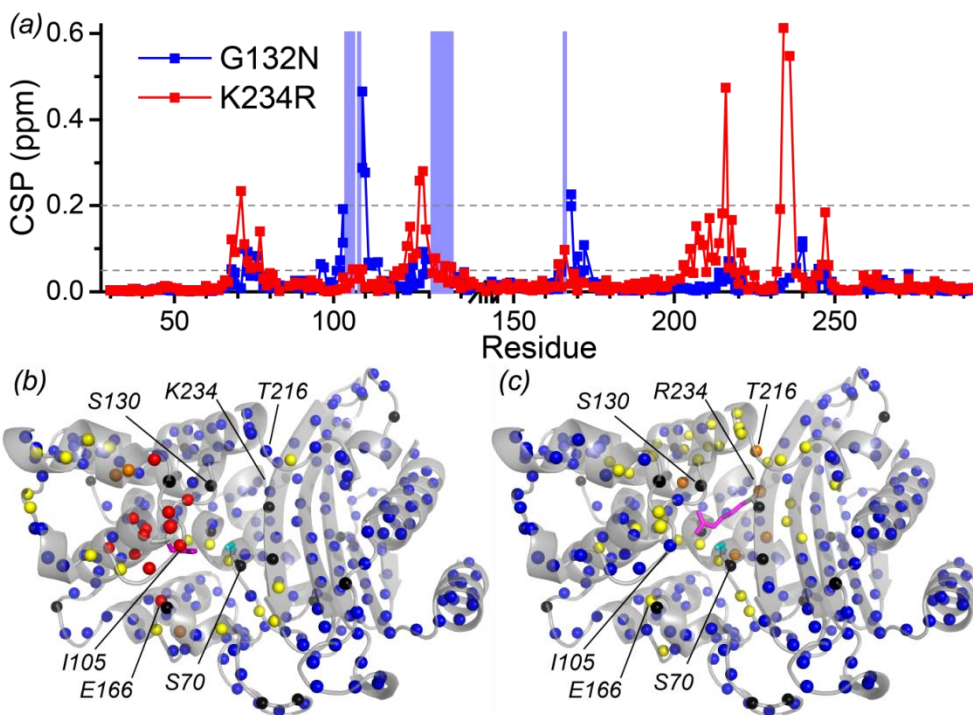
Figure 4.3. Chemical Shift Perturbation (CSP) of BlaC backbone amide resonances upon mutation. *(a)* Plot of average absolute CSP on the sequence [$|\frac{1}{2}\Delta\delta(^1H)| + |0.1*\Delta\delta(^{15}N)|$]. Blue background indicates residues that have broadened beyond detection in the G132N mutant. Grey dashed lines represent cut-off values for the colouring of amides in *(b)*. The break on the horizontal axis represents the insertion of a G-G-G-T-loop, relative to Ambler numbering. Error bars have been omitted for clarity, estimated 95% confidence interval is ± 0.03 ppm. *(b, c)* Plot of CSP for BlaC G132N *(b)* and BlaC K234R *(c)* on the structure. Orange: CSP > 0.2 ppm. Yellow: 0.2 ppm ≥ CSP > 0.05 ppm. Blue: CSP ≤ 0.05 ppm. Red: Peak broadened beyond detection in G132N but not in wt BlaC. Black: no data available. Side chains of the mutated residues are displayed in magenta stick representation. Structure: PBD entry 5NJ2, subunit A.

As the K234R mutation is very near to the phosphate binding site and appears to affect the dynamic behaviour of at least Thr235, which participates in phosphate binding, the phosphate affinity was measured with a titration. Surprisingly, a K_D of 20.1 ± 0.7 mM (Figure S4.3, error from fit of one titration) was found for BlaC K234R, which is close to the K_D of 27 ± 11 mM (error from duplicate titration) found for wt BlaC (Figure 2.5, [28]).

To probe the effect of these mutations on the pico- to nanosecond dynamics, the Nuclear Overhauser Effect (*NOE*) of the backbone amides was measured (Figure 4.4). The high *NOE*s indicate that the two mutants, like wt BlaC, are overall very rigid. The *NOE*s of most residues are very similar to wt, showing the expected reductions for flexible loops and high values in long β-sheets and α-helices. There are also residues that show increased or decreased rigidity. Notably, residue Ile247 in K234R displays a very low *NOE*. This amide is

situated on β-strand 4, directly adjacent to residue 234 on β-strand 3. In the wt structure, the Ile247 amide is hydrogen bonded to the carbonyl group of Lys234. The loss of rigidity that we observe may suggest that this hydrogen bond is lost upon mutation of Lys234 to Arg. However, the other amides on these two strands show *NOE*s that are similar to those in wt, indicating that the effect is very local. In G132N, fast dynamics are observed around Ser70, at least for one of the two forms. Val80, which displays increased flexibility in wt BlaC, is stabilised in G132N and even further in K234R, where it returns to a normal rigidity compared to the rest of the protein.
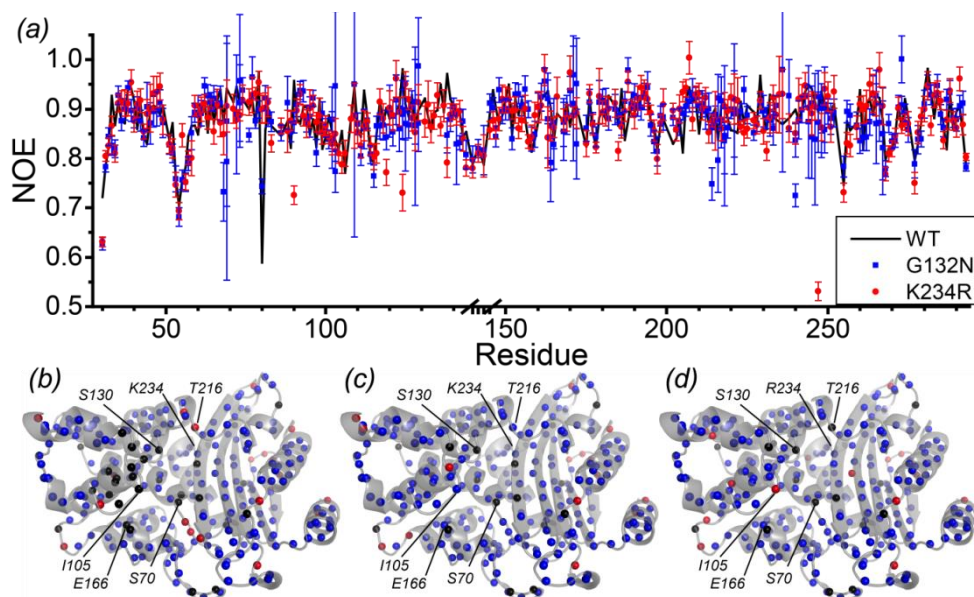

Figure 4.4. Nuclear Overhauser Effect (*NOE*) of mutant and wt backbone amides. *(a)* Plot of *NOE* for each residue. The break on the horizontal axis represents the insertion of a G-G-G-T-loop, relative to Ambler numbering. Error bars indicate the standard deviation based on the spectral noise. The wt BlaC *NOE* values are displayed as a line for reference, values and errors can be found in Figure 3.2 and under BMRB ID 27888. Mutant *NOE* values are also included under BMRB IDs 27889 (G132N) and 27891 (K234R). *(b-d)* Plots of *NOE* values on the BlaC structure, for G132N *(b)*, wt *(c)* and K234R BlaC *(d)*. Backbone amides with *NOE* < 0.8 are displayed in red, those with *NOE* ≥ 0.8 in blue and those for which no data are available in black. Structure: PDB entry 5NJ2, subunit A.

To probe the effect of the G132N and K234R mutations on the millisecond dynamics of BlaC, CPMG relaxation dispersion experiments were performed. In wt BlaC, significant relaxation dispersion was observed around the active site, indicating dynamics with an exchange rate of *ca.* 860 s^{-1} (Chapter 3 and Figure 4.5a, black). Surprisingly, this relaxation dispersion is completely absent in mutant K234R (Figure 4.5a, red). The opposite effect is observed in mutant G132N, which shows strikingly increased relaxation dispersion for many residues (Figure 4.5a, blue). Like the broadened and split peaks, the peaks that show

relaxation dispersion are also centred around the active site (Figure 4.5b). A few example CPMG profiles are provided in Figure 4.6 and more in Figure S4.4.
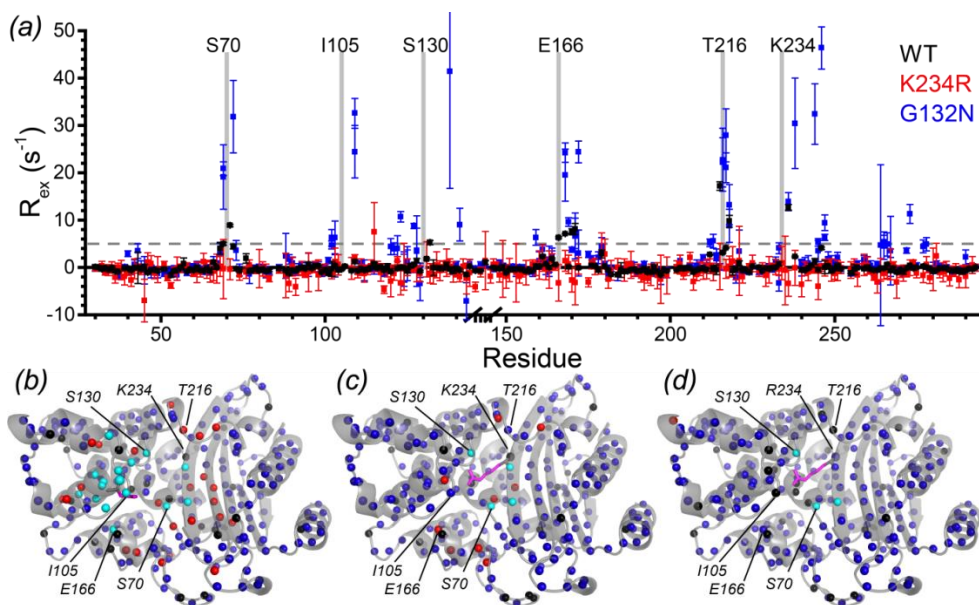
Figure 4.5. Chemical exchange effects observed for backbone ^{15}N resonances in BlaC, as measured by CPMG relaxation dispersion analysis. R_{ex} is defined as the $R_{2,eff}$ at v_{CPMG} = 25 s^{-1} minus that at 1000 s^{-1}. *(a)* Plot of R_{ex} vs. the residue number. The break on the horizontal axis represents the insertion of a G-G-G-T-loop, relative to Ambler numbering. Error bars represent the 95% confidence interval based on three duplicate delays per experiment. Values can also be accessed under BMRB IDs 27888 (wt), 27889 (G132N) and 27891 (K234R). *(b)-(d)* Colour map of R_{ex} on the structure, for G132N *(b)*, wt *(c)* and K234R BlaC *(d)*. Backbone amides with R_{ex} > 5 s^{-1} are displayed in red and those with R_{ex} ≤ 5 s^{-1} in green. Amides for which the resonance was broadened beyond detection are displayed in cyan. Amides for which no data was available for a different reason (e.g. proline or too much overlap) are displayed in black. Mutated residues are displayed as magenta sticks, modelled into subunit A of the structure with PBD entry 5NJ2.[28]
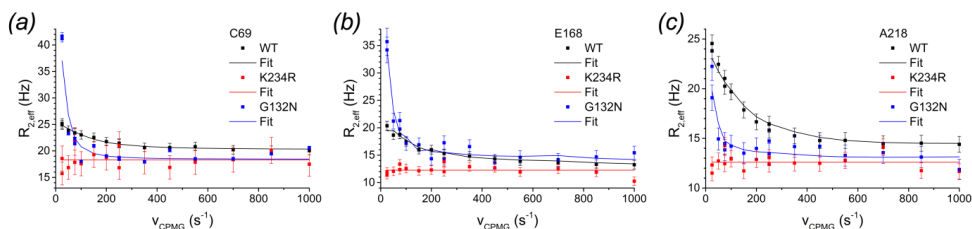

Figure 4.6. Example CPMG profiles from BlaC wt, G132N and K234R. The lines represent global fits using CATIA software for BlaC wt and G132N and individual fits to $R_{2,eff}$ = c for BlaC K234R. Error bars represent standard deviation based on three duplicate frequencies.

A global fit using CATIA software[97] of 36 G132N dispersion profiles (Figure S4.4) resulted in an estimate of the exchange rate of 70 ± 2 s^{-1}, and the state B population (p_B) of 48.99 ± 0.01 %. This fitting procedure also yields the absolute ^{15}N chemical shift difference, $|\Delta\Omega|$, between the resonance positions of the two states. For several residues, the fitted $|\Delta\Omega|$ is significantly larger than the coalescence point at an exchange rate of 70 s^{-1}, which is ~0.18 ppm at the experimental magnetic field strength of 20 T. This implies that these amides are predicted to experience slow-intermediate exchange. This, together with the extraordinarily high predicted p_B, means that the fit predicted that the second states of these peaks should be visible in the spectrum. As we did indeed observe doubled peaks, we were able to cross-check the fit by comparing the predicted $|\Delta\Omega|$ values with those that were measured in the spectrum assignment (Figure 4.7). The fitted and observed $|\Delta\Omega|$ values correlate well, though there appears to be a small bias, reflecting either an experimental underestimation of $|\Delta\Omega|$ due to peak picking artefacts of partly overlapping peaks, or an overestimation of the $|\Delta\Omega|$ by the fitting procedure. However, the results clearly suggest that the observed peak doubling reflects the same exchange process as observed with the RD experiments.
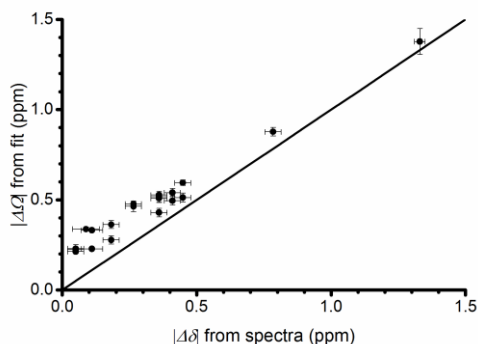

Figure 4.7. Correlation plot of the $|\Delta\Omega|$ derived from RD NMR versus the ^{15}N chemical shift differences observed in the HSQC-spectrum for the two BlaC G132N states. The diagonal line indicates y=x. Vertical and horizontal error bars represent standard deviation of the fit and the estimated error in the peak picking, respectively.

Chemical exchange with a rate of 70 s^{-1} should also be observable using the Chemical Exchange Saturation Transfer (CEST) method. We previously reported no measurable exchange in this regime for wt BlaC. CEST of the G132N mutant was measured, yielding direct observation of exchange between the resonances with the largest chemical shift differences, Gly238 and Asp246 (Figure S4.5). Unfortunately, the $|\Delta\Omega|$ values of the other exchanging resonances are too small to be observed clearly via CEST. No other CEST profiles indicated exchange. Nevertheless, it is clear that the doubled peaks in the G132N spectrum arise from two states of the protein that are in exchange.

The exchange rate and excited state population (p_B) of 70 s^{-1} and 49 %, respectively, were obtained from a global fit of as many similar relaxation dispersion profiles as possible, as is the usual practice. Usually, however, only state A is visible and can be measured directly. In the BlaC G132N spectrum, both states are visible and a mix of the two were used in the fit. Although this procedure does yield the most accurate estimate of the exchange rate, the estimate of the p_B can obviously not be trusted. Fortunately, the facile detection of the two states allows us to determine which peaks correspond to the same populations by simply acquiring TROSY-HSQC's at various temperatures. The relative intensities of ten non-overlapping peak pairs at five temperatures ranging from 279 to 298 K were used to determine that the true population of state B at 298 K is 40 ± 2 %. Furthermore, this analysis revealed that the major state at 298 K becomes the minor state at lower temperatures and thus has a higher energy level (Figure 4.8). The CATIA relaxation dispersion fit was repeated for states A and B separately, with p_b fixed at 0.4 and 0.6, respectively. This yielded exchange rates and $|\Delta\Omega|$ values that are very similar to those from the global fit (Figure S4.6).
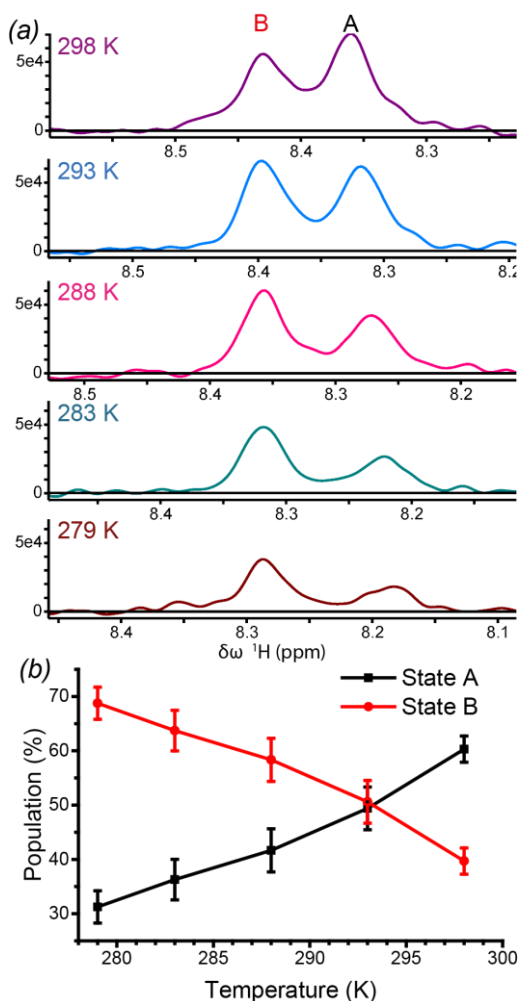
Figure 4.8. Temperature dependence of BlaC G132N state B population. *(a)* Example of a doubled peak, Ala164, at five temperatures. The $|\Delta\Omega|$ in the ^{15}N dimension is zero for this amide, as is the ^{15}N $\Delta\delta$ in the temperature titration, thus slices through this dimension yield the peak shapes and maxima for both states A and B. Note that peak maxima normally decrease with temperature as a result of sample viscosity. *(b)* Average and standard deviation of relative intensities of ten split backbone amide resonances in the five ^{1}H-^{15}N TROSY-HSQC spectra.

Discussion

Here we reported on the dynamics of two variants of BlaC that both increase resistance to inhibition by clavulanic acid. Curiously, the mutations have opposite effects on the dynamic behaviour in the millisecond time scale. K234R reduces the active site chemical exchange in the millisecond time scale, while G132N increases it. Neither mutation has large effects on the pico- to nanosecond time scale dynamics of BlaC.

G132N

We show that BlaC G132N exists in two almost equally populated states, exchanging with a rate of *ca.* 70 s^{-1}. This is observed through the splitting of backbone amide resonance peaks around the active site and the mutation, as well as through CEST and relaxation dispersion experiments. Additionally, the resonances of amides in a large region around the mutation have broadened beyond detection. However, it should be noted that several very broad peaks in the two-dimensional TROSY-HSQC spectra remain unassigned due to being undetectable in the three-dimensional HNCa spectrum. Generally, most of the active site resonances that are detectable have broadened significantly in the HNCa and thus barely reach the detection threshold. These observations, combined with the concentric localisation of the peak broadening, the peak splitting and the relaxation dispersion, suggest that all of these effects may arise from the same exchange process with a rate of 70 s^{-1} and a state B population of 40 % at 298 K.

The observed chemical exchange of BlaC G132N is significantly slower than the active site exchange process that was observed for the wt protein, *ca*. 860 s^{-1} (Chapter 3), and it is detected in a much broader region of the protein. The observations of broadened and split resonance peaks rather parallel those for wt BlaC bound to clavulanic acid. Upon inhibitor binding, resonances are also lost or split into multiple peaks, in a very similar region of the protein (compare Figure 4.2a, Figure 3.7). Chemical exchange between the split peaks in bound form, like in the G132N mutant, must be much slower than the exchange that wt BlaC displays in free form. However, although the protein region that is affected by peak splitting is very similar in the two cases, the relative positions in which the split peaks appear in the spectrum are not. Furthermore, in the G132N spectrum, resonances that split all show two states with consistent exchange and relative populations. This is not the case for inhibitor-bound BlaC, where for one of the amides, three resonance positions could be identified. Moreover, the large relaxation dispersion that we observe for G132N amides is absent in inhibitor-bound wt protein. Therefore, although the observations in the two datasets are reminiscent, it seems unlikely that they represent the same dynamic process.

To interpret the process, it is important to consider the effect of the G132N mutation. The Asn side chain introduces a relatively large extra moiety in the active site of BlaC. This requires spatial adaptation of other residues that occupy the same position, most notably Ser104. This residue in wt BlaC points inwards to take the space that is occupied by Asn132 in TEM-1 and SHV-1, where the residue at position 104 points outward (Figure 4.9). Intuitively, a minor dislocation of the loop that covers the active site like a lid appears to be the most accessible way to generate space for the Asn side chain. Indeed, in TEM-1, this loop is located a few Å further away from the active site (Figure 4.9).
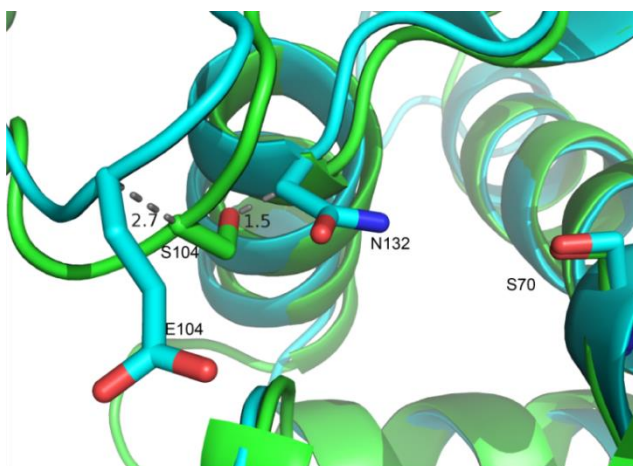
Figure 4.9. Alignment of BlaC (green) with TEM-1 (cyan). TEM-1 Asn132, Glu104 and BlaC Ser104 as well as both Ser70 residues are displayed in stick representation. Dashed grey lines indicate distances in Å. In BlaC, Ser104 would clash with an Asn residue at position 132. In TEM-1, residue 104 is displaced relative to Ser104 in BlaC. The distance between the C_α atoms is 2.7 Å.

A dislocation of the 'lid' loop would presumably affect the hydrogen bonds between the lid loop and residues 131-134 (Figure 4.10), in line with the NMR effects observed for these residues (Figure 4.3 and Figure 4.5). Unless displacement of the lid loop involves partial unfolding of helix 7, it does not explain, however, why the resonances of amides 135 – 137 have also broadened beyond detection. The reason for this may lie in an interaction between Asn132 and Glu166. A reorientation of the backbone at position 166 could drastically change the chemical environment of Asn136, which staples the omega loop to the α-domain via hydrogen bonds with the backbone carbonyl and amide of Glu166 (Figure 4.10). In fact, movement of the tip of the omega-loop into and out of the active site is the commonly held model for the active millisecond dynamics that are observed in several class A β-lactamases, including BlaC (Chapter 3).
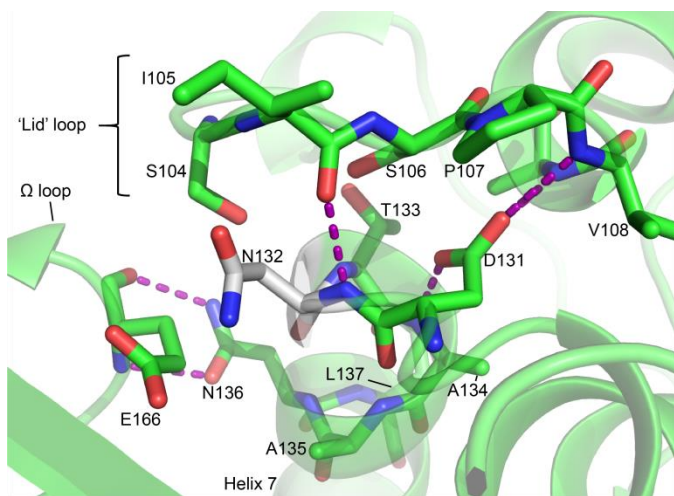
Figure 4.10. View of the BlaC active site with Asn132 modelled into a similar position that it takes in TEM-1. BlaC (PDB 5NJ2[28]) is displayed in transparent cartoon representation, with several residues that are mentioned in the text in stick representation. Several hydrogen bonds are indicated with purple dashed lines (all are 2.7 – 2.9 Å).

The question remains if the exchange process is involved in the functional differences between the enzyme and the mutant, increased clavulanate resistance and avibactam affinity, or if it is an unrelated side effect of the mutation. The protein exists in two almost equally populated states that interconvert slowly, and we cannot simply assume that the two states have equal properties. In the simplest model, the two observed states are similar to the two states that wt BlaC exhibits (Chapter 3). If it is assumed that one state hydrolyses clavulanic acid and binds avibactam much better than the other state, then the G132N mutation favours the former state. In this model, the 140-fold increase in carbamylation rate of avibactam observed by Soroka *et al.*[75] for G132N BlaC compared to the wt enzyme could be explained if the population of this active state changed from *ca.* 0.3 or 0.4 % in wt to 40 or 60 % in G132N, respectively. However, such a low population of the excited state in the wt BlaC is not in line with the NMR results. The population of the minor state in the wt enzyme must sizable to completely broaden the resonances of the four active site residues, as was discussed in Chapter 3. Furthermore, if the same state is also responsible for the increased hydrolysis of clavulanic acid acyl adduct, then the turnover rate of clavulanic acid should increase by the same factor 140. Soroka *et al.* found a k_{cat} of clavulanate hydrolysis by BlaC G132N of 0.4 ± 0.1 s^{-1} in 100 mM MES pH 6.4 at 293 K. The hydrolysis of clavulanate by wt BlaC was not detected in their experiments, but we have found turnover rates up to 2.3 ($\pm$ 0.2) 10^{-4} s^{-1} in the same buffer at 298 K (Chapter 2, [28]). This difference is almost an order of magnitude larger than the factor 140 in apparent avibactam affinity. Clearly, the functional effects of the G132N mutation cannot solely be explained by the increased population of state B. The insertion of an Asn

sidechain must change the shape and electronegativity of the active site surface. Even without dynamics, this could contribute to the altered functionality of the enzyme. For example, it is interesting to note that in structures of BlaC bound to avibactam, there is a gap between the active site wall containing Gly132 and the adduct (Figure 4.11a). Tassoni *et al.* have shown that this gap allows the avibactam adduct to rotate slightly away, releasing the sulphate moiety from the hydroxyl-binding pocket (Figure 4.11b). In SHV-1, which has a much higher affinity for avibactam than BlaC,[74,171] this gap is filled by the Asn132 sidechain. It may be that the shape of the BlaC binding pocket is simply not a very good match for avibactam and the G132N mutation increases affinity. Furthermore, the displacement of Ser104 and presumably the whole loop including gatekeeper residue Ile105 may make the binding site more accessible for avibactam.
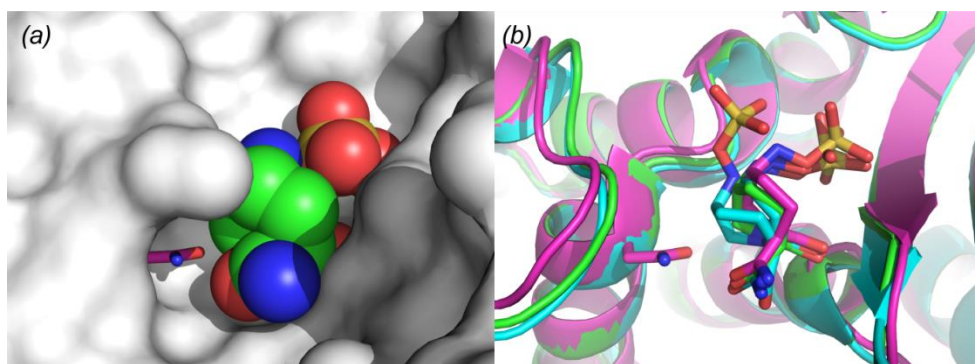

Figure 4.11. BlaC bound to avibactam. *(a)* The BlaC active site in surface representation bound to avibactam in spacefilling representation (PDB 4df6[41]). A gap is visible in between the adduct and the enzyme. In the gap, the Asn132 side chain of SHV-1 bound to avibactam (PDB 4zam[172] aligned to 4df6) is visible in sticks representation. *(b)* The same viewpoint and structures (4df6 in green, 4zam in magenta) as *(a)*, with the addition of another structure of BlaC bound to avibactam (PDB 6h2h[160] in cyan). Here, all structures are displayed in cartoon representation with the avibactam adducts in sticks. Two orientations of avibactam are visible in the 6h2h BlaC structure. The smallest heavy atom centre distance between the 4zam Asn132 side chain and the 6h2h normal avibactam orientation is 3.0 Å, while that between Asn132 and the tilted avibactam orientation is only 2.2 Å. This suggests that this avibactam orientation may not occur in BlaC G132N.

Further research will be required to elucidate the role of dynamics in clavulanate hydrolysis by BlaC G132N. However, the question of whether such dynamics are required to reach this phenotype in BlaC can be answered conclusively via comparison to another clavulanate-resistant mutant.

K234R

The dynamic behaviour of wt BlaC on the millisecond time scale (Chapter 3) is not detectable in mutant K234R. This indicates that the millisecond chemical exchange is not required for clavulanate hydrolysis. Moreover, as this mutant is able to hydrolyse at least ampicillin, bezylpenicillin, cephalothin[73] and nitrocefin, it forms direct evidence that the millisecond dynamics are not required for β-lactamase activity. Doucet *et al.* first reported

changes in millisecond dynamics in TEM-1 to correlate with functional differences,[103] but later observed that a laboratory-engineered chimeric β-lactamase displayed conserved function but strikingly increased dynamic behaviour.[111] To our knowledge, however, BlaC K234R is the first functional class A β-lactamase in which no millisecond dynamics could be detected in or near the active site. It is important to note, however, that the inability to detect such dynamics does not mean that no dynamics are present. An important indicator of the dynamic behaviour of the class A β-lactamases is the broadening of some of the resonances of their active site backbone amides. In BlaC, four of these amides are broadened beyond detection. While mutant K234R is the first BlaC variant in which the Thr235 backbone amide could be identified, we have still been unable to identify the resonances for the amide groups of Ser70, Ser130 and Thr237. These missing peaks suggest that an exchange process is still present, most likely too fast to probe using CPMG relaxation dispersion experiments ($\sim 50 - 3000$ s^{-1}) but too slow to affect the *NOE* ($\sim 10^{9} - 10^{12}$ s^{-1}). Such dynamics could possibly be measured using an R$_{1,rho}$ spin-lock experiment ($\sim 10^{3} - 10^{6}$ s^{-1}) or detected through residual dipolar couplings ($\sim 10^{3} - 10^{12}$ s^{-1}), but such experiments are outside the scope of this thesis.

Materials and methods

Error-prone PCR
Error-prone PCR mutagenesis was performed on an *Escherichia coli*-expression optimised DNA sequence (Figure S4.7) encoding the soluble domain of BlaC, using DreamTaq polymerase (0.1 U/µL, ThermoFisher Scientific), using the reaction conditions as recommended by the supplier but disturbed by the addition of manganese (0.2 mM), extra magnesium (2 mM) and skewed nucleotide concentrations (0.52 mM dCTP/dTTP vs 0.2 mM dATP/dGTP) in the reaction mixture. The primers that were used are listed in Table S4.1. Fifteen rounds of error-prone PCR were followed by purification of the reaction product using the Illustra GFX PCR DNA and Gel Band Purification Kit (GE LifeSciences) and another 25 rounds of non-error-prone PCR to further amplify the product. Primers for the second PCR (Table S4.1) anneal only to the product of the first reaction, not to the template. The product of the second PCR was purified as before and subsequently digested using restriction enzymes *Bgl*II and *Xho*I, with addition of *Dpn*I to digest any original template. The resulting gene fragments, containing only the coding sequence of soluble BlaC with semi-random combinations of mutations, were purified by agarose gel band extraction. These were subsequently cloned into similarly digested and purified pUK21-based vectors containing expression and subcellular localisation elements to create a cloning/expression plasmid capable of IPTG-induced expression of BlaC mutants fused to an N-terminal, TorA-derived protein export signal for use in *E. coli*. A map of the construct is shown in Figure S4.8. These plasmids were introduced into *E. coli*

strain KA797[173] using the chemical transformation method described by Inoue *et al.*,[170] yielding libraries of up to 0.5 million CFU per 200 µL transformation. Screening for clavulanate resistance was performed by incubating at 37 °C overnight on LB agar containing 50 µg/mL kanamycin sulfate, 1 mM IPTG, 8 µg/mL ampicillin and 1 µg/mL clavulanic acid. Colonies were transferred to separate liquid cultures and after overnight incubation, plasmids were isolated from the cells and used to transform fresh cells. Hits were only registered as valid if the plasmid also transmitted the same ampicillin/clavulanic acid-resistant phenotype to the fresh cells. Mutation frequency and bias in the library were controlled by Sanger sequencing of at least 10 randomly picked colonies from plates without ampicillin and clavulanic acid.

Site-directed mutagenesis

Site-directed mutations in the *blaC* gene, encoding the amino acid sequence as detailed in Figure S2.3, were made using a whole-plasmid synthesis approach, with the primers listed in Table S4.1. Incorporation of the correct mutations and absence of any other mutations was checked by comparison of Sanger sequencing data of each mutant from two sides (Baseclear BV, Leiden).

Protein production and purification

Pure BlaC of wt and mutants, without signal peptide and without purification tag, but with an N-terminal Gly residue instead of a Met (sequence as in Figure S2.3), was obtained as described previously (Chapter 2, [28]). The Ambler standard β-lactamase numbering scheme[17] is used throughout this thesis.

NMR spectroscopy

All NMR spectra were recorded on a Bruker AVIII HD 850 MHz (20 T) spectrometer equipped with a TCI cryoprobe. Unless mentioned otherwise, all experiments were performed on samples containing 0.38 mM ^{15}N enriched BlaC in 94 mM MES/NaOH pH 6.4 and 6% D_2O, at 298 K. HNCa spectra were measured on samples containing 0.6 and 0.28 mM ^{15}N^{13}C enriched BlaC G132N and K234R, respectively, in the same buffer. These spectra were recorded using the standard Bruker pulse program 'trhncaetgp3d', processed with Topspin 3.2 (Bruker Biospin, Leiderdorp) and analysed using CCPNmr Analysis.[143] Residue assignment of the peaks was performed by comparison of the HNCa to the assigned wt spectra (Chapter 3, BMRB ID 27888) and can be accessed under BMRB IDs 27889 for BlaC G132N and 27891 for BlaC K234R. *NOE* measurements were performed using standard Bruker pulse program 'hsqcnoef3gpsi' with a ^{1}H saturation delay of 4 s. *NOE* data were processed with Topspin 3.2 and resulting peak heights were fitted to exponential decay curves using Dynamics Center 2.5 (Bruker BioSpin, Rheinstetten).

CPMG relaxation dispersion measurements were performed using the TROSY CPMG pulse program as detailed by Vallurupalli *et al.*,[163] with 0, 1 (2x), 2, 3 (2x), 4, 6, 8, 10 (2x), 14, 18,

22, 28, 34 and 40 [15]N 180˚ pulses in 40 ms relaxation time, respectively. Data were processed with NMRPipe[164] and resulting resonances were fitted to a glore lineshape using FuDa.[97] Effective transverse relaxation rates ($R_{2,eff}$) were calculated from the fitted peak heights using an exponential decay function. Chemical exchange rate and p_B were determined using a grouped fit with the software CATIA.[97]

Chemical Exchange Saturation Transfer (CEST) measurements were performed using the standard Bruker "hsqc_cest_etf3gpsitc3d" pulse program, with 2.5 s recycle delay and 0.8 s B_1 irradiation at all frequencies in the ^{15}N range 100.5:0.5:130 ppm and field powers of 8 Hz and 26 Hz.

Figures containing protein structures were created using the PyMOL Molecular Graphics System, Version 2.2 Schrödinger, LLC.

Supplementary text

Optimisation of the library generation pipeline

The digestion / ligation approach was compared to Gibson Assembly (in-house), the InFusion Cloning Kit (Takara, Inc.) and the GeneMorph® II EZClone Domain Mutagenesis Kit (Agilent Technologies). The in-house digestion / ligation approach was chosen because it outscored the other approaches in the number of transformed mutants per transformation. The most efficient insert : vector ratio for ligation and subsequent transformation was found to be 3 or 4 : 1 (Figure S4.9). Strain KA797 was found to be the most efficient strain for transformation that was available in-house. Surprisingly, chemical transformation was found to yield more transformants than electrotransformation did. Commercial XL10-Gold cells were found to be ~3x more competent than KA797 cells when the latter were prepared via the standard in-house chemically competent cell preparation protocol, but an order of magnitude less than KA797 cells prepared via the 'Simple and Efficient Method' (SEM) described by Inoue *et al*.[170] (Table S4.2). Strain KA797 was also found to be a useful strain for library screening (Table S4.3). An ampicillin concentration of 8 µg/mL was found to be the minimum required concentration to prevent any non-resistant KA797 cell from forming a colony on the plate after transformation. Likewise, 1 µg/mL clavulanic acid was found to be enough to inhibit colony formation of all wild type BlaC expressing cells. When incubated at room temperature (with 1 mM IPTG), KA797 cells that were transformed with the BlaC cloning/expression plasmid were only resistant to ~2 µg/mL ampicillin (*vs*. ~16 µg/mL at 37 °C). Pre-induction with IPTG or switching to *E. coli* strain DH5α did not increase this MIC. Screening for mutants with increased clavulanic acid resistance but decreased temperature stability was therefore not attempted. Several of these optimisation experiments were performed in cooperation with Ralphe Drenth.

Supplementary figures
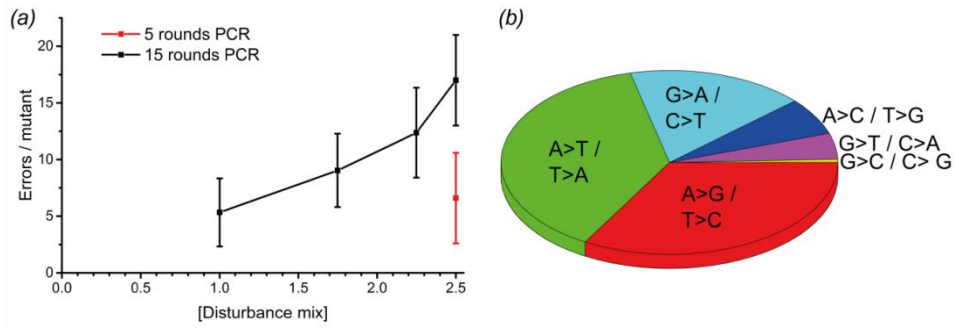
Figure S4.1. Semi-random mutagenesis. *(a)* Mutation frequency average and standard deviation as a function of the concentration of 'disturbance mix' consisting of 0.2 mM manganese, 2 mM extra magnesium and 0.32 mM extra dCTP/dTTP. Fifteen rounds of PCR with 1x disturbance mix was used for generation of the library. *(b)* Mutation bias, based on 369 single basepair replacements.

4

4
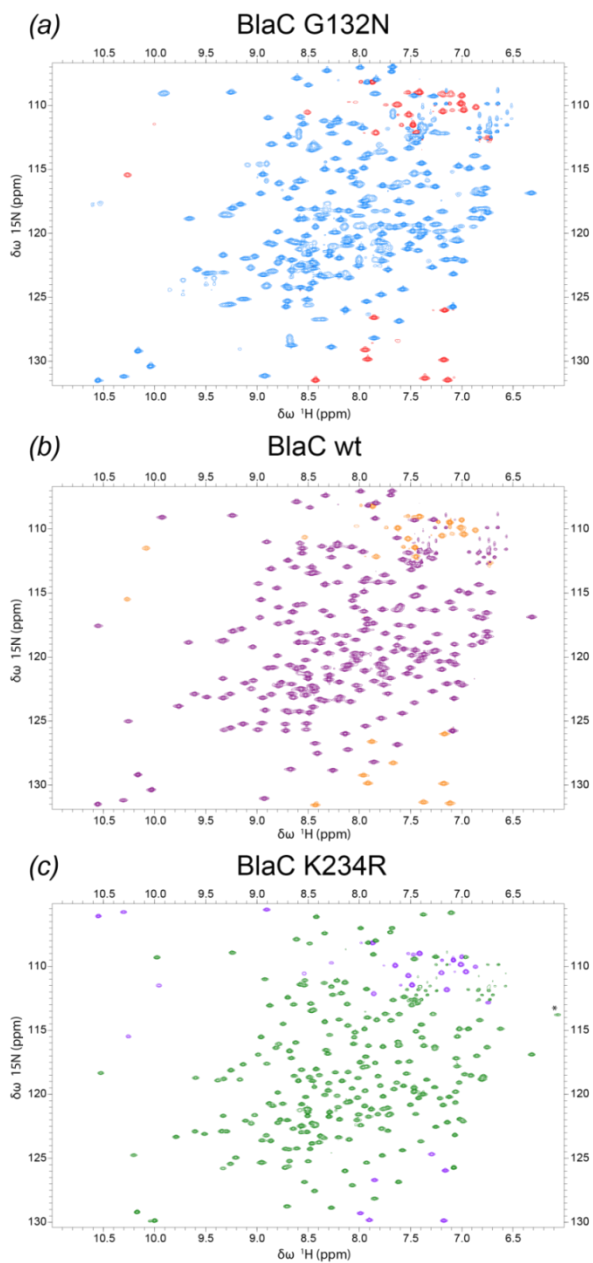
Figure S4.2. TROSY-HSQC spectra of BlaC wt and mutants. In each case, contour levels in the minority colour indicate folded peaks. Assignments can be accessed under Biological Magnetic Resonance Bank ID 27889. The resonance marked with an * in the BlaC K234R spectrum is assigned to the Thr235 amide.
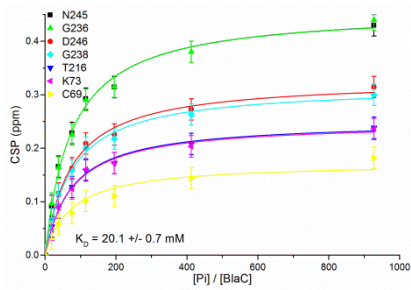
Figure S4.3. BlaC K234R – phosphate binding curves. The plot shows the CSPs upon phosphate titration for seven selected backbone amide resonances plotted against the ratio of the phosphate and BlaC concentrations. Data points are shown with an estimated peak picking error of ±0.02 ppm, error in K_D is the standard error of the global fit.
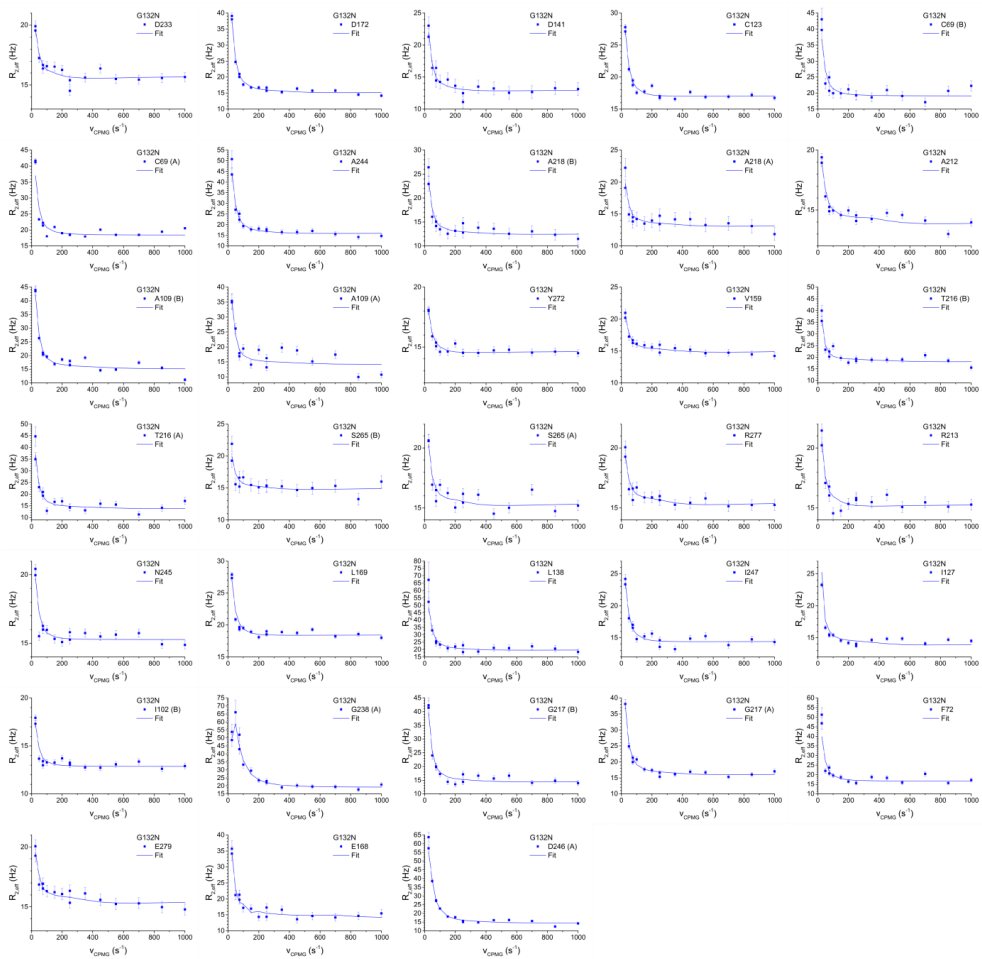
Figure S4.4. Relaxation dispersion curves of G132N backbone amides, with global fit. Error bars represent the standard deviation based on three duplicate CPMG frequencies.
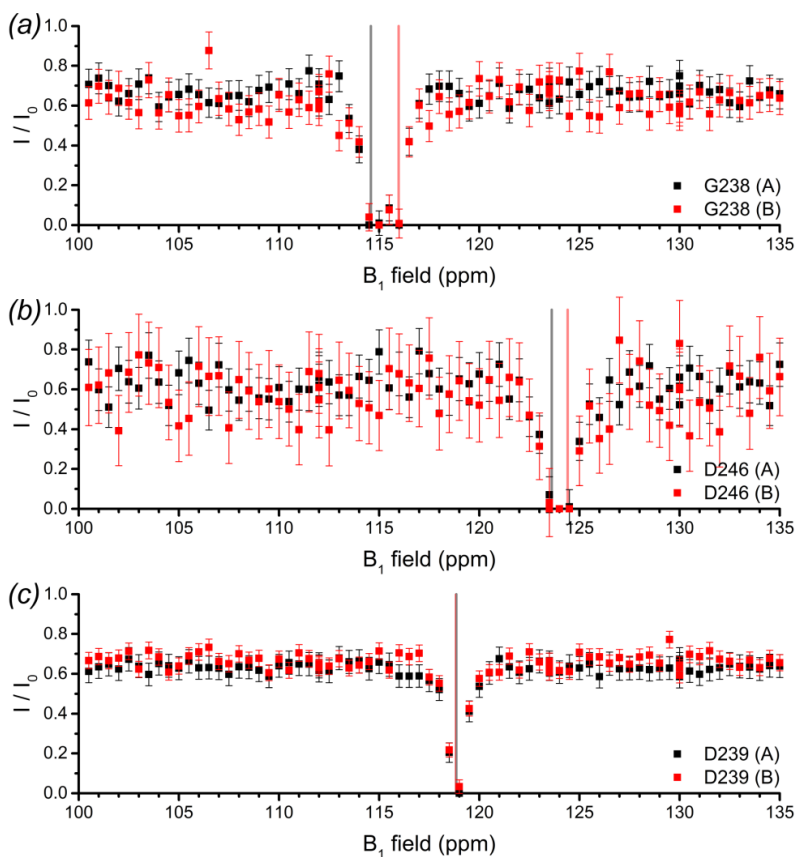
Figure S4.5. CEST profiles of G132N backbone amides Gly238 *(a)*, Asp246 *(b)* and Asp239 BlaC *(c)*. Vertical bars represent the peak positions of state A (black) and B (red). In panels *(a)* and *(b)*, the ^{15}N chemical shift difference between states A and B is large and exchange between the states can be observed via broadening of the two saturation dips. Panel *(c)* is included for reference, here the observable ^{15}N chemical shift difference between states A and B is small and the exchange is therefore not detectable. All other profiles (not shown) have profiles that are similar to *(c)*. Error bars indicate the standard deviation based on the spectral noise. These errors, especially those in *(b),* are very large due to the splitting and broadening of the peaks.
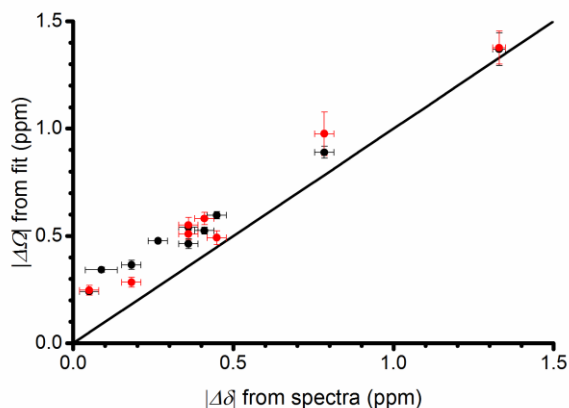
Figure S4.6. Correlation plot of the |ΔΩ| derived from relaxation dispersion NMR fits of the separate states A (black) and B (red) versus the ^{15}N chemical shift differences observed in the HSQC-spectrum for the two BlaC G132N states. The diagonal line indicates y=x. Y error bars represent standard deviation of the fit, x error bars represent estimated error in the peak picking. These fits were performed with p_b fixed at 0.4 and 0.6, respectively. The fit of state A relaxation dispersion data yielded an exchange rate estimate of 82 ± 3 s^{-1} and that of state B yielded 77 ± 5 s^{-1}.

```
ATGgccaataatgacctgtttcaggcaagccgtcgtcgtttttctggcacagctgggtggtctgaccgt
tgcaggtatgctgggtccgagcctgctgacaccgcgtcgtgcaaccgcagcacaggcaGATCTGGCAG
ATCGTTTTGCAGAACTGGAACGTCGTTATGATGCACGTCTGGGTGTTTATGTTCCGGCAACCGGCACC
ACCGCAGCAATTGAATATCGTGCAGATGAACGTTTTGCATTTTGCAGCACCTTTAAAGCACCGCTGGT
TGCAGCCGTTCTGCATCAGAATCCGCTGACCCATCTGGATAAACTGATTACCTATACCAGTGATGATA
TCCGTAGCATTAGTCCGGTTGCACAGCAGCATGTTCAGACCGGTATGACCATTGGTCAGCTGTGTGAT
GCAGCAATTCGTTATAGTGATGGCACCGCAGCCAATCTGCTGCTGGCCGATCTGGGTGGACCGGGTGG
TGGTACAGCAGCCTTTACCGGTTATCTGCGTAGCCTGGGTGATACCGTTAGCCGTCTGGATGCAGAAG
AACCGGAACTGAATCGTGATCCGCCTGGTGATGAACGTGATACCACCACACCGCATGCCATTGCACTG
GTTCTGCAGCAGCTGGTTCTGGGTAATGCACTGCCTCCGGATAAACGTGCACTGCTGACCGATTGGAT
GGCACGTAATACCACCGGTGCCAAACGTATTCGTGCAGGTTTTCCGGCAGATTGGAAAGTTATTGATA
AAACCGGTACGGGTGATTATGGTCGTGCAAATGATATTGCAGTTGTTTGGAGCCCGACCGGTGTTCCG
TATGTTGTTGCAGTTATGAGCGATCGTGCCGGTGGTGGCTATGATGCCGAACCGCGTGAAGCACTGCT
```

Figure S4.7. Sequence of the BlaC gene that was used for generation of the mutant library. Bases in upper case encode the BlaC protein, lower case italics encodes the TorA-derived protein export signal for use in *E. coli*, lower case without italics encodes a C-terminal 6-histidine purification tag.

Figure S4.8. Map of the cloning/expression plasmid used for generation of the mutant library. The section of DNA that was mutated through error-prone PCR is displayed in red.

Figure S4.9. Transformation efficiency as a function of ligation condition.

Supplementary tables

Table S4.1. Primers that were used in this study. Bases that are displayed in red indicate mutations with respect to the wild type sequence.

Process	Primer sequences (5' - 3')
Error-prone PCR	GCTAGCTCAGTCCTAGGTATAATGCTAGCGTTTAACTTTAAGAAGGAGATATACCATGG; CCCGGGAGCTCGAATTCCCTCAGTGGTGGTGGTGGTGGTG
Second amplification	CGCCACGGCGATATCGGATCCTTGACAGCTAGCTCAGTCCTAGGTATAATGC; CCCGGGAGCTCGAATTCCC

G132N mutagenesis	GCAGCAATTCGTTATAGTGAT**AA**CACCGCAGCCAATCTGCTGC; GCAGCAGATTGGCTGCGGTG**TT**ATCACTATAACGAATTGCTGC
K234R mutagenesis	GCAGATTGGAAAGTTATTGATA**G**AACCGGTACGGGTGATTATGG; CCATAATCACCCGTACCGGTT**C**TATCAATAACTTTCCAATCTGC
I105V mutagenesis	GTGATGATATCCGTAGC**G**TTAGTCCGGTTGCACAGC; GCTGTGCAACCGGACTAA**C**GCTACGGATATCATCAC
R213S mutagenesis	GCTGACCGATTGGATGGCA**A**GTAATACCACCGGTGCCAAACG; CGTTTGGCACCGGTGGTATTAC**T**TGCCATCCAATCGGTCAGC
H184R mutagenesis	CGTGATACCACCACACCGC**G**TGCCATTGCACTGGTTCTGC; GCAGAACCAGTGCAATGGCA**C**GCGGTGTGGTGGTATCACG
D172N mutagenesis	GCAGAAGAACCGGAACTGAATCGT**A**ATCCGCCTGGTGATGAACG; CGTTCATCACCAGGCGGAT**T**ACGATTCAGTTCCGGTTCTTCTGC

Table S4.2. Transformation efficiency of SEM competent *E. coli* KA797 as a function of DNA concentration. This test was performed with intact plasmids. The approximate amount of DNA per transformation that was used for the library generation is indicated in bold.

Plasmid (ng)	CFU ($\times 10^4$)	CFU / Plasmid molecule ($\times 10^{-5}$)	CFU / cell ($\times 10^{-4}$)
0.125	2	70	3
1.25	29	100	40
12.5	***142***	***50***	***200***
42.5	177	20	200
85	331	20	500
170	341	9	500
425	461	5	600
850	625	3	800

Table S4.3. Ampicillin Minimal Inhibitory Concentration (MIC) for several *E. coli* strains with and without BlaC. Plates were grown overnight at 37 °C in the presence of 1 mM IPTG, after application of 150 μL of cultures with 30 minutes pre-induction and cell density OD_{600} = 10.

Strain	Ampicillin MIC (μg/mL)	
	- BlaC	+ BlaC
KA797	2	32
BL21 Codon+	0.5	16
BL21 pLys CPF	0.5	16
BL21 STAR (DE3) pLys	1	32
BL21 pLysE	0.5	0.5
BL21 pLysS	0.5	64

4

Chapter 5

General conclusions and perspectives

> "*The time may come when penicillin can be bought by anyone in the shops. Then there is the danger that the ignorant man may easily underdose himself and by exposing his microbes to non-lethal quantities of the drug make them resistant.*" – Alexander Fleming, 1945

When the man who discovered the first antibiotic received his Nobel prize, he predicted the problem of antibiotic resistance. While his discovery heralded a healthcare revolution that allowed us to live without fear of infections for many decades, we are currently discovering the severity of his warning. It is up to us to find to find solutions. The research line in the Ubbink group, as described in Chapter 1, is geared towards the potential design of drugs that are more able to avoid the emergence of resistance. We do not know if this is possible at all, so that is what we are trying to find out. A question like this may take many years of research to answer and could lead to the conclusion that, after all, it is not possible to design such drugs. Yet even if this were to be so, it is important to realise that in fundamental research, much will be learned in the process – about the nature of the model system, as well as about the nature of evolution itself. Moreover, it is my strong belief that if enough people embark on projects like this, a small percentage of them will succeed in finding novel opportunities. Then if these opportunities are useful enough, the small percentage will be all that is needed. I am convinced that if this research line ever leads to an understanding of how to design drugs such that they are less prone to the development of resistance, it will be worth everything that was invested into it and much more. In this chapter, I will try to describe if and how the work presented in this thesis brings us closer to this goal. Subsequently, I will give a short overview of how our research fits in the more general progression of the field.

Overarching research line

The work presented here describes the first steps that were taken in the research line in the Ubbink group. The first steps mainly concern understanding of the model system itself. As it will be necessary to learn much about the model system, a model system was chosen that is interesting by itself. The most common method through which infectious bacteria develop resistance to antibiotics is through the production of a β-lactamase. The β-lactamase of *Mycobacterium tuberculosis* (Mtb) was chosen as model system. This

bacterium causes the most lethal infectious disease worldwide. Moreover, inhibition of its β-lactamase, BlaC, has recently emerged as a potential treatment option. Furthermore, the high promiscuity of BlaC makes it a suitable model system to study substrate adaptation.

Inhibition of BlaC, like other β-lactamases, is most commonly achieved with the substrate-like β-lactamase inhibitor clavulanic acid. In Chapter 2, inhibition of BlaC by clavulanic acid is shown not to be irreversible. Rather, BlaC is able to slowly hydrolyse clavulanic acid. This reaction is promoted by the presence of phosphate, which binds in the carboxy binding pocket of the BlaC active site. These findings contribute to the understanding of the BlaC–clavulanic acid interaction that is required to determine the conditions of future experiments on the system under study. Clearly, this is vital for the research line described here. An example of how the knowledge from this chapter influenced future experiments is that it identifies conditions in which it is possible to perform the type of lengthy experiments that are presented in Chapter 3.

Proteins do not exist in a single static conformation, but rather in an ensemble of dynamic conformations. The range, frequency and relevance of such conformational exchanges may differ from protein to protein. In related β-lactamases, motions in the millisecond time scale have been identified that could be correlated to the function of the enzyme[31] as well as to its evolution[109]. In order to fully understand the function of BlaC, therefore, an understanding of its conformational dynamics may be required. In Chapter 3, NMR dynamics experiments were used to show that like related β-lactamases, BlaC is very rigid on pico- to nanosecond time scale but shows significant dynamics in the millisecond timescale. This conformational exchange occurs at a rate of *ca*. 860 s^{-1} and is located in the active site of the protein. For the first time in any β-lactamase, the effect of inhibition on the conformational dynamics were also probed. Inhibition of BlaC with clavulanic acid leads to a major increase in the active site low millisecond dynamics and potentially destabilises the hydrophobic core of the α-domain.

These results improve upon the existing knowledge of the interaction between BlaC and inhibitor, but yield no information on the ability of BlaC to develop resistance to inhibition. To probe this, a large library of semi-random BlaC mutants was generated and tested for improved resistance against inhibition.

One might wonder if it is wise to purposely develop novel drug resistance. I would argue not only that the biosafety in our laboratory is relatively controlled, but also that in the host which was used here, *Escherichia coli*, inhibitor-resistant β-lactamases are unfortunately not novel at all. The notion of introducing novel resistance therefore does not apply. Furthermore, should this research progress towards introducing mutated *blaC* genes into *M. tuberculosis*, then indeed the biosafety level at which such experiments

would be performed will be much higher, to ensure that we cannot induce the spread of novel resistance.

Using the semi-random mutagenesis method, several mutants with improved resistance to clavulanic acid were identified. Of course, the identification of resistant mutants is only the first step towards understanding the mechanism through which resistance is achieved. The next step was to identify which (combinations of) mutations, amongst the multiple mutations in the resistant mutants, were responsible for the phenotype. In the mutants that were identified here, like in that which was engineered by Soroka *et al.*,[74] a single amino acid mutation was enough to reach a clavulanic acid-degrading phenotype. These two mutations, K234R and G132N, have been extensively characterised kinetically by others[73–75] while we were optimising our cloning pipeline for library generation. These biochemical characterisations yielded the information that at least the G132N mutation causes increased hydrolysis of the clavulanic acid BlaC acylenzyme adduct, but they provided no chemical models as to how this works for either mutation. In an attempt to gain more insight into this question, the tools described in Chapter 3 were used to study the dynamic behaviour of these two single amino acid mutants. These experiments showed that the two mutants, with similar functional phenotypes, displayed very different dynamic behaviour. While the relaxation dispersion measurements showed a striking increase of active site dynamics in the G132N mutant, they showed a severe decrease in the K234R mutant. This led to the conclusion that the active site dynamics are not required for enzymatic function of BlaC.

Unfortunately, while the results in Chapter 4 allowed speculation on possible models, no evidence for one or another chemical mechanism of clavulanate hydrolysis was obtained. Further clues could potentially be found through comparison of the two conformational states that were observed for BlaC G132N. For example, if only one of the states binds clavulanic acid, a rate-limiting step of 70 s^{-1} might be identified using time-resolved, pre-steady state kinetics between BlaC G132N and clavulanic acid. An assigned ^{1}H-^{15}N TROSY-HSQC spectrum of BlaC G132N bound to clavulanic acid could help to identify which of the states binds clavulanic acid, though this may be experimentally difficult to achieve due to the ability of this mutant to hydrolyse the inhibitor faster than the wt enzyme. Naturally, another approach would be to solve the crystal structures of these mutants. The insights derived from such structures could aid tremendously in the development of a chemical model for inhibitor hydrolysis, especially if, like the dynamics data of BlaC K234R seem to suggest, conformational dynamics are not essential for the reaction. In practice, however, past results have shown that it is challenging to explain the effects of many mutations in terms of structural changes, as the differences between crystal structures of variants with significantly different activities are often extremely subtle.[174] In such cases, it would be interesting to combine the cryogenic, static structures obtained from crystallography with NMR dynamics data at ambient temperature and molecular dynamics simulations. Such

combinations have proven valuable in the past (e.g. [102,104,106]) and this may also be applicable here. Currently, steps in all these directions are being undertaken within the Ubbink group.

Although the mechanisms of clavulanic acid hydrolysis by the two mutants described here have yet to be elucidated, it would nevertheless be interesting to investigate the effects of combinatorial mutations. The identification of combinatorial mutations has been an important argument for the employed experimental design, and indeed, such combinations have been shown to be capable of improving the clavulanic acid hydrolysing phenotype considerably.[73] The library generation pipeline described in Chapter 4 can also be exploited further to probe the existence of pathways towards inhibitor resistance that have not been explored yet.

For validity of any identified pathways in the model system itself, finally, the results will have to be tested in *M. tuberculosis*. This bacterium has a very different morphology and growth rate than *E. coli*, and past results have shown that results obtained through *in vitro* experiments do not always translate to this host in a straightforward manner.[29] The translation from resistance mechanisms to the potential design of drugs that can avoid these mechanisms will be even more challenging. A parallel research project within the Ubbink group focuses on residues that are conserved in BlaC and other class A β-lactamases. Through the combined understanding of which evolutionary routes are available and which parts of the enzyme are not available for mutation without loss of function, it may be possible to target inhibitors specifically to the latter parts.

Context of the field

Due to technological advances in areas such as saturation mutagenesis and deep sequencing, the understanding of the mutual effects of protein sequences and populations of organisms has grown rapidly over the past years.[175] Protein fitness landscapes have yielded insights into protein structure, stability and function which were recently reviewed by Gupta and Varadarajan[118], while those into epistasis were reviewed by Storz[114] and those into evolution by Canale *et al*.[129] as well as by Bastolla *et al.*[176] Here, I will shortly mention the recent insights that are most relevant for the current BlaC research line.

The saturation mutagenesis analyses of TEM-1[120,121] have provided information on the fitness effect of every single mutation in that protein. As explained in Chapter 1, this presents an alternative approach to the analysis of mutational landscapes that is complementary to, rather than competitive with the approach presented here. One of the central conclusions of such studies is that the epistasis, or context-dependence, of single point mutations in β-lactamases is high.[122] It could therefore be interesting to perform a similar analysis in BlaC.

Computational approaches are also revolutionising the field of protein science. For example, Jacquier *et al.* showed that it is possible, to some extent, to predict epistatic effects of mutations in TEM-1.[177] Others have computationally predicted inhibition efficiencies[178] and other protein parameters.[179,180] Importantly, conformational dynamics can also be probed computationally. This has been done through molecular dynamics simulations for at least a decade already, leading to useful insights such as those into TEM-1 dynamics by Fisette *et al.*[102] More recently, the time scale constraint of traditional molecular dynamics simulations is being challenged by novel ensemble techniques such as Markov State Modelling.[181] This technique has been applied to β-lactamases to explore how activity can be explained by hidden conformations[174] and to predict stabilizing mutations.[182] It would be interesting to pursue such avenues as complementary approaches in the research line presented here. This would be especially helpful in the model selection step, as NMR dynamics data can be difficult to interpret structurally.

Over the last few years, it has become increasingly clear that conformational dynamics can play an important role in evolutionary trajectories, with evolutionary changes occurring through conformational selection.[83,109] In this light, however modest the results presented in this thesis are, it could be said that the extension of our knowledge of BlaC towards its dynamic behaviour puts the research on this protein and its evolution in a different light. Specifically, our observation that a single point mutation can have dramatic effects on the millisecond dynamics of the protein raises concerns about the conclusions regarding the conservation of these dynamics. Kinetics and molecular dynamics experiments on resurrected Precambrian β-lactamases have shown that these ancestral proteins combine a broader substrate profile with increased fast conformational dynamics relative to the modern enzymes.[108,109,183] However, Risso *et al.* performed NMR dynamics experiments on an ancestral and a modern β-lactamase and observed the fast dynamics to be similar, while only the millisecond dynamics were more pronounced in the ancestral form.[110] They concluded that the slow dynamics relate to promiscuity. Our results suggest that perhaps the conclusion should instead be that fast conformational dynamics are more conserved in proteins than slow conformational dynamics are.

General perspectives on β-lactamases have recently been reviewed by Bush,[184] while specific insights into their inhibition were reviewed by Bush and Bradford,[40] Tehrani and Martin[185] and van den Akker and Bonomo.[39] These developments include the identification of an allosteric inhibition site in TEM-1.[186,187] It is currently not known if such a site also exists in BlaC, but based on the crystal structures, the targeted π-stacking PWP triad in TEM-1 does not appear to have a conserved orientation in BlaC. The most important development in the field of β-lactamase inhibition has been the clinical approval of several new β-lactamase inhibitors such as avibactam, vaborbactam and relebactam. While the former has a relatively low affinity for BlaC,[75] it has nevertheless been shown to display potent sterilising activity against multi-drug-resistant *M.*

tuberculosis when combined with ceftazidime.[188] Furthermore, all these inhibitors were shown to enhance the potency of several β-lactams against at least *Mycobacterium abscessus*.[189–191] It is therefore interesting to expand the scope of the research line to these new inhibitors, which is currently being done within the Ubbink group.

Still, most studies on the treatment of tuberculosis with β-lactam / β-lactamase inhibitor cocktails use clavulanic acid. Several clinical results give hope for the effective use of clavulanic acid with meropenem or tebipenem,[47,48,50,52,53,57–59] strong antibiotics that are such slow substrates for BlaC that they are practically inhibitors themselves.[22,43] The gain of resistance to these combinations through mutation of BlaC may be more difficult to achieve than to the combination of clavulanic acid and ampicillin, which was tested here. It would be interesting to utilise the mutagenesis and screening approach presented here to test this hypothesis. These and other new treatment options for tuberculosis have recently been reviewed by Tiberi *et al.,* who came to the conclusion that the arrival of new drugs and new treatment strategies brings hope to this plagued field.[13]

In conclusion, the work presented in this thesis provides improvements in the basic understanding of the model protein BlaC and its inhibition by clavulanic acid, as well as several tools that can be used to study these phenomena. Alas, these are rather modest steps in the light of goals such as the understanding of protein evolution and the development of drugs with improved evolution resistance. Nevertheless, these modest steps may one day contribute to something greater. After all, no great discoveries can be made without the tools to study the phenomena they describe.

5

References

1. Daniel, T. M. The history of tuberculosis. *Respir. Med.* **100**, 1862–1870 (2006).
2. Rubin, S. A. Tuberculosis. Captain of all these men of death. *Radiol. Clin. North Am.* **33**, 619–639 (1995).
3. McAdam, K. P. W. J. Book Review In the shadow of tuberculosis. *N. Engl. J. Med.* **332**, 1106–1109 (1995).
4. World Health Organization. *Global Tuberculosis Report*. *Tuberculosis* (World Health Organization, 2015). doi:978 92 4 156450 2
5. World Health Organization. *Global tuberculosis report 2016*. (2016).
6. World Health Organization. *Global tuberculosis report 2017*. (2017).
7. Centers for Disease Control and Prevention (CDC). Emergence of Mycobacterium tuberculosis with extensive resistance to second-line drugs--worldwide, 2000-2004. *MMWR. Morb. Mortal. Wkly. Rep.* **55**, 301–305 (2006).
8. World Health Organisation. Extensively drug-resistant tuberculosis (XDR-TB): recommendations for prevention and control. *Relev. Epidemiol. Hebd.* **81**, 430–432 (2006).
9. World Health Organisation. WHO | Drug-resistant TB: Totally drug-resistant TB FAQ. *WHO* (2018). Available at: http://www.who.int/tb/areas-of-work/drug-resistant-tb/totally-drug-resistant-tb-faq/en/. (Accessed: 28th August 2018)
10. Velayati, A. A. *et al.* Emergence of new forms of totally drug-resistant tuberculosis bacilli: super extensively drug-resistant tuberculosis or totally drug-resistant strains in iran. *Chest* **136**, 420–425 (2009).
11. Udwadia, Z. F., Amale, R. A., Ajbani, K. K. & Rodrigues, C. Totally Drug-Resistant Tuberculosis in India. *Clin. Infect. Dis.* **54**, 579–581 (2012).
12. Wallis, R. S. *et al.* Tuberculosis—advances in development of new drugs, treatment regimens, host-directed therapies, and biomarkers. *Lancet Infect. Dis.* **16**, e34–e46 (2016).
13. Tiberi, S. *et al.* New drugs and perspectives for new anti-tuberculosis regimens. *Pulmonology* **24**, 86–98 (2018).
14. Voladri, R. K. *et al.* Recombinant expression and characterization of the major beta-lactamase of *Mycobacterium tuberculosis*. *Antimicrob. Agents Chemother.* **42**, 1375–1381 (1998).
15. Flores, A. R., Parsons, L. M. & Pavelka, M. S. Genetic analysis of the beta-lactamases of *Mycobacterium tuberculosis* and *Mycobacterium smegmatis* and susceptibility to beta-lactam antibiotics. *Microbiology* **151**, 521–532 (2005).
16. Wang, F., Cassidy, C. & Sacchettini, J. C. Crystal structure and activity studies of the *Mycobacterium tuberculosis* β-lactamase reveal its critical role in resistance to β-lactam antibiotics. *Antimicrob. Agents Chemother.* **50**, 2762–2771 (2006).
17. Ambler, R. P. & Coulson, A. F. W. A standard numbering scheme for the Class A beta-lactamases. *Biochem. J.* **276**, 269–272 (1991).
18. Hugonnet, J.-E. & Blanchard, J. S. Irreversible inhibition of the *Mycobacterium tuberculosis* beta-lactamase by clavulanate. *Biochemistry* **46**, 11998–12004 (2007).

19. Meroueh, S. O., Fisher, J. F., Schlegel, H. B. & Mobashery, S. Ab Initio QM/MM Study of Class A β-Lactamase Acylation: Dual Participation of Glu166 and Lys73 in a Concerted Base Promotion of Ser70. *J. Am. Chem. Soc.* **127**, 15397–15407 (2005).

20. Vandavasi, V. G. *et al.* Exploring the Mechanism of β-Lactam Ring Protonation in the Class A β-lactamase Acylation Mechanism Using Neutron and X-ray Crystallography. *J. Med. Chem.* **59**, 474–479 (2016).

21. Tremblay, L. W., Xu, H. & Blanchard, J. S. Structures of the Michaelis complex (1.2 Å) and the covalent acyl intermediate (2.0 Å) of cefamandole bound in the active sites of the *Mycobacterium tuberculosis* β-lactamase K73A and E166A mutants. *Biochemistry* **49**, 9685–9687 (2010).

22. Chow, C., Xu, H. & Blanchard, J. S. Kinetic characterization of hydrolysis of nitrocefin, cefoxitin, and meropenem by β-lactamase from *Mycobacterium tuberculosis*. *Biochemistry* **52**, 4097–4104 (2013).

23. McDonough, J. A., Hacker, K. E., Flores, A. R., Pavelka, M. S. & Braunstein, M. The twin-arginine translocation pathway of *Mycobacterium smegmatis* is functional and required for the export of mycobacterial beta-lactamases. *J. Bacteriol.* **187**, 7667–7679 (2005).

24. McDonough, J. A. *et al.* Identification of functional Tat signal sequences in *Mycobacterium tuberculosis* proteins. *J. Bacteriol.* **190**, 6428–6438 (2008).

25. Bush, K. Characterization of beta-lactamases. *Antimicrob. Agents Chemother.* **33**, 259–263 (1989).

26. Bush, K., Jacoby, G. A. & Medeiros, A. A. A functional classification scheme for beta-lactamases and its correlation with molecular structure. *Antimicrob. Agents Chemother.* **39**, 1211–1233 (1995).

27. Bush, K. & Jacoby, G. A. Updated functional classification of beta-lactamases. *Antimicrob. Agents Chemother.* **54**, 969–976 (2010).

28. Elings, W. *et al.* Phosphate promotes the recovery of *Mycobacterium tuberculosis* β-lactamase from clavulanic acid inhibition. *Biochemistry* **56**, 6257–6267 (2017).

29. Kurz, S. G. *et al.* Can inhibitor-resistant substitutions in the *Mycobacterium tuberculosis* β-Lactamase BlaC lead to clavulanate resistance?: a biochemical rationale for the use of β-lactam-β-lactamase inhibitor combinations. *Antimicrob. Agents Chemother.* **57**, 6085–6096 (2013).

30. Feiler, C. *et al.* Directed evolution of *Mycobacterium tuberculosis* β-lactamase reveals gatekeeper residue that regulates antibiotic resistance and catalytic efficiency. *PLoS One* **8**, e73123 (2013).

31. Doucet, N., De Wals, P.-Y. & Pelletier, J. N. Site-saturation mutagenesis of Tyr-105 reveals its importance in substrate stabilization and discrimination in TEM-1 beta-lactamase. *J. Biol. Chem.* **279**, 46295–46303 (2004).

32. Jelsch, C., Mourey, L., Masson, J.-M. & Samama, J.-P. Crystal structure of *Escherichia coli* TEM1 β-lactamase at 1.8 Å resolution. *Proteins Struct. Funct. Genet.* **16**, 364–383 (1993).

33. Kuzin, A. P. *et al.* Structure of the SHV-1 β-Lactamase. *Biochemistry* **38**, 5720–5727 (1999).

34. Tremblay, L. W., Fan, F. & Blanchard, J. S. Biochemical and Structural Characterization of *Mycobacterium tuberculosis* β-Lactamase with the

Carbapenems Ertapenem and Doripenem. *Biochemistry* **49**, 3766–3773 (2010).

35. Robin, F. *et al.* TEM-109 (CMT-5), a natural complex mutant of TEM-1 beta-lactamase combining the amino acid substitutions of TEM-6 and TEM-33 (IRT-5). *Antimicrob. Agents Chemother.* **49**, 4443–4447 (2005).

36. Poirel, L. *et al.* Emergence in Klebsiella pneumoniae of a chromosome-encoded SHV beta-lactamase that compromises the efficacy of imipenem. *Antimicrob. Agents Chemother.* **47**, 755–758 (2003).

37. Ourghanlian, C., Soroka, D. & Arthur, M. Inhibition by avibactam and clavulanate of the β-lactamases KPC-2 and CTX-M-15 harboring the substitution N132G in the conserved motif SDN. *AAC Accept. Manuscr. Posted Online Antimicrob. Agents Chemother* (2017). doi:10.1128/AAC.02510-16

38. Drawz, S. M. & Bonomo, R. A. Three decades of β-lactamase inhibitors. *Clin. Microbiol. Rev.* **23**, 160–201 (2010).

39. van den Akker, F. & Bonomo, R. A. Exploring additional dimensions of complexity in inhibitor design for serine β-lactamases: mechanistic and intra- and inter-molecular chemistry approaches. *Front. Microbiol.* **9**, 622 (2018).

40. Bush, K. & Bradford, P. A. Interplay between β-lactamases and new β-lactamase inhibitors. *Nat. Rev. Microbiol.* **17**, 295–306 (2019).

41. Xu, H., Hazra, S. & Blanchard, J. S. NXL104 irreversibly inhibits the β-lactamase from *Mycobacterium tuberculosis*. *Biochemistry* **51**, 4551–4557 (2012).

42. Kurz, S. G. *et al.* Inhibiting the beta-lactamase of *Mycobacterium tuberculosis* (Mtb) with novel boronic acid transition-state inhibitors (BATSIs). *ACS Infect. Dis.* **1**, 234–242 (2016).

43. Hazra, S., Xu, H. & Blanchard, J. S. Tebipenem, a new carbapenem antibiotic, is a slow substrate that inhibits the β-lactamase from *Mycobacterium tuberculosis*. *Biochemistry* **53**, 3671–3678 (2014).

44. Hazra, S. *et al.* Kinetic and structural characterization of the interaction of 6-methylidene penem 2 with the beta-lactamase from *Mycobacterium tuberculosis*. *Biochemistry* **54**, 5657–5664 (2015).

45. Chambers, H. F. *et al.* Can penicillins and other beta-lactam antibiotics be used to treat tuberculosis? *Antimicrob. Agents Chemother.* **39**, 2620–2624 (1995).

46. Kurz, S. G. & Bonomo, R. A. Reappraising the use of β-lactams to treat tuberculosis. *Expert Rev. Anti. Infect. Ther.* **10**, 999–1006 (2012).

47. Hugonnet, J.-E., Tremblay, L. W., Boshoff, H. I., Barry, C. E. & Blanchard, J. S. Meropenem-clavulanate is effective against extensively drug-resistant *Mycobacterium tuberculosis*. *Science* **323**, 1215–1218 (2009).

48. Payen, M. C. *et al.* Clinical use of the meropenem-clavulanate combination for extensively drug-resistant tuberculosis. *Int. J. Tuberc. Lung Dis.* **16**, 558–560 (2012).

49. Gonzalo, X. & Drobniewski, F. Is there a place for β-lactams in the treatment of multidrug-resistant/extensively drug-resistant tuberculosis? Synergy between meropenem and amoxicillin/clavulanate. *J. Antimicrob. Chemother.* **68**, 366–369 (2013).

50. Forsman, L. D. *et al.* Meropenem-clavulanic acid has high in vitro activity against multidrug-resistant *Mycobacterium tuberculosis*. *Antimicrob. Agents Chemother.* **59**, 3630–3632 (2015).

51.   Jaganath, D., Lamichhane, G. & Shah, M. Carbapenems against *Mycobacterium tuberculosis*: a review of the evidence. *Int. J. Tuberc. Lung Dis.* **20**, 1436–1447 (2016).

52.   Payen, M. C. *et al.* Meropenem-clavulanate for drug-resistant tuberculosis: a follow-up of relapse-free cases. *Int. J. Tuberc. Lung Dis.* **22**, 34–39 (2018).

53.   Tiberi, S. *et al.* Effectiveness and safety of meropenem/clavulanate-containing regimens in the treatment of MDR- and XDR-TB. *Eur. Respir. J.* **47**, 1235–1243 (2016).

54.   Tiberi, S. *et al.* Comparison of effectiveness and safety of imipenem/clavulanate- versus meropenem/clavulanate-containing regimens in the treatment of MDR- and XDR-TB. *Eur. Respir. J.* 13993003.00214-2016- (2016). doi:10.1183/13993003.00214-2016

55.   Chambers, H. F., Kocagöz, T., Sipit, T., Turner, J. & Hopewell, P. C. Activity of amoxicillin/clavulanate in patients with tuberculosis. *Clin. Infect. Dis.* **26**, 874–877 (1998).

56.   Rullas, J. *et al.* Combinations of β-lactam antibiotics currently in clinical trials are efficacious in a DHP-I deficient mice model of TB infection. *Antimicrob. Agents Chemother.* **59**, 4997–4999 (2015).

57.   Li, F. *et al.* In Vitro Activity of β-Lactams in Combination with β-Lactamase Inhibitors against *Mycobacterium tuberculosis* Clinical Isolates. *Biomed Res. Int.* **2018**, 3579832 (2018).

58.   De Lorenzo, S. *et al.* Efficacy and safety of meropenem-clavulanate added to linezolid-containing regimens in the treatment of MDR-/XDR-TB. *Eur. Respir. J.* **41**, 1386–1392 (2013).

59.   England, K. *et al.* Meropenem-clavulanic acid shows activity against *Mycobacterium tuberculosis in vivo. Antimicrob. Agents Chemother.* **56**, 3384–3387 (2012).

60.   Dhar, N. *et al.* Rapid cytolysis of *Mycobacterium tuberculosis* by faropenem, an orally bioavailable β-lactam antibiotic. *Antimicrob. Agents Chemother.* **59**, 1308–1319 (2015).

61.   Blair, J. M. A., Webber, M. A., Baylay, A. J., Ogbolu, D. O. & Piddock, L. J. V. Molecular mechanisms of antibiotic resistance. *Nat. Rev. Microbiol.* **13**, 42–51 (2015).

62.   Delcour, A. H. Outer membrane permeability and antibiotic resistance. *Biochim. Biophys. Acta - Proteins Proteomics* **1794**, 808–816 (2009).

63.   Blondiaux, N. *et al.* Reversion of antibiotic resistance in *Mycobacterium tuberculosis* by spiroisoxazoline SMARt-420. *Science* **355**, 1206–1211 (2017).

64.   Hall, B. G. & Barlow, M. Evolution of the serine beta-lactamases: past, present and future. *Drug Resist. Updat.* **7**, 111–123 (2004).

65.   Sulton, D. *et al.* Clavulanic Acid Inactivation of SHV-1 and the Inhibitor-resistant S130G SHV-1 β-Lactamase. *J. Biol. Chem.* **280**, 35528–35536 (2005).

66.   Thomson, J. M., Distler, A. M., Prati, F. & Bonomo, R. A. Probing active site chemistry in SHV beta-lactamase variants at Ambler position 244. Understanding unique properties of inhibitor resistance. *J. Biol. Chem.* **281**, 26734–26744 (2006).

67.   Helfand, M. S. *et al.* Understanding resistance to beta-lactams and beta-lactamase inhibitors in the SHV beta-lactamase: lessons from the mutagenesis of SER-130. *J.*

Biol. Chem. **278**, 52724–52729 (2003).

68. Mendonça, N. *et al.* The Lys234Arg substitution in the enzyme SHV-72 is a determinant for resistance to clavulanic acid inhibition. *Antimicrob. Agents Chemother.* **52**, 1806–1811 (2008).

69. Papp-Wallace, K. M., Winkler, M. L., Taracila, M. A. & Bonomo, R. A. Variants of β-lactamase KPC-2 that are resistant to inhibition by avibactam. *Antimicrob. Agents Chemother.* **59**, 3710–7 (2015).

70. Bermudes, H. *et al.* Molecular Characterization of TEM-59 (IRT-17), a Novel Inhibitor-Resistant TEM-Derived beta -Lactamase in a Clinical Isolate of *Klebsiella oxytoca*. *Antimicrob. Agents Chemother.* **43**, 1657–1661 (1999).

71. Drawz, S. M. *et al.* The Role of a Second-Shell Residue in Modifying Substrate and Inhibitor Interactions in the SHV β-Lactamase: A Study of Ambler Position Asn276. *Biochemistry* **48**, 4557–4566 (2009).

72. Prinarakis, E. E., Miriagou, V., Tzelepi, E., Gazouli, M. & Tzouvelekis, L. S. Emergence of an inhibitor-resistant beta-lactamase (SHV-10) derived from an SHV-5 variant. *Antimicrob. Agents Chemother.* **41**, 838–840 (1997).

73. Egesborg, P., Carlettini, H., Volpato, J. P. & Doucet, N. Combinatorial active-site variants confer sustained clavulanate resistance in BlaC β-lactamase from *Mycobacterium tuberculosis*. *Protein Sci.* **24**, 534–544 (2015).

74. Soroka, D. *et al.* Hydrolysis of clavulanate by *Mycobacterium tuberculosis* β-lactamase BlaC harboring a canonical SDN motif. *Antimicrob. Agents Chemother.* **59**, 5714–5720 (2015).

75. Soroka, D. *et al.* Inhibition of β-lactamases of mycobacteria by avibactam and clavulanate. *J. Antimicrob. Chemother.* **72**, 1081–1088 (2017).

76. Yon, J. M., Perahia, D. & Ghélis, C. Conformational dynamics and enzyme activity. *Biochimie* **80**, 33–42 (1998).

77. Wand, A. J. Dynamic activation of protein function: A view emerging from NMR spectroscopy. *Nat. Struct. Biol.* **8**, 926–931 (2001).

78. Kay, L. E. NMR studies of protein structure and dynamics. *J. Magn. Reson.* **173**, 193–207 (2005).

79. Mittermaier, A. K. & Kay, L. E. Observing biological dynamics at atomic resolution using NMR. *Trends Biochem. Sci.* **34**, 601–611 (2009).

80. Bellissent-Funel, M.-C. *et al.* Water Determines the Structure and Dynamics of Proteins. *Chem. Rev.* **116**, 7673–7697 (2016).

81. Kovermann, M., Rogne, P. & Wolf-Watz, M. Protein dynamics and function from solution state NMR spectroscopy. *Quarterly reviews of biophysics* **49**, e6 (2016).

82. Narayanan, C., Bafna, K., Roux, L. D., Agarwal, P. K. & Doucet, N. Applications of NMR and computational methodologies to study protein dynamics. *Arch. Biochem. Biophys.* **628**, 71–80 (2017).

83. Petrović, D., Risso, V. A., Kamerlin, S. C. L. & Sanchez-Ruiz, J. M. Conformational dynamics and enzyme evolution. *J. R. Soc. Interface* **15**, (2018).

84. Abragam, A. The principles of nuclear magnetism. *Nucl. Phys.* **28**, 692–693 (1961).

85. Lipari, G. & Szabo, A. Model-free approach to the interpretation of nuclear magnetic resonance relaxation in macromolecules. 1. Theory and range of validity. *J. Am. Chem. Soc.* **104**, 4546–4559 (1982).

86. Lipari, G. & Szabo, A. Model-free approach to the interpretation of nuclear

magnetic resonance relaxation in macromolecules. 2. Analysis of experimental results. *J. Am. Chem. Soc.* **104**, 4559–4570 (1982).

87. Korzhnev, D. M., Billeter, M., Arseniev, A. S. & Orekhov, V. Y. NMR studies of Brownian tumbling and internal motions in proteins. *Prog. Nucl. Magn. Reson. Spectrosc.* **38**, 197–266 (2001).

88. d'Auvergne, E. J. Protein dynamics: a study of the model-free analysis of NMR relaxation data. (2006).

89. Cavanagh, J., Skelton, N. J., Fairbrother, W. J., Rance, M. & Palmer, A. G. I. *Protein NMR spectroscopy : principles and practice*. (Academic Press, 2007).

90. Keeler, J. *Understanding NMR spectroscopy*. (John Wiley and Sons, 2010).

91. Walker, O., Varadan, R. & Fushman, D. Efficient and accurate determination of the overall rotational diffusion tensor of a molecule from 15N relaxation data using computer program ROTDIF. *J. Magn. Reson.* **168**, 336–345 (2004).

92. Carr, H. Y. & Purcell, E. M. Effects of Diffusion on Free Precession in Nuclear Magnetic Resonance Experiments. *Phys. Rev.* **94**, 630–638 (1954).

93. Meiboom, S. & Gill, D. Modified Spin-Echo Method for Measuring Nuclear Relaxation Times. *Rev. Sci. Instrum.* **29**, 688–691 (1958).

94. Ishima, R. CPMG Relaxation Dispersion. in 29–49 (Humana Press, Totowa, NJ, 2014). doi:10.1007/978-1-62703-658-0_2

95. Bloch, F. Nuclear Induction. *Phys. Rev.* **70**, 460–474 (1946).

96. McConnell, H. M. Reaction Rates by Nuclear Magnetic Resonance. *J. Chem. Phys.* **28**, 430–431 (1958).

97. Hansen, D. F., Vallurupalli, P., Lundström, P., Neudecker, P. & Kay, L. E. Probing chemical shifts of invisible states of proteins with relaxation dispersion NMR spectroscopy: How well can we do? *J. Am. Chem. Soc.* **130**, 2667–2675 (2008).

98. Palmer, A. G., Kroenke, C. D. & Patrick Loria, J. Nuclear Magnetic Resonance Methods for Quantifying Microsecond-to-Millisecond Motions in Biological Macromolecules. *Methods Enzymol.* **339**, 204–238 (2001).

99. Ban, D. *et al.* Exceeding the limit of dynamics studies on biomolecules using high spin-lock field strengths with a cryogenically cooled probehead. *J. Magn. Reson.* **221**, 1–4 (2012).

100. Vallurupalli, P., Bouvignies, G. & Kay, L. E. Studying 'invisible' excited protein states in slow exchange with a major state conformation. *J. Am. Chem. Soc.* **134**, 8148–8161 (2012).

101. Savard, P.-Y. & Gagné, S. M. Backbone dynamics of TEM-1 determined by NMR: Evidence for a highly ordered protein. *Biochemistry* **45**, 11414–11424 (2006).

102. Fisette, O., Morin, S., Savard, P.-Y., Lagüe, P. & Gagné, S. M. TEM-1 backbone dynamics-insights from combined molecular dynamics and nuclear magnetic resonance. *Biophys. J.* **98**, 637–645 (2010).

103. Doucet, N., Savard, P.-Y., Pelletier, J. N. & Gagné, S. M. NMR investigation of Tyr105 mutants in TEM-1 beta-lactamase: dynamics are correlated with function. *J. Biol. Chem.* **282**, 21448–21459 (2007).

104. Morin, S. & Gagné, S. M. NMR Dynamics of PSE-4 β-Lactamase: An Interplay of ps-ns Order and μs-ms Motions in the Active Site. *Biophys. J.* **96**, 4681–4691 (2009).

105. Roccatano, D. *et al.* Dynamical Aspects of TEM-1 β-Lactamase Probed by Molecular Dynamics. *J. Comput. Aided. Mol. Des.* **19**, 329–340 (2005).

106. Fisette, O., Gagné, S. & Lagüe, P. Molecular Dynamics of Class A β-lactamases—Effects of Substrate Binding. *Biophys. J.* **103**, 1790–1801 (2012).

107. Clouthier, C. M. *et al.* Chimeric β-Lactamases: Global Conservation of Parental Function and Fast Time-Scale Dynamics with Increased Slow Motions. *PLoS One* **7**, e52283 (2012).

108. Risso, V. A., Gavira, J. A., Mejia-Carmona, D. F., Gaucher, E. A. & Sanchez-Ruiz, J. M. Hyperstability and Substrate Promiscuity in Laboratory Resurrections of Precambrian β-Lactamases. *J. Am. Chem. Soc.* **135**, 2899–2902 (2013).

109. Zou, T., Risso, V. A., Gavira, J. A., Sanchez-Ruiz, J. M. & Ozkan, S. B. Evolution of Conformational Dynamics Determines the Conversion of a Promiscuous Generalist into a Specialist Enzyme. *Mol. Biol. Evol.* **32**, 132–143 (2015).

110. Risso, V. A. *et al.* De novo active sites for resurrected Precambrian enzymes. *Nat. Commun.* **8**, 16113 (2017).

111. Gobeil, S. M. C. *et al.* Maintenance of Native-like Protein Dynamics May Not Be Required for Engineering Functional Proteins. *Chem. Biol.* **21**, 1330–1340 (2014).

112. Frederick, T. E. & Peng, J. W. A gratuitous β-Lactamase inducer uncovers hidden active site dynamics of the Staphylococcus aureus BlaR1 sensor domain. *PLoS One* **13**, e0197241 (2018).

113. Knox, R., Lento, C. & Wilson, D. J. Mapping Conformational Dynamics to Individual Steps in the TEM-1 β-Lactamase Catalytic Mechanism. *J. Mol. Biol.* (2018). doi:10.1016/J.JMB.2018.06.045

114. Storz, J. F. Compensatory mutations and epistasis for protein function. *Current Opinion in Structural Biology* **50**, 18–25 (2018).

115. de Visser, J. A. G. M. & Krug, J. Empirical fitness landscapes and the predictability of evolution. *Nat. Rev. Genet.* **15**, 480–490 (2014).

116. Fowler, D. M. & Fields, S. Deep mutational scanning: a new style of protein science. *Nat. Methods* **11**, 801–807 (2014).

117. Kitzman, J. O., Starita, L. M., Lo, R. S., Fields, S. & Shendure, J. Massively parallel single-amino-acid mutagenesis. *Nat. Methods* **12**, 203–206, 4 p following 206 (2015).

118. Gupta, K. & Varadarajan, R. Insights into protein structure, stability and function from saturation mutagenesis. *Curr. Opin. Struct. Biol.* **50**, 117–125 (2018).

119. Firnberg, E. & Ostermeier, M. PFunkel: Efficient, Expansive, User-Defined Mutagenesis. *PLoS One* **7**, e52031 (2012).

120. Firnberg, E., Labonte, J. W., Gray, J. J. & Ostermeier, M. A Comprehensive, High-Resolution Map of a Gene's Fitness Landscape. *Mol. Biol. Evol.* **31**, 1581–1592 (2014).

121. Stiffler, M. A., Hekstra, D. R. & Ranganathan, R. Evolvability as a function of purifying selection in TEM-1 β-lactamase. *Cell* **160**, 882–892 (2015).

122. Steinberg, B. & Ostermeier, M. Shifting Fitness and Epistatic Landscapes Reflect Trade-offs along an Evolutionary Pathway. *J. Mol. Biol.* **428**, 2730–2743 (2016).

123. Wilson, D. S. & Keefe, A. D. Random mutagenesis by PCR. *Curr. Protoc. Mol. Biol.* **Chapter 8**, Unit8.3 (2001).

124. Cirino, P. C., Mayer, K. M. & Umeno, D. Generating Mutant Libraries Using Error-Prone PCR. in *Directed Evolution Library Creation* 3–10 (Humana Press, 2003). doi:10.1385/1-59259-395-X:3

125. Firnberg, E. & Ostermeier, M. The genetic code constrains yet facilitates Darwinian evolution. *Nucleic Acids Res.* **41**, 7420–8 (2013).

126. Bershtein, S., Segal, M., Bekerman, R., Tokuriki, N. & Tawfik, D. S. Robustness–epistasis link shapes the fitness landscape of a randomly drifting protein. *Nature* **444**, 929–932 (2006).

127. Salverda, M. L. M. *et al.* Initial mutations direct alternative pathways of protein evolution. *PLoS Genet.* **7**, e1001321 (2011).

128. Jacquier, H. *et al.* Capturing the mutational landscape of the beta-lactamase TEM-1. *Proc. Natl. Acad. Sci. U. S. A.* **110**, 13067–13072 (2013).

129. Canale, A. S., Cote-Hammarlof, P. A., Flynn, J. M. & Bolon, D. N. Evolutionary mechanisms studied through protein fitness landscapes. *Curr. Opin. Struct. Biol.* **48**, 141–148 (2018).

130. Tremblay, L. W., Hugonnet, J.-E. & Blanchard, J. S. Structure of the covalent adduct formed between *Mycobacterium tuberculosis* beta-lactamase and clavulanate. *Biochemistry* **47**, 5312–5316 (2008).

131. Mire, J. A. BlaC E166A faropenem acyl-intermediate complex. *Protein Data Bank* DOI: 10.2210/pdb4ebl/pdb (2013). doi:10.2210/pdb4ebl/pdb

132. Tremblay, L. W. & Blanchard, J. S. Crystal structure of BlaC-E166A covalently bound with cefuroxime. *Protein Data Bank* DOI: 10.2210/pdb3nbl/pdb (2011). doi:10.2210/pdb3nbl/pdb

133. Xie, H. *et al.* Rapid point-of-care detection of the tuberculosis pathogen using a BlaC-specific fluorogenic probe. *Nat. Chem.* **4**, 802–809 (2012).

134. Sutcliffe, I. C. & Harrington, D. J. Lipoproteins of *Mycobacterium tuberculosis*: An abundant and functionally diverse class of cell envelope components. *FEMS Microbiol. Rev.* **28**, 645–659 (2004).

135. Gu, S. *et al.* Comprehensive proteomic profiling of the membrane constituents of a *Mycobacterium tuberculosis* strain. *Mol. Cell. Proteomics* **2**, 1284–1296 (2003).

136. Tassoni, R. Structural characterization of bacterial proteins involved in antibiotic resistance and peptidoglycan biosynthesis. (Leiden, 2018).

137. Chen, Y., Bonnet, R. & Shoichet, B. K. The acylation mechanism of CTX-M β-lactamase at 0.88 Å resolution. *J. Am. Chem. Soc.* **129**, 5378–5380 (2007).

138. Pernot, L., Petrella, S. & Sougakoff, W. Crystal structure of the class A beta-lactamse L2 from *Stenotrophomonas maltophilia* at 1.51 angstrom. *Protein Data Bank* DOI: 10.2210/pdb1o7e/pdb (2004). doi:10.2210/pdb1o7e/pdb

139. Marciano, D. C. *et al.* Genetic and structural characterization of an L201P global suppressor substitution in TEM-1 β-lactamase. *J. Mol. Biol.* **384**, 151–164 (2008).

140. Levitte, S. *et al.* Mycobacterial acid tolerance enables phagolysosomal survival and establishment of tuberculous infection in vivo. *Cell Host Microbe* **20**, 250–258 (2016).

141. Nelson, D. L. & Cox, M. M. Lehninger Principles of biochemistry. in 497 (2005).

142. Artimo, P. *et al.* ExPASy: SIB bioinformatics resource portal. *Nucleic Acids Res.* **40**, W597–W603 (2012).

143. Vranken, W. F. *et al.* The CCPN data model for NMR spectroscopy: Development of a software pipeline. *Proteins: Struct., Funct., Bioinf.* **59**, 687–696 (2005).

144. Greives, N. & Zhou, H.-X. Both protein dynamics and ligand concentration can shift the binding mechanism between conformational selection and induced fit. *Proc.*

Natl. Acad. Sci. U. S. A. **111**, 10197–10202 (2014).

145. Vogt, A. D. & Di Cera, E. Conformational selection or induced fit? A critical appraisal of the kinetic mechanism. *Biochemistry* **51**, 5894–5902 (2012).

146. Du, X. *et al.* Insights into Protein-Ligand Interactions: Mechanisms, Models, and Methods. *Int. J. Mol. Sci.* **17**, (2016).

147. Bhabha, G. *et al.* A Dynamic Knockout Reveals That Conformational Fluctuations Influence the Chemical Step of Enzyme Catalysis. *Science* **332**, 234–238 (2011).

148. Kohen, A. Role of Dynamics in Enzyme Catalysis: Substantial versus Semantic Controversies. *Acc. Chem. Res.* **48**, 466–473 (2015).

149. Olmos, J. L. *et al.* Enzyme intermediates captured "on the fly" by mix-and-inject serial crystallography. *BMC Biol.* **16**, 59 (2018).

150. Pervushin, K., Riek, R., Wider, G. & Wüthrich, K. Attenuated T2 relaxation by mutual cancellation of dipole-dipole coupling and chemical shift anisotropy indicates an avenue to NMR structures of very large biological macromolecules in solution. *Proc. Natl. Acad. Sci. U. S. A.* **94**, 12366–12371 (1997).

151. Renner, C., Schleicher, M., Moroder, L. & Holak, T. A. Practical aspects of the 2D 15N-{1H}-NOE experiment. *J. Biomol. NMR* **23**, 23–33 (2002).

152. Gong, Q. & Ishima, R. 15N–{1H} NOE experiment at high magnetic field strengths. *J. Biomol. NMR* **37**, 147–157 (2007).

153. Ferrage, F., Piserchio, A., Cowburn, D. & Ghose, R. On the measurement of 15N-{1H} nuclear Overhauser effects. *J. Magn. Reson.* **192**, 302–13 (2008).

154. Ferrage, F., Reichel, A., Battacharya, S., Cowburn, D. & Ghose, R. On the measurement of ^{15}N-{^{1}H} nuclear Overhauser effects. 2. Effects of the saturation scheme and water signal suppression. *J. Magn. Reson.* **207**, 294–303 (2010).

155. Ferrage, F., Cowburn, D. & Ghose, R. Accurate Sampling of High-Frequency Motions in Proteins by Steady-State ^{15}N–{^{1}H} Nuclear Overhauser Effect Measurements in the Presence of Cross-Correlated Relaxation. *J. Am. Chem. Soc.* **131**, 6048–6049 (2009).

156. García de la Torre, J., Huertas, M. . & Carrasco, B. HYDRONMR: Prediction of NMR Relaxation of Globular Proteins from Atomic-Level Structures and Hydrodynamic Calculations. *J. Magn. Reson.* **147**, 138–146 (2000).

157. Stivers, J. T., Abeygunawardana, C., Mildvan, A. S. & Whitman, C. P. 15 N NMR Relaxation Studies of Free and Inhibitor-Bound 4-Oxalocrotonate Tautomerase: Backbone Dynamics and Entropy Changes of an Enzyme upon Inhibitor Binding. *Biochemistry* **35**, 16036–16047 (1996).

158. Tremblay, L. W., Hugonnet, J. E. & Blanchard, J. S. Crystal structure of the covalent adduct formed between TB B-lactamase and clavulanate. *Protein Data Bank* DOI: 10.2210/pdb3cg5/pdb (2008). doi:10.2210/pdb3cg5/pdb

159. Sagar, A., Haleem, N., Bashir, Y. M. & Ashish. Search for non-lactam inhibitors of mtb β-lactamase led to its open shape in apo state: new concept for antibiotic design. *Sci. Rep.* **7**, 6204 (2017).

160. Tassoni, R., Blok, A., Pannu, N. S. & Ubbink, M. New Conformations of Acylation Adducts of Inhibitors of β-Lactamase from Mycobacterium tuberculosis. *Biochemistry* **58**, 997–1009 (2019).

161. Bruker Corporation. Dynamics Center Manual. **003**, 110 (2018).

162. Woessner, D. E. Nuclear Spin Relaxation in Ellipsoids Undergoing Rotational

Brownian Motion. *J. Chem. Phys.* **37**, 647–654 (1962).

163. Vallurupalli, P., Hansen, D. F., Stollar, E., Meirovitch, E. & Kay, L. E. Measurement of bond vector orientations in invisible excited states of proteins. *Proc. Natl. Acad. Sci. U. S. A.* **104**, 18473–18477 (2007).

164. Delaglio, F. *et al.* NMRPipe: A multidimensional spectral processing system based on UNIX pipes. *J. Biomol. NMR* **6**, 277–293 (1995).

165. Hansen, D. F. *et al.* An exchange-free measure of 15 N transverse relaxation: An NMR spectroscopy application to the study of a folding intermediate with pervasive chemical exchange. *J. Am. Chem. Soc.* **129**, 11468–11479 (2007).

166. Galleni, M. *et al.* Use of the chromosomal class A beta-lactamase of Mycobacterium fortuitum D316 to study potentially poor substrates and inhibitory beta-lactam compounds. *Antimicrob. Agents Chemother.* **38**, 1608–1614 (1994).

167. Sauvage, E. *et al.* Crystal structure of the Mycobacterium fortuitum class A beta-lactamase: structural basis for broad substrate specificity. *Antimicrob. Agents Chemother.* **50**, 2516–2521 (2006).

168. Lenfant, F., Labia, R. & Masson, J. M. Replacement of lysine 234 affects transition state stabilization in the active site of beta-lactamase TEM1. *J. Biol. Chem.* **169**, 17187–17194 (1991).

169. Winkler, M. L. *et al.* Design and exploration of novel boronic acid inhibitors reveals important interactions with a clavulanic acid-resistant sulfhydryl-variable (SHV) β-lactamase. *J. Med. Chem.* **56**, 1084–1097 (2013).

170. Inoue, H., Nojima, H. & Okayama, H. High efficiency transformation of *Escherichia coli* with plasmids. *Gene* **96**, 23–28 (1990).

171. Winkler, M. L., Papp-Wallace, K. M., Taracila, M. A. & Bonomo, R. A. Avibactam and inhibitor-resistant SHV β-lactamases. *Antimicrob. Agents Chemother.* **59**, 3700–3709 (2015).

172. Krishnan, N. P., Nguyen, N. Q., Papp-Wallace, K. M., Bonomo, R. A. & van den Akker, F. Inhibition of Klebsiella β-Lactamases (SHV-1 and KPC-2) by Avibactam: A Structural Study. *PLoS One* **10**, e0136813 (2015).

173. Coulondre, C. & Miller, J. H. Genetic studies of the lac repressor: IV. Mutagenic specificity in the lacI gene of *Escherichia coli*. *J. Mol. Biol.* **117**, 577–606 (1977).

174. Hart, K. M., Ho, C. M. W., Dutta, S., Gross, M. L. & Bowman, G. R. Modelling proteins' hidden conformations to predict antibiotic resistance. *Nat. Commun.* **7**, 12965 (2016).

175. Bershtein, S., Serohijos, A. W. & Shakhnovich, E. I. Bridging the physical scales in evolutionary biology: from protein sequence space to fitness of organisms and populations. *Curr. Opin. Struct. Biol.* **42**, 31–40 (2017).

176. Bastolla, U., Dehouck, Y. & Echave, J. What evolution tells us about protein physics, and protein physics tells us about evolution. *Curr. Opin. Struct. Biol.* **42**, 59–66 (2017).

177. Figliuzzi, M., Jacquier, H., Schug, A., Tenaillon, O. & Weigt, M. Coevolutionary Landscape Inference and the Context-Dependence of Mutations in Beta-Lactamase TEM-1. *Mol. Biol. Evol.* **33**, 268–280 (2016).

178. Fritz, R., Alzate-Morales, J. H., Spencer, J., Mulholland, A. J. & van der Kamp, M. W. Multiscale simulations of clavulanate inhibition identify the reactive complex in class A β-lactamases and predict efficiency of inhibition. *Biochemistry*

acs.biochem.8b00480 (2018). doi:10.1021/acs.biochem.8b00480

179. Cortina, G. A. & Kasson, P. M. Predicting allostery and microbial drug resistance with molecular simulations. *Curr. Opin. Struct. Biol.* **52**, 80–86 (2018).

180. Latallo, M. J., Cortina, G. A., Faham, S., Nakamoto, R. K. & Kasson, P. M. Predicting allosteric mutants that increase activity of a major antibiotic resistance enzyme. *Chem. Sci.* **8**, 6484–6492 (2017).

181. Pande, V. S., Beauchamp, K. & Bowman, G. R. Everything you wanted to know about Markov State Models but were afraid to ask. *Methods* **52**, 99–105 (2010).

182. Zimmerman, M. I. *et al.* Prediction of New Stabilizing Mutations Based on Mechanistic Insights from Markov State Models. *ACS Cent. Sci.* **3**, 1311–1321 (2017).

183. Siddiq, M. A., Hochberg, G. K. & Thornton, J. W. Evolution of protein specificity: insights from ancestral protein reconstruction. *Curr. Opin. Struct. Biol.* **47**, 113–122 (2017).

184. Bush, K. Past and Present Perspectives on β-Lactamases. *Antimicrob. Agents Chemother.* **62**, e01076-18 (2018).

185. Tehrani, K. H. M. E. & Martin, N. I. β-lactam/β-lactamase inhibitor combinations: an update. *Medchemcomm* **9**, 1439–1456 (2018).

186. Avci, F. G., Altinisik, F. E., Ulu, D. V., Olmez, E. O. & Akbulut, B. S. An evolutionarily conserved allosteric site modulates beta-lactamase activity. *J. Enzyme Inhib. Med. Chem.* (2016). doi:10.1080/14756366.2016.1201813

187. Avci, F. G. *et al.* Targeting a hidden site on class A beta-lactamases. *J. Mol. Graph. Model.* **84**, 125–133 (2018).

188. Deshpande, D. *et al.* Ceftazidime-avibactam has potent sterilizing activity against highly drug-resistant tuberculosis. *Sci. Adv.* **3**, e1701102 (2017).

189. Lefebvre, A.-L. *et al.* Bactericidal and intracellular activity of β-lactams against *Mycobacterium abscessus*. *J. Antimicrob. Chemother.* dkw022- (2016). doi:10.1093/jac/dkw022

190. Kaushik, A. *et al.* Combinations of avibactam and carbapenems exhibit enhanced potencies against drug-resistant *Mycobacterium abscessus*. *Future Microbiol.* fmb-2016-0234 (2017). doi:10.2217/fmb-2016-0234

191. Kaushik, A. *et al.* In vitro activity of the new β-lactamase inhibitors relebactam and vaborbactam in combination with β-lactams against *Mycobacterium abscessus* complex clinical isolates. *Antimicrob. Agents Chemother.* AAC.02623-18 (2019). doi:10.1128/AAC.02623-18

Summary

The availability of antibiotics to treat infectious diseases has revolutionised healthcare. The current rise of antibiotic resistance, coupled with the recent void in antibiotic discoveries, threatens to undermine that progress. The work presented in this thesis aims to contribute to a greater understanding of resistance and its evolution, at the protein level. The model protein that was used for these studies is BlaC, the β-lactamase of *Mycobacterium tuberculosis*. This bacterium causes the highest yearly human death count of all pathogens and BlaC provides it with resistance to a broad spectrum of β-lactam antibiotics. The protein can be inhibited by β-lactamase inhibitors, enabling treatment of the disease with the combination of these inhibitors and β-lactam antibiotics. This treatment option is gaining popularity as a last-resort treatment option for tuberculosis bacteria that have gained resistance to other anti-tuberculosis drugs. Chapter 1 provides an introduction to and description of BlaC, as well as an introduction to some of the methodologies that were used here to study it.

Chapter 2 deepens the functional understanding of BlaC by specifying its activity in various conditions. The reversibility of BlaC inhibition by clavulanic acid is addressed especially. Whereas previous literature was inconsistent with regards to whether or not BlaC is able to hydrolyse clavulanic acid, we show conclusively that indeed it is. The hydrolysis is heavily dependent on the conditions. Specifically, the presence of phosphate, which binds to the active site with an affinity of *ca*. 30 mM, accelerates the hydrolysis of clavulanic acid by more than an order of magnitude. This finding adds to an existing volume of work on BlaC, which altogether provides a functional and structural understanding of the protein, which is, however, based on a static view of its structure. Proteins in solution at physiological temperatures do not exist in a single conformation but rather as a dynamic ensemble of conformations. Exchange between different conformations occurs on time scales ranging from picoseconds to second or even hours. The fast exchange is observed for processes on the low Ångström scale, for example, rotation of methyl groups, whereas larger motions, such as concerted movement of domains and unfolding are much slower. Some of these exchange processes and their time scales, magnitudes and localisation in the protein can be studied by nuclear magnetic resonance (NMR) spectroscopy. Chapter 3 provides the first such description of the dynamic behaviour of BlaC. It was found to be very rigid on fast time scales, showing very little local movement. On the millisecond time scale, however, significant motion was detected, specifically in the active site. These findings resemble those on related β-lactamases, and the rate of the active site motion was accurately determined for the first time, at *ca*. 860 s^{-1}. This chapter also provides the first insights into the effect of ligand binding on β-lactamase dynamics. It was found that

upon binding of inhibitor clavulanic acid, BlaC dynamics on all time scales increase dramatically. Fast motions in the α-domain of the enzyme indicate loss of stability of the hydrophobic core, while the direct observation of multiple conformations indicated either a shift in equilibrium and decrease in exchange rate of the active site motions, or the introduction of a second, very slow process.

As the use of β-lactam / β-lactamase inhibitor combinations to treat tuberculosis is gaining traction, it is also interesting to investigate if and how BlaC can potentially mutate to gain resistance to inhibition. Chapter 4 describes the development and application of a simulated evolution assay to identify mutations that confer resistance to clavulanic acid. The mutation that was found to confer most resistance, K234R, had already been described kinetically by Egesborg *et al.*, but nothing was yet known about the potential role of dynamics in the inhibitor-resistant phenotype. Chapter 4 therefore also describes NMR dynamics studies on this mutant and another mutant, G132N, which was identified by Soroka *et al.* to convey the same inhibitor-resistant phenotype upon BlaC. The results are surprisingly different. The G132N mutation causes an extensive region around the BlaC active site to experience two almost equally populated conformations, exchanging at *ca.* 70 s^{-1}. In the K234R mutant, however, no millisecond dynamics were detected at all. These results indicate that multiple evolutionary routes are available to reach the same inhibitor resistant phenotype. Furthermore, as the K234R mutant is active, they also show that active site dynamics on the millisecond time scale are not required for function.

Chapter 5 discusses the research presented in this thesis in the context of the overarching research goal of the Ubbink group and the overall progression of the scientific field. The work in this thesis adds to the understanding of BlaC inhibition and its dynamic behaviour, laying the foundation for detailed, ongoing studies of the roles of conserved residues and the laboratory evolution experiments aimed at understanding the evolutionary landscape of BlaC. Ultimately, we expect that this knowledge can help in the development of inhibitors that are less prone to resistance.

Samenvatting

De beschikbaarheid van antibiotica voor de behandeling van infectieziektes heeft de gezondheidszorg gerevolutioneerd. De opkomst van antibioticaresistentie, samen met het recente gebrek aan nieuwe antibiotica, dreigt die vooruitgang te ondermijnen. Het werk in dit proefschrift wil bijdragen aan een beter begrip van resistentie en de evolutie daarvan, op eiwitniveau. Het modeleiwit BlaC, de β-lactamase van *Mycobacterium tuberculosis*, is gebruikt voor dit onderzoek. De *M. tuberculosis* bacterie veroorzaakt bij mensen de meeste sterfgevallen van alle infectieziektes, en BlaC veroorzaakt de resistentie tegen een breed scala aan β-lactam antibiotica. Dit enzym kan geremd worden met β-lactamase remmers, waardoor behandeling van tuberculose mogelijk wordt met een combinatie van deze remmers en β-lactam antibiotica. Deze behandeloptie wordt meer en meer gebruikt als laatste redmiddel bij tuberculose bacteriën die resistent zijn tegen andere medicijnen. Hoofdstuk 1 bevat een inleiding in en beschrijving van BlaC, evenals een introductie tot sommige van de technieken die in dit onderzoek gebruikt zijn om dit eiwit te bestuderen.

Hoofdstuk 2 verdiept het functionele begrip van BlaC door zijn activiteit onder verschillende omstandigheden te definiëren. Vooral de omkeerbaarheid van de remming van BlaC door clavulaanzuur is onderzocht. Voorgaande studies spraken elkaar tegen over de vraag of BlaC deze remmer kan hydrolyseren, maar wij laten zien dat dat inderdaad het geval is. De hydrolyse is sterk afhankelijk van de condities. Specifiek de aanwezigheid van fosfaat, dat in de active site bindt met een dissociatieconstante van *ca*. 30 mM, versnelt de hydrolyse van clavulaanzuur met meer dan een orde van grootte. Alle studies die tot nu toe aan BlaC zijn gedaan hebben samen al een goed functioneel en structureel begrip van het eiwit opgeleverd. Dit is echter wel een statisch beeld van de structuur, en dat is vaak niet voldoende. Bij fysiologische temperaturen bestaan eiwitten in oplossing niet uit een enkele conformatie, maar uit een dynamisch ensemble van conformaties. Uitwisseling tussen de verschillende conformaties vindt plaats op tijdsschalen variërend van picoseconden tot seconden of zelfs uren. Snelle uitwisseling zien we voor processen op de lage Ångström lengteschaal, zoals de rotatie van methylgroepen. Veel langzamer zijn de processen op grotere schaal, zoals bewegingen van domeinen en vouwing. Sommige van deze uitwisselprocessen en hun tijdsschalen, groottes en lokalisatie in het eiwit kunnen bestudeerd worden met kernspinresonantie (NMR) spectroscopie. In hoofdstuk 3 wordt voor het eerst het dynamische gedrag van BlaC beschreven. Het enzym blijkt erg rigide te zijn op snelle tijdsschalen, met maar weinig lokale beweging. Op de milliseconde-tijdsschaal werd echter wel significante beweging gedetecteerd, specifiek in de active site. Deze bevindingen lijken op die bij verwante β-lactamases. De snelheid van de active site beweging werd voor het eerst nauwkeurig vastgesteld, op 860 s^{-1}. Dit hoofdstuk beschrijft

ook de eerste inzichten in het effect van ligandbinding op β-lactamase-dynamiek. Binding van de remmer clavulaanzuur blijkt de dynamiek van BlaC op alle tijdsschalen dramatisch te vergroten. Snelle beweging in het α-domein van het enzym is een aanwijzing voor stabiliteitsverlies van de hydrofobe kern. De waarneming van meerdere conformaties geeft aan ofwel dat er een verandering in de balans van bestaande conformaties en een vertraging van de beweging plaatsvindt, ofwel dat er een tweede, erg langzame beweging bijgekomen is.

Aangezien het gebruik van β-lactam / β-lactamaseremmer combinaties voor de behandeling van tuberculose toeneemt, is het interessant om te onderzoeken of en hoe BlaC zou kunnen muteren om inhibitieresistent te worden. Hoofdstuk 4 beschrijft de ontwikkeling en toepassing van een experiment om evolutie in het laboratorium te kunnen simuleren en daarmee mutaties te identificeren die clavulaanzuurresistentie verlenen. Van de BlaC-variant die het meest resistentie bleek te verlenen, K234R, waren de kinetische eigenschappen al beschreven door Egesborg *et al.*, maar er was nog niets bekend over de eventuele rol van eiwitdynamiek in het remmerresistente fenotype. Hoofdstuk 4 beschrijft daarom ook NMR-onderzoek naar de dynamiek van deze enzymvariant en een andere, G132N, waarvan door Soroka *et al.* gevonden was dat die BlaC hetzelfde remmerresistente fenotype verleent. De resultaten zijn verrassend verschillend. De G132N-mutatie zorgt ervoor dat veel kernen in een groot gebied rond de active site in twee conformaties voorkomen, die ongeveer dezelfde populatie hebben en uitwisselen met een snelheid van *ca*. 70 s^{-1}. In de K234R-variant, aan de andere kant, werd helemaal geen millisecondedynamiek gevonden. Deze resultaten betekenen dat er meerdere evolutionaire routes beschikbaar zijn om hetzelfde remmerresistente fenotype te bereiken. Aangezien de K234R-variant actief is, laten ze verder zien dat de beweging in de active site op de milliseconde tijdsschaal niet nodig is voor de functie.

In hoofdstuk 5 wordt het onderzoek dat in dit proefschrift is gepresenteerd in de context van het overkoepelende doel van het onderzoek in de Ubbink-groep en de voortgang van het algehele onderzoeksveld geplaatst. De resultaten dragen bij aan het begrip van de interactie van remmers en BlaC, evenals de dynamiek van dit enzym. Daarmee legt het de basis voor verdere, reeds lopende onderzoeken naar de rol van geconserveerde residuen voor BlaC en het evolutionaire landschap van BlaC. We verwachten dat dit werk uiteindelijk kan helpen bij de ontwikkeling van remmers waartegen *M. tuberculosis* niet gemakkelijk resistent zal kunnen worden.

In dit licht zijn de resultaten die in deze thesis beschreven worden nogal bescheiden. Desalniettemin zouden deze toevoegingen aan het begrip van de remming en dynamiek van BlaC uiteindelijk bij kunnen dragen aan een groter begrip evolutie in het algemeen en, wellicht, de ontwikkeling van minder resistentiegevoelige remmers.

Curriculum Vitae

Wouter Elings was born in Utrecht, The Netherlands on the 12th of April 1989 and raised in Heerde, The Netherlands. After completing voorbereidend wetenschappelijk onderwijs (vwo, specialising in nature and health) in 2007, he moved to Wageningen, The Netherlands to study Molecular Life Sciences at Wageningen University and Research Centre (WUR). During his studies he participated in the international Genetically Engineered Machine (iGEM) competition as part of the WUR iGEM 2012 team. Due to their combined efforts, the team was not only awarded a gold medal and a finalist position in the iGEM competition, but was also awarded with a Sweet Sixteen position and the prize for Europe's Best Presentation. After completing his master's internship in the proteomics research group at the European Molecular Biology Laboratory in Heidelberg, Germany, he graduated his masters in 2015. Wouter then started as a PhD student in the Protein Chemistry (later Macromolecular Biochemistry) group at Leiden University, with prof. dr. Marcellus Ubbink. For his PhD he studied the inhibition, dynamics and evolution of the β-lactamase of *Mycobacterium tuberculosis*, BlaC. After completing this thesis in 2019, he continued his work in a post-doctoral research position in the same group.

Publications

1. **Elings, W., Tassoni, R., van der Schoot, S. A., Luu, W., Kynast, J. P., Dai, L., Blok, A. J., Timmer, M., Florea, B. I., Pannu, N. S. and Ubbink, M.** (2017) Phosphate promotes the recovery of *Mycobacterium tuberculosis* β-lactamase from clavulanic acid inhibition. *Biochemistry 56*, 6257–6267.
2. **Elings, W., Gaur, A., Blok, A. J., Timmer, M., Ingen, H. van and Ubbink, M.** β-Lactamase of *Mycobacterium tuberculosis* shows dynamics in the active site that increase upon inhibitor binding. *Manuscript submitted to Antimicrobial Agents and Chemotherapy*
3. **Elings, W., Zanten, D. B. van, Drenth, R., Blok, A. J., Timmer, M. and Ubbink, M.** Role of protein dynamics in BlaC evolution towards clavulanic acid resistance. *Manuscript to be submitted*